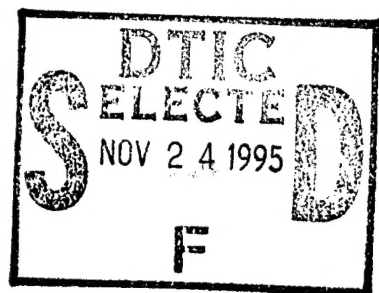


NASA CR-175061



National Aeronautics and
Space Administration



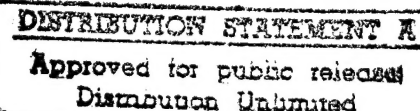
EVALUATION OF CAPILLARY REINFORCED COMPOSITES

"Original contains color plates: All DTIC reproductions will be in black and white"

by

Samuel W. Ciardullo and Lewis J. Stoffer
General Electric Company
Aircraft Engine Business Group
Cincinnati, Ohio 45215

19951120 138



DTIC QUALITY INSPECTED 8

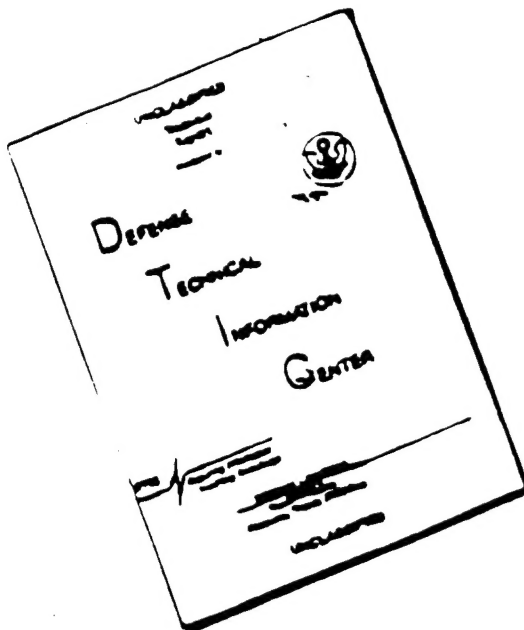
Prepared for
National Aeronautics and Space Administration

DEPARTMENT OF DEFENSE
PLASTICS TECHNICAL EVALUATION CENTER
BRIADCOM, DOVER, N. H. 03801

NASA Lewis Research Center
Contract NAS3-24386

48934

DISCLAIMER NOTICE



**THIS DOCUMENT IS BEST
QUALITY AVAILABLE. THE COPY
FURNISHED TO DTIC CONTAINED
A SIGNIFICANT NUMBER OF
PAGES WHICH DO NOT
REPRODUCE LEGIBLY.**

* For sale by the National Technical Information Service, Springfield, Virginia 22161

PREFACE

The work described herein was conducted by the GENERAL ELECTRIC AIRCRAFT ENGINE BUSINESS GROUP (GE AEBG) under Contract NAS3-24386 for the NASA LEWIS RESEARCH CENTER, Cleveland, Ohio. The NASA Project Manager was Mr. Kenneth Bowles.

For General Electric AEBG, the overall program was performed by the Advanced Composites Technology Development group under Mr. Stephen C. Mitchell. Mr. Samuel W. Ciardullo was Program Manager and Mr. Lewis J. Stoffer was the Technical Project Manager. Other key General Electric contributors to this program were:

James E. Cahill - Specialist, Heat Transfer Lab/Windtunnel

Pauline M. Eichelberger, Specialist, Thermographic Imaging

John F. Halase - Manager, Infra-Red Inspection

William K. South - Manager, Development Heat Transfer Unit

Dr. Ronald D. Zerkle - Manager Heat Transfer Design Methods

Accesion For	
NTIS	CRA&I
DTIC	TAB
Unannounced	
Justification _____	
By _____	
Distribution / _____	
Availability Codes	
Dist	Avail and/or Special
A-1	

TABLE OF CONTENTS

1.0	Summary	1
2.0	Introduction	2
3.0	Program Guidelines	4
4.0	Technical Approach	5
4.1	Thermal Model	5
4.2	Steady State One Dimensional Thermal Model	5
4.3	Steady State Two Dimensional Thermal Model	11
4.4	Experimental Test Panels	24
4.5	Physical Properties of Test Panel	31
5.0	Wind Tunnel Test Rig	45
5.1	Wind Tunnel Testing	45
5.2	Test Data Analysis	53
5.3	Heat Transfer Analysis	53
5.4	Conclusions From the SIMCAP Analysis	92
5.5	Boundary Layer Results	93
5.6	Conclusions From the Boundary Layer	94
6.0	Infrared Measurement of Surface Temperature	95
6.1	Infared Temperature Measurement Sensor	95
6.2	Measurement System Calibration	95
6.3	Preliminary Emmissivity Test	96
6.4	Data Acquisition	96
6.5	Data Analysis	100
6.6	Results	100
7.0	Combined 2D Wall Heat Conduction and 1D Compressible Tube Air Mathematical Model	104
7.1	Thermal Analysis of Capillary Reinforced Composites .	104
7.2	Two-Dimensional Heat Conduction Analysis	104
7.2.1	Analysis of a Simple Test Case: A Plane Wall .	106
7.2.2	Analysis of the Reference Case	108
7.2.3	Effect of Heat Transfer at the Hot Wall Surface	110
7.2.4	Effect of a Second Layer of Tubes	110
7.2.5	Effect of Tube Spacing on Heat Conduction .	111
7.3	Axial Variation of TWALL	115
7.4	Comparison of Test Results with Computer Code	117
8.0	Summary and Conclusions	126
9.0	Projections for Future Captube Effort	127
10.0	Proposed Follow-on Effort	131

LIST OF TABLES

		Page
Table I	Flow Check Data Sheet - No. I	55
Table II	Flow Check Data Sheet - No. II	62
Table III	Capillary Tubes W/Ragged Ends Flow Check	63

LIST OF ILLUSTRATIONS

Figure		Page
1	Convection Heated Configuration	6
2	Hot-Air Passages for Anti Icing	7
3	SS1D Heat Transfer Model Effect of Y_{WALL} and $T_{K_{WALL}}$	9
4	SS1D Heat Transfer Model Effect of HTCO and HTCI	10
5	SS1D Heat Transfer Model Effect of Tube Diameter	12
6	Capillary Tube	13
7	SS2D Heat Transfer Model Effect of Captube Mass Flowrate on T_{CAP} and T_{WALL}	15
8	SS2D Captube Heat Transfer Model Effect on Captube Diameter and Length on Mass Flowrate	19
9	SS2D Captube Heat Transfer Model Effect of Tube Diameter on Mach Number Distribution	20
10	SS2D Captube Heat Transfer Model Effect of Tube Diameter on Pressure Distribution	21
11	SS2D Captube Heat Transfer Model Effect of Tube Diameter on T_{WALL} and T_{CAP}	22
12	SS2D Captube Heat Transfer Model Effect of Tube Diameter and T_{Source} on HTCI	23
13	SS2D Captube Heat Transfer Model Effect of P_{Source} on M_{Cap} Within Larger Tube	25
14	SS2D Captube Heat Transfer Model Effect of Y_{Wall} on M_{Cap} Within Larger Tube	26
15	SS2D Captube Heat Transfer Model Effect of HTCO on M_{Cap} Within Larger Tube	27
16	SS2D Captube Heat Transfer Model Effect of P_{Source} on T_{Wall} and T_{Cap} Within Larger Tube	28
17	SS2D Captube Heat Transfer Model Effect of HTCO on T_{Wall} and T_{Cap} Within Larger Tube	29
18	SS2D Captube Heat Transfer Model Effect of Y_{Wall} on T_{Wall} and T_{Cap} Within Larger Tube.	30
19	Final Experimental Designs	32

LIST OF ILLUSTRATIONS

20	Wind Tunnel Test Panels, 90°	33
21	Wind Tunnel Test Panels, 0°	34
22	Tube Panels for Property Testing	35
23	Capillary Panel for Physical Test	36
24	Capillary Tubing Panel A Flexural Strength Test Report	37
25	Capillary Tubing Panel B Flexural Strength Test Report	38
26	Capillary Tubing Panels A & B Compressive Strength Test Report	39
27	Capillary Tubing Panels A & B Tensile Strength Test Report	40
28	Capillary Tubing Panels A & B Short Beam Shear Test Report	41
29	Microphotograph of Capillary Tube Panels Showing 0.012 inch ID Tubes Above and 0.020 inch Tubes Below	43
30	Cross Ply Capillary Tube Test Panel	44
31	Wind Tunnel Test Features	46
32	Wind Tunnel Test Section with Captubes at Crossflow	47
33	Wind Tunnel Test Rig Assembly	48
34	Wind Tunnel Test Rig Horn	49
35	Wind Tunnel Test Rig Plenum Chamber	50
36	Wind Tunnel Test Rig	51
37	Test Panel Plenum, Bottom View	52
38	Test Panel Plenum, Side View	52
39	Wind Tunnel Test Set-Up for Check Out	53

LIST OF ILLUSTRATIONS

40	Plot of Predicted and Measured Adiabatic Flow Check Thru 204 Tubes	56
41	Exit Mach Number Vs. Source Pressure of Adiabatic Flow Check	57
42	Exit Reynolds Number Vs. Source Pressure of Adiabatic Flow Check	58
43	204 Tubes Arranged in Parallel for Manifold Adiabatic Flow Check	59
44	Flow Check Data Sheet	61
45	F/F Vs. Press Ratio	64
46	Flow Rate Vs. Source Pressure - Small Tubes	65
47	Exit Mach Numbers Vs. Sources Pressure - Small Tubes	66
48	Tube Exit Reynolds Number Vs. Source Pressure - Small Tubes	67
49	Mass Flowrate Vs. Source Pressure	68
50	Prediction of Exit Mach Number Vs. Source Pressure	69
51	Prediction of Reynolds Number at Tube Exit Vs. Source Pressure	70
52	Prediction for Heat Transfer Test at T = 95F/S=70F.	71
53	Prediction for Heat Transfer Test at T = 120F/S = 70F	72
54	Prediction for Heat Transfer Test at T = 170F/S = 70F	73
55	Prediction for Heat Transfer Test at T = 250F/S = 70F.	74
56	Prediction for Heat Transfer Test Effect of HTCO at T = 120F, S = 70F, P = 50 psia.	75
57	Prediction for Heat Transfer Test Effect of P Vs. T = 120F, S = 70F.	76
58	Prediction for Heat Transfer Test of Larger Tubes with T = 120F, S = 70F for Mass Flowrate	77
59	Prediction for Heat Transfer Test of Larger Tubes with T = 120F, S = 70F for Mach Number at Tube Exit	78

LIST OF ILLUSTRATIONS

60	Prediction for Heat Transfer Test of Larger Tubes With T = 120F, S = 70F for Reynolds Number at Tube Exit	79
61	Prediction for Heat Transfer Test of Smaller Tubes Effect of P vs. T = 120F, S = 70F. - Short Panel	80
62	Prediction for Heat Transfer Test of Smaller Tube Effect of P Vs. T = 120F, S = 70F - Long Panel	81
63	Prediction for Heat Transfer of Small Tube Effect of P Vs. T = 120F, S = 70F on Mass Flowrate	82
64	Prediction for Heat Transfer Test of Smaller Tube With T = 120F, S = 70F on Mach Number at Tube Exit	83
65	Prediction for Heat Transfer Test of Smaller Tubes With T = 120F, S = 70F on Reynolds Number at Tube Exit	84
66	KEPS Boundary Layer Analysis for Various Mach Number Flows in Test Duct	85
67	KEPS Boundary Layer Analysis for Heat Transfer Coeficient Along the Duct.	86
68	KEPS Boundary Layer Analysis for Variations of Heat Flux and Velocity BL Thickness Along Duct Walls	87
69	KEPS Boundary layer Analysis of Heat Flux and Velocity BL Thickness Along Duct Wall.	88
70	KEPS Boundary Layer Analysis of Heat Transfer Tests on 2 Inch Pre-Heat Section/Counterflow Air Streams	89
71	KEPS Boundary Layer Analysis of Heat Transfer Tests on 2 Inch Pre-Heat Section - HTC Effect.	90
72	KEPS Boundary Layer Analysis of Heat Transfer Tests on 2 Inch Pre-Heat Section - Q_{WALL} Effect.	91
73	Infrared Measurement Test Apparatus	97
74	Infrared Camera Set-Up to View Test Panel	98
75	Cross Flow Test Panel in Wind Tunnel Throat	99
76	Computer Color Enhanced Images for Test Point 120 - showing successively narrower temperature windows	101

LIST OF ILLUSTRATIONS

77	Colorized Images with Corresponding Temperature Maps, Describing Two Test Points	102
78	Basic Conduction Problem	105
79	Simple Plan Wall Test Case	107
80	Reference Case: One Layer of Tubes	109
81	Control Area with Two Layers of Tubes	112
82	Effect of Tube Spacing on Dimensionless Wall Surface Temperature	113
83	Effect of Tube Spacing on Dimensionless Wall Surface Heat Transfer	114
84	Effect of Tube Spacing on Heat Conduction Shape Factor	116
85	SS2D Captube Heat Transfer Model Effect of Captube Spacing on TWALL and TCAP Distributions	117
86	Actual Vs. Predicted Heat Transfer Tests - Mass Flowrate Vs. Source Pressure	119
87	Actual Vs. Predicted Heat Transfer Tests - Wall Temperature Vs. Panel Length - Test 101A	120
88	Actual Vs. Predicted Heat Transfer Tests - Wall Temperature Vs. Panel Length - Test 103A	121
89	Actual Vs. Predicted Heat Transfer Tests - Wall Temperature Vs. Panel Length - Test 112	122
90	Actual Vs. Predicted Heat Transfer Tests - Wall Temperature Vs. Panel Length - Test 114	123
91	Actual Vs. Predicted Heat Transfer Tests - Wall Temperature Vs. Panel Length - Test 117	124
92	Actual Vs. Predicted heat Transfer Tests - Wall Temperature Vs. Panel Length - Test 120.	125
93	Graphite/PMR15 Composite Anti-Iced IGV Assembly	128
94	Graphite/PMR15 Composite Anti-Iced Front Frame Assembly	129
95	Concept for Anti-Icing IGV Flap	130

1.0 SUMMARY

The objective of this program was to advance the technology needed for designing advanced anti-iced composite structures which inherently have low transverse thermal conductivity. Anti-icing of the metal components in the inlet of jet engines is usually achieved with high pressure heated air. The air is directed forward from the compressor through ducts to manifolds that direct the air to the internal cavities of areas that are susceptible to ice formation. The heat is then conducted rapidly through metal to the air flow surface to prevent ice from forming. This program was conducted to investigate the prospect of conducting heated air through small capillary tubes (CAPTUBES) that are embedded in the surface of composite inlet components. The heated air is then delivered directly to the surface of such components rather than relying on heat being conducted through thick composite walls that are inherently poor conductors of heat.

An analytical computer program was developed to predict the anti-icing performance of heated pressurized air flowing through small glass capillary tubes embedded in a composite wall. A physical wind tunnel test conducted on a flat test panel with capillary tubes clustered on its surface in tight parallel array was found to display excellent agreement with the analytical code. The heat transfer test results and the analytical code results both indicate feasibility of using capillary tubes for surface heating of composites.

Issues remaining to be evaluated for this captube anti-icing system are:

- o Long term influence of stress corrosion and contamination of capillary tubes.
- o Impact damage and possible methods of repair.
- o Mechanical design, engine systems and further heat transfer studies.
- o Proof-of-concept test on a composite frame sector.
- o Maintenance methods for unplugging clogged tubes.
- o Engine performance benefits.

2.0 INTRODUCTION

The use of composite materials is essential in meeting the high thrust to-weight and low-cost goals of the new General Electric family of commercial and military engines. Consequently, the application of advanced composite structures in aircraft gas turbine engines is expanding as weight and cost reductions become more difficult to achieve with metal designs. Over the past 15 years, the basic feasibility of fabricating major engine structures utilizing advanced composite materials has been demonstrated through the fabrication and test of a number of components. Most of these components, however, have been in the cooler portions of the engine because of the temperature limitation of graphite/epoxy, which has received the most attention due to its availability and advanced stage of development. The use of advanced composites in the higher (300°F to 600°F) temperature regions has been paced by the slower emergence of the polyimide-type matrix systems.

The first series of polyimides to be investigated were of the condensation cure type which were difficult to process. Subsequently, reaction type systems were developed that were some improvement, but still presented difficult processing problems. One of the first polyimide-type matrix systems to offer both relative ease of processing with good, consistent part quality at a competitive cost was the NASA-Lewis Research Center-developed PMR system. Although somewhat more limited in temperature capability than a conventional condensation-type polyimide system, PMR15 has the highest potential for opening up the 300°F to 550°F temperature range to the economic application of advanced composites.

An application of high temperature composites that would exist on many military (T700, F404, F110) and commercial (CT700, GE36, GE38) engines is in the front frame structure. A typical front frame is a primary structural component that supports the front end of the engine, and controls the airflow to the fan. Consequently, the front frame may contain the main engine mounts and/or support the forward thrust bearing. Since the frame is the first component, it must be capable of being anti-iced and the struts must be able to withstand various types of foreign object damage. Unfortunately, the design requirement for anti-icing places significant cost, weight, and performance penalties on both the frame and engine. Increased attention, therefore, is being focused on new anti-icing techniques that will allow for the application of composites to anti-iced engine structures.

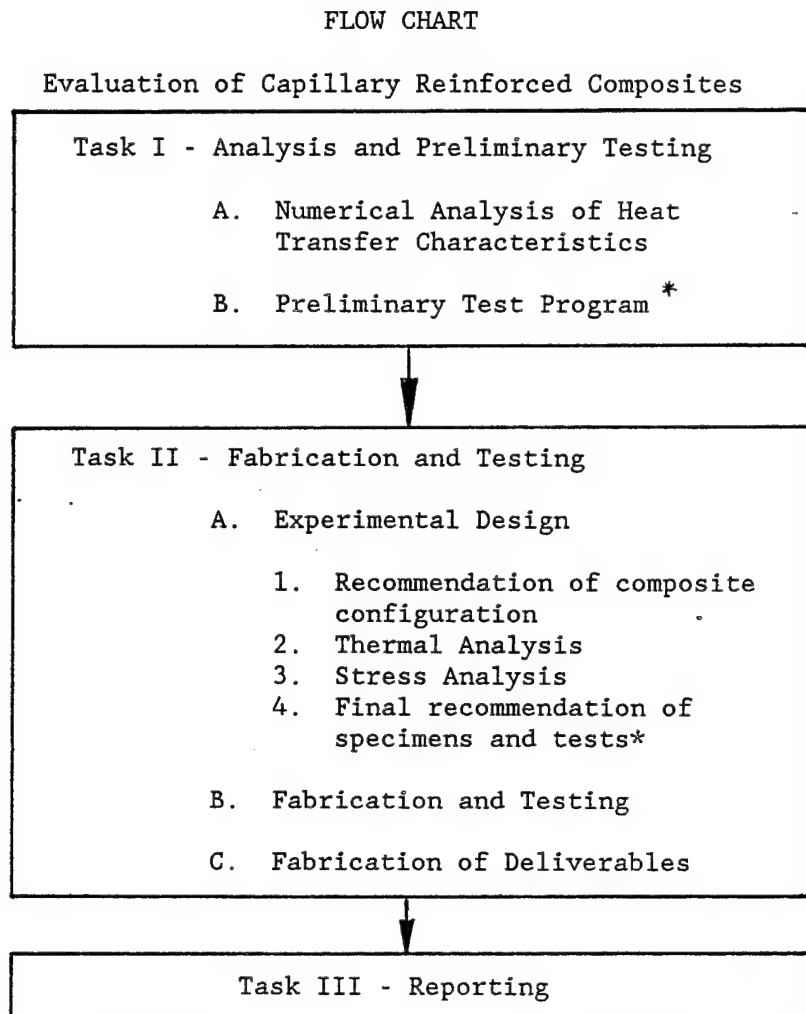
Initially both electrical and air anti-icing concepts were investigated. Unfortunately, the initial work showed large power requirements for electrical anti-icing and the subsequent lack of on-board power terminated the use of electrical anti-icing. Consequently, all efforts have been focused on hot air anti-icing concepts.

Anti-icing in jet engines is generally performed with high pressure, heated air that is directed from the compressor through a series of pipes to manifolds located on the exterior of the anti-iced structures. From the manifold the air is directed to all flowpath surfaces that may be susceptible to ice formation. Depending on the size and shape of the surface to be heated, the anti-icing function may be performed by either heat conduction or by film heating.

It was the objective of this program to develop an advanced materials and design concept needed for designing advanced, anti-iced composite structures. The concept that was evaluated uses flexible micro-capillaries embedded in a composite structure as a hot air distribution system for anti-icing. This method has the potential of providing an efficient, anti-icing technique that could be better than present approaches. The success of this program has helped remove a major barrier in the application of lightweight, low cost, composite designs to anti-iced structures.

3.0 PROGRAM GUIDELINES

The program to accomplish the objectives of this capillary heating evaluation was divided into three tasks as shown in the following Flow Chart.



*NASA Project Manager Approval

4.0 TECHNICAL APPROACH

4.1 Thermal Model

The concept for this analysis is illustrated in Figure 1. Air at elevated pressure and temperature would enter and flow through very small tubes located near the surface of a composite wall exposed to very cold moist air. Heat would flow from the hot air to the cold air, causing the wall outside surface temperature to be warmer than if the tubes were not present. The tubes would then exhaust to low pressure surroundings.

It was of interest to determine if available capillary-size tubing (0.0126 and 0.0209 inch inside diameter) could provide sufficient energy flow at typical pressures and temperatures to achieve effective anti-icing protection. Therefore, an objective of this analysis was to derive mathematical models which relate performance characteristics to design parameters. The models could then be used to examine the feasibility of this anti-icing concept and to guide an experimental validation program.

4.2 Steady-State One-Dimensional Thermal Model

Consider the cross-section of a tube assembly shown in Figure 2(a), and the cross-section of a single capillary tube shown in Figure 2(b). For the initial study, it was assumed that no spacing exists between the tubes, and all of the heat flows directly from a tube to the nearest wall outside surface.

The local stagnation temperature of the hot air in the tube is TCAP, and the temperature of the cold air is TSINK. Heat flows from the hot gas to the tube inside surface having a heat transfer coefficient HTCI. It is then conducted through the tube wall having thermal conductivity TKTUBE. A protective layer of material with thickness YWALL and thermal conductivity TKWALL is located between the capture and the wall outside surface having a heat transfer coefficient HTCO.

A circuit representation for the SS1D model is shown in Figure 2(c). The heat flow per unit tube length, q' , is related to the individual thermal resistances in the circuit as follows:

$$\begin{aligned} q' &= (TCAP-TTI)/RI && (1) \\ &= (TTI-TTO)/RTUBE && (2) \\ &= (TTO-TWALL)/RWALL && (3) \\ &= (TWALL-TSINK)/RO && (4) \end{aligned}$$

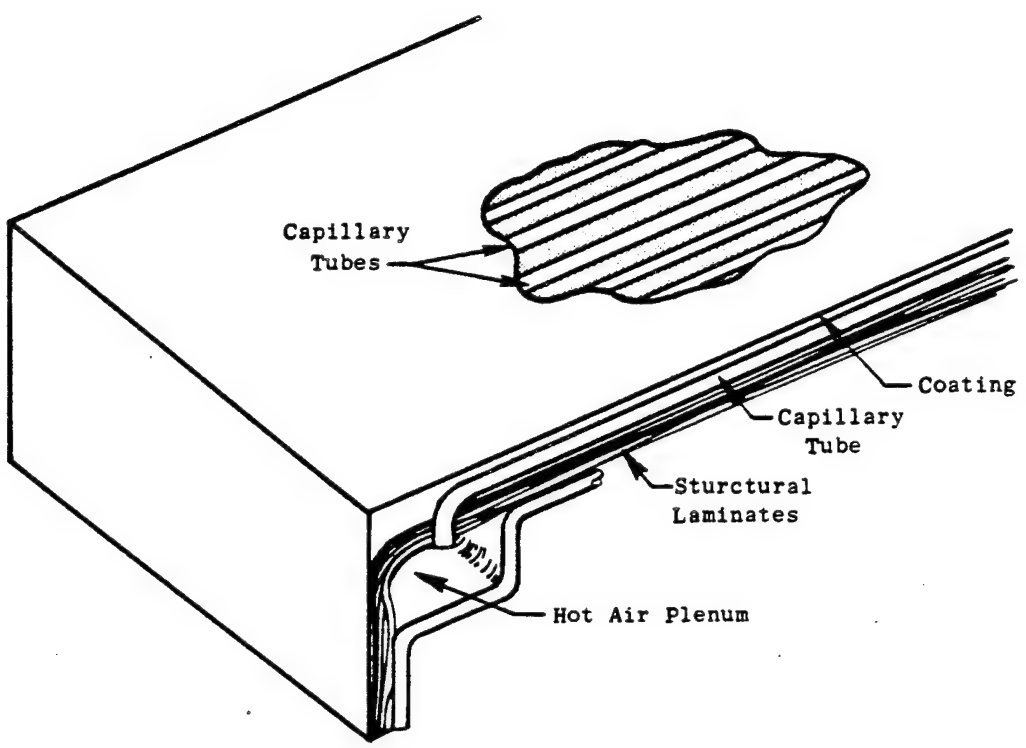
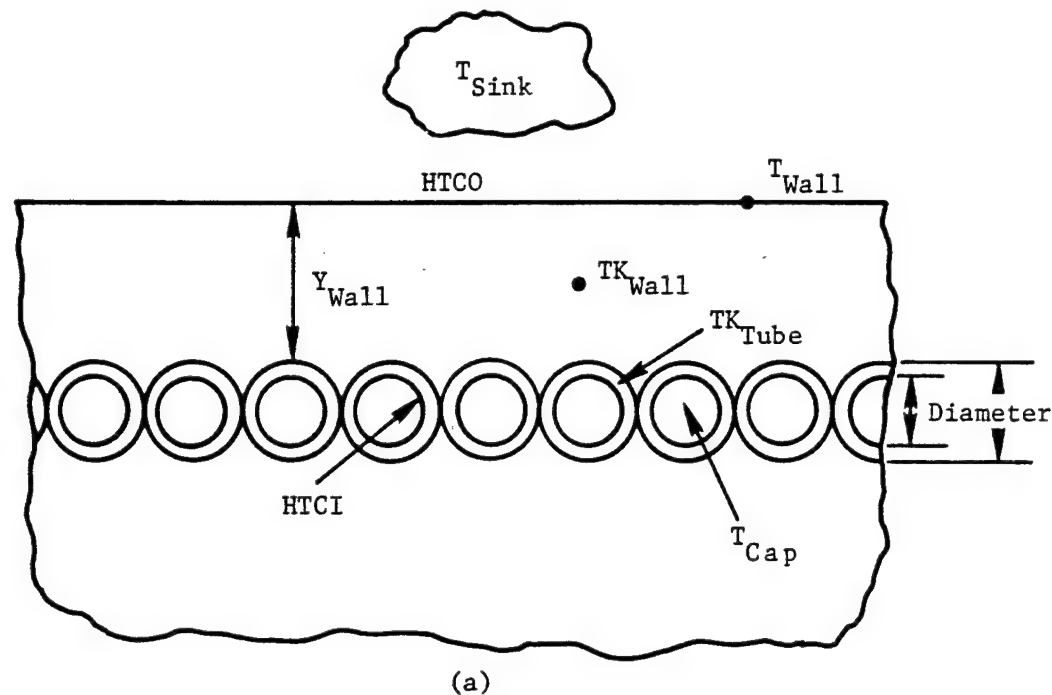
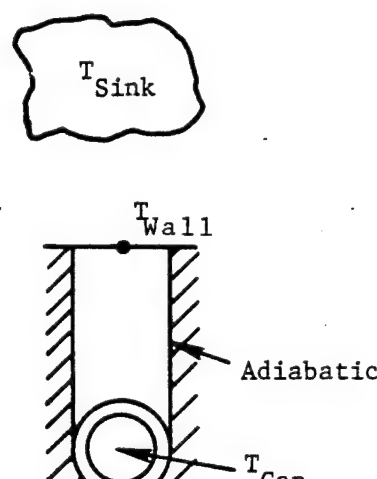


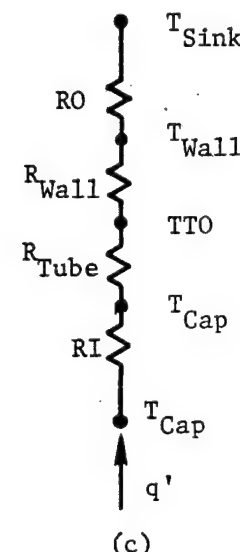
Figure 1. Convection Heated Configuration.



(a)



(b)



(c)

Figure 2. Hot-Air Passages for Anti-Icing.

where

$$RI = 2/(HTCI*\pi*DI) \quad (5)$$

$$RTUBE = ALOG(DO/DI)/\pi*TKTUBE \quad (6)$$

$$RWALL = [YWALL+DO(1-\pi/4)/2]/(DO*TKWALL) \quad (7)$$

$$RO = 1/(HTCO*DO) \quad (8)$$

$$RTOT = RI + RTUBE + RWALL + RO \quad (9)$$

Equations (1-4) can be solved simultaneously to eliminate the intermediate temperatures TTI, TTO and TWALL. The resulting expression for the heat loss from the capture per unit length as a function of the model parameters is

$$q' = (TCAP-TSINK)/RTOT \quad (10)$$

Equation (10) can be combined with Equation (4) and rearranged to obtain the following relation for the wall outside surface temperature as a function of TCAP and the model parameters:

$$\frac{(TWALL-TSINK)}{(TCAP-TSINK)} = \frac{RO}{RTOT} \quad (11)$$

The model parameters are TSINK, TKWALL, YWALL, HTCI, HTCO, DI, DO, AND TKTUBE. TKTUBE is assumed to have a value of 1 (Btu/hr-ft-F), corresponding to glass. Two tube sizes were available for testing. The smaller tube had an insider diameter of 0.0126 inch, and the larger tube had an inside diameter of 0.0209 inch. Both tubes had a wall thickness of 0.004 inch. HTCI was expected to have a value in the range from 100 to 500 (Btu/hr-sq. ft-F), and HTCO from 50 to 150 (Btu/hr-sq. ft-F). TKWALL was expected to have a value in the range from 0.2 to 0.5 (Btu/hr-ft-F).

The effect of YWALL and TKWALL on TWALL is shown in Figure 3. Values of model parameters listed at the top of Figure 3 were used with Equation (11) to obtain these results.

An illustration of the use of Figure 3 is as follows. Typical temperatures for the T700 engine at a "worst case" are TSINK = 4F and TCAP = 152F. If the desired value of TWALL is 40° F in order to provide anti-icing protection, then

$$\frac{TWALL-TSINK}{TCAP-TSINK} = \frac{40-(-4)}{152-(-4)} = \frac{44}{156} = 0.282$$

From Figure 3 at the above dimensionless temperature level, if TKWALL = 0.2 (BTU/hr-ft-F), then YWALL = 0.050 inch. That is, if YWALL were less than 0.050 inch, then TWALL would be warmer than 40° F. Also, if YWALL were fixed at 0.050 inch, then TWALL would be warmer than 40° F if TKWALL were greater than 0.2 (Btu/hr-ft-F).

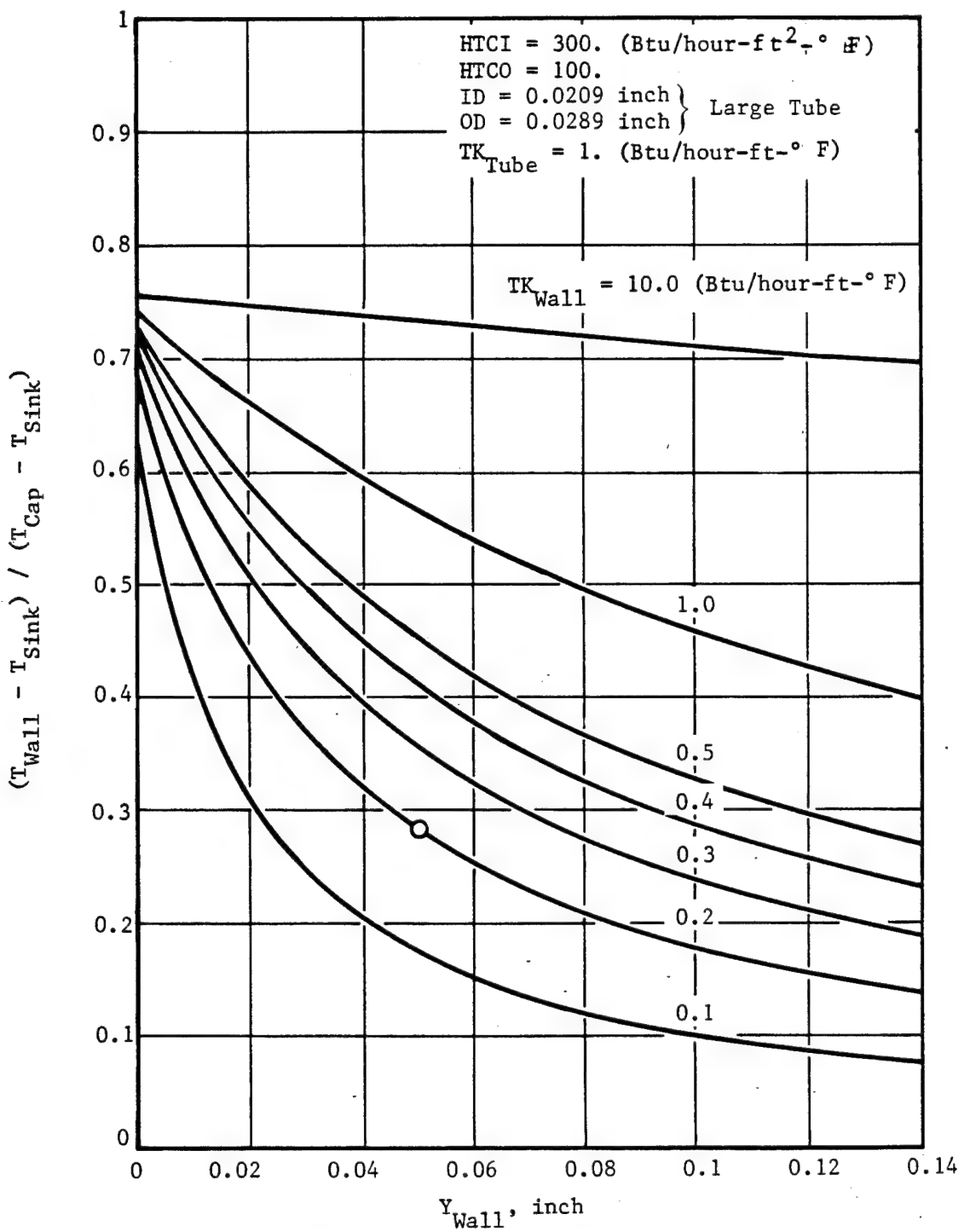


Figure 3. SSID Heat Transfer Model Effect of Y_{Wall} and TK_{Wall} .

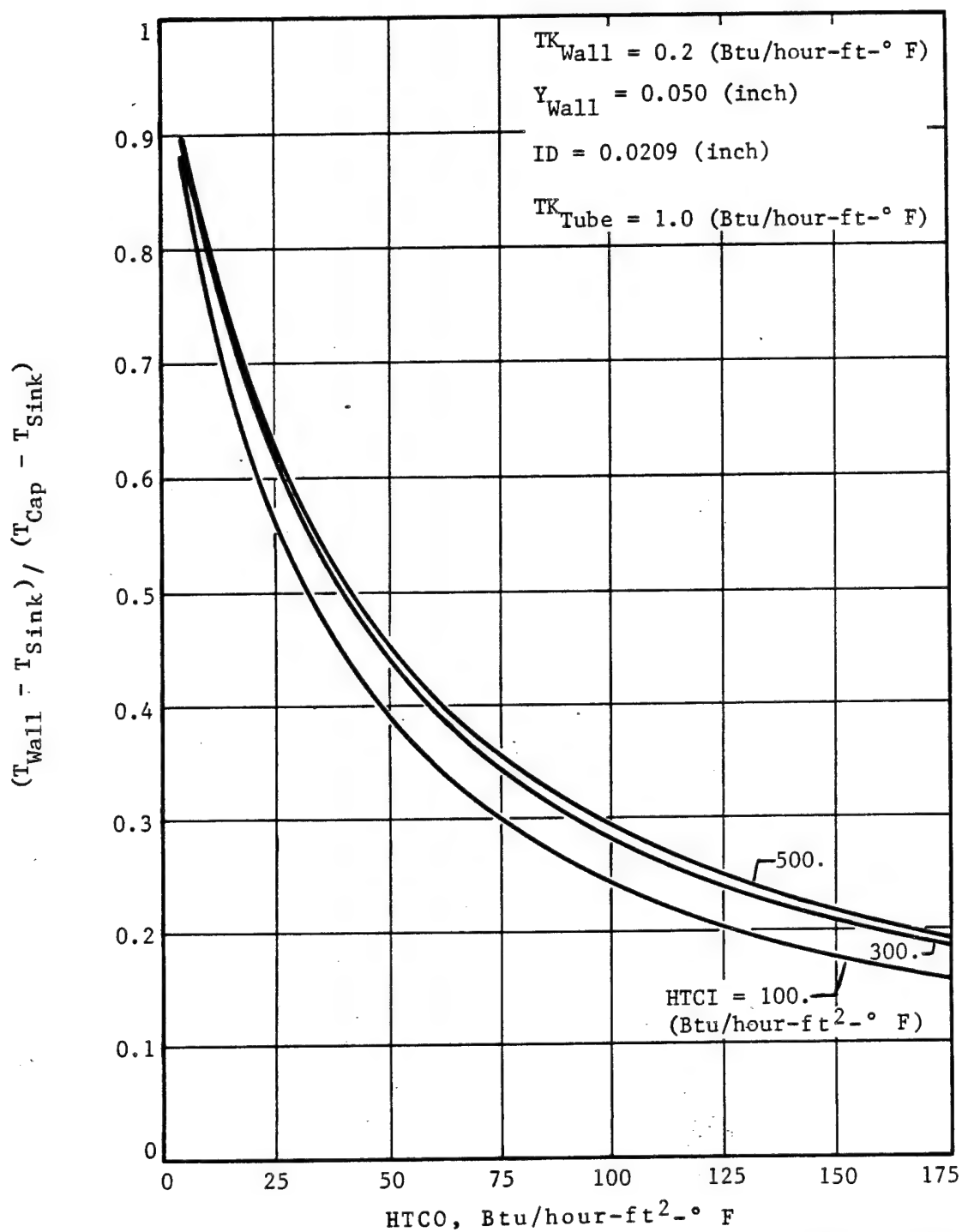


Figure 4. SSID Heat Transfer Model Effect of HTCO and HTCI.

The effects of heat transfer coefficients, $HTCO$ and $HTCI$ on dimensionless wall outside surface temperature, are shown in Figure 4. It can be seen that $TWALL$ is very sensitive to $HTCO$, and relatively insensitive to $HTCI$. This is because the variation of $HTCO$ occurs at the location of $TWALL$, whereas the wall and tube resistances exist between the locations of $HTCI$ and $TWALL$, and tend to damp the influence of $HTCI$ on $TWALL$.

The effect of tube diameter on dimensionless wall outside surface temperature is plotted in Figure 5. The SS1D model indicates that the dimensionless wall temperature is insensitive to tube diameter. However, this result can be misleading, because tube diameter will have an important effect upon the mass flowrate of hot air through the captube, and the temperature distribution of the hot air in the captube, $TCAP$, will decrease significantly with decreased tube diameter. This effect is demonstrated by the two-dimensional model described in the following section.

4.3 Steady-State Two-Dimensional Thermal Model

The temperature of the hot air will decrease as it flows through the capillary tube and loses heat through the wall material to the cold air. Equation (11) indicates that the wall outside surface temperature, $TWALL$, is proportional to the local hot air temperature, $TCAP$. Therefore, the wall surface temperature will also become colder in the direction of the captube flow, and can lose its anti-icing ability.

The energy carrying capacity of the hot air is proportional to its mass flowrate through the captube. Thus, mass flowrate has a strong influence upon temperature decrease along the captube, and the relationship between these quantities can be derived as follows.

Consider the side view of the capillary tube imbedded in a composite wall as represented in Figure 6. Hot air at pressure $PSOURCE$ and temperature $TSOURCE$ enters the captube and flows at mass flowrate $MCAP$ in the axial direction z with origin at the tube entrance. The local stagnation temperature of the hot air in the tube is $TCAP$. Heat at the local rate q' is transferred from the captube through the wall layer to the cold air at pressure $PSINK$ and temperature $TSINK$. It is assumed here that q' is described by Equation (10), and the local wall surface temperature $TWALL$ is related to $TCAP$ and the model parameters by Equation (11). If conservation of energy is applied to a differential control volume of length dz within the captube, then the heat transfer rate from the control volume is equal to a decrease of stagnation enthalpy. That is,

$$q' dz = -MCAP*CP*d(TCAP) \quad (12)$$

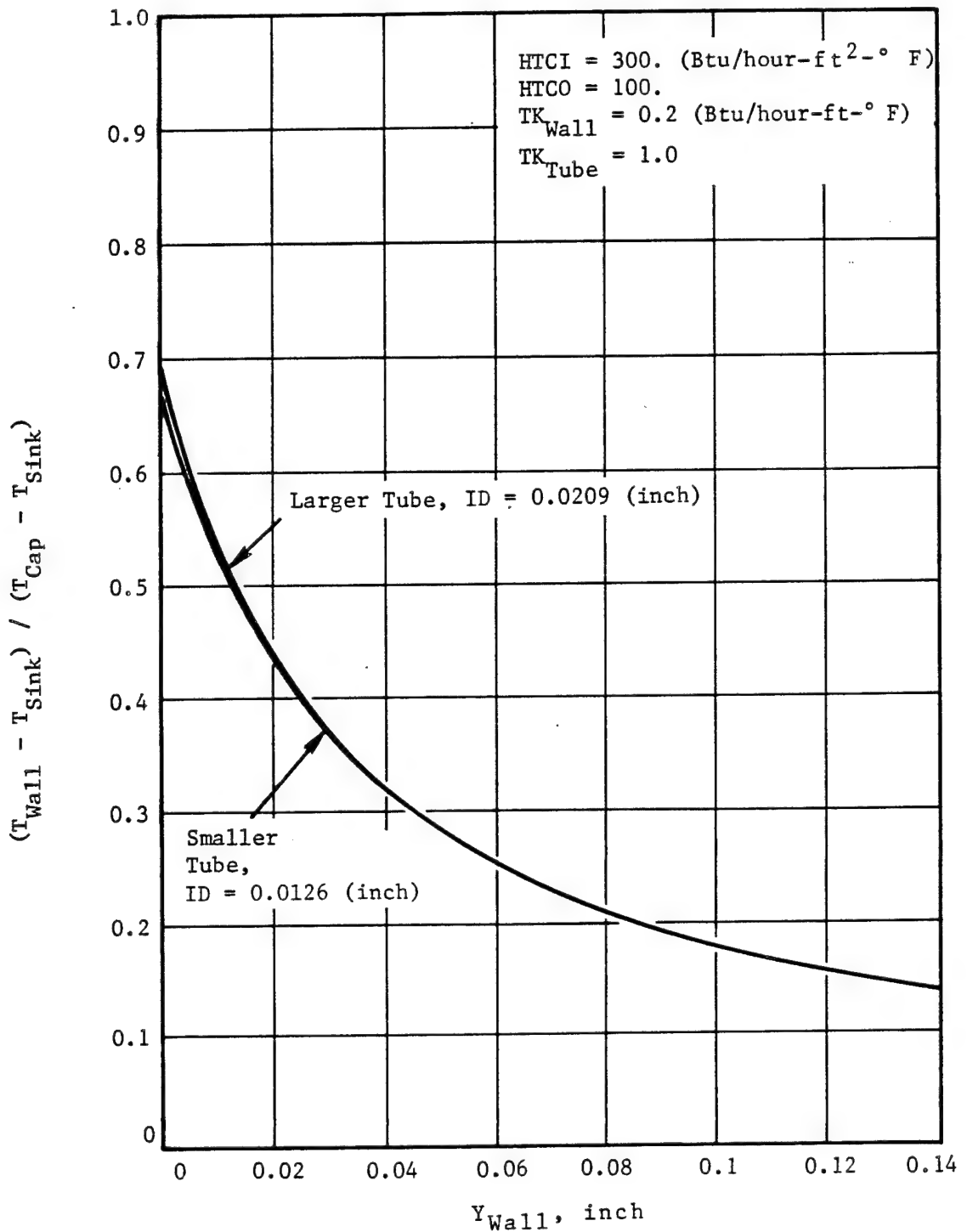


Figure 5. SS1D Heat Transfer Model Effect of Tube Diameter.

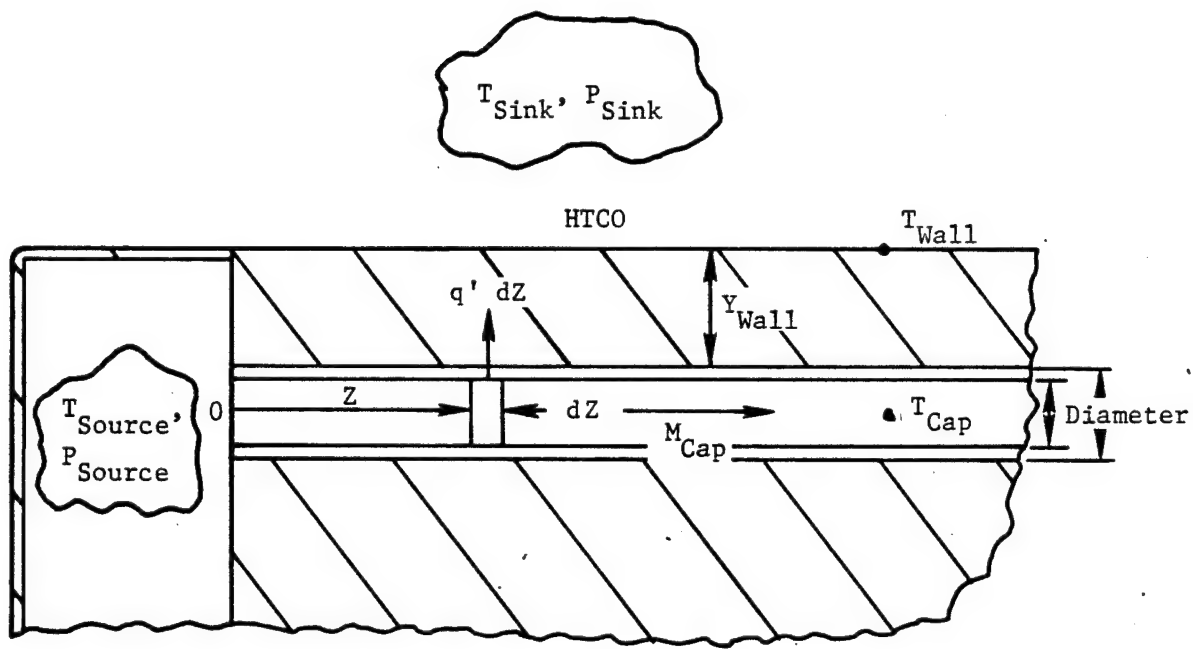


Figure 6. Capillary Tube.

where C_P is the specific heat of air at constant pressure. Substituting Equation (10) for q' into Equation (12) and separating variables gives

$$\int_{TSOURCE}^{\text{TCAP}} \frac{d(\text{TCAP})}{(\text{TCAP}-\text{TSINK})} = - \int_0^z \frac{dz}{(\text{MCAP} \cdot C_P \cdot R_{TOT})} \quad (13)$$

If MCAP , C_P and R_{TOT} are constant along the captube length, then Equation (13) can be integrated to give

$$\frac{(\text{TCAP}-\text{TSINK})}{(\text{TSOURCE}-\text{TSINK})} = \exp [-z / (\text{MCAP} \cdot C_P \cdot R_{TOT})] \quad (14)$$

and Equation (11) can be rearranged to the following form:

$$\frac{(\text{TWALL}-\text{TSINK})}{(\text{TSOURCE}-\text{TSINK})} = \frac{(\text{TCAP}-\text{TSINK})}{(\text{TSOURCE}-\text{TSINK})} * (R_0 / R_{TOT}) \quad (15)$$

Equations (14) and (15) relate TCAP and TWALL to z , MCAP and the model parameters including TSOURCE , TSINK , YWALL , TKWALL , HTCI , HTCO , DI , DO , TKTUBE , and C_P .

The effect of MCAP on TCAP and TWALL distributions along the captube are shown in Figure 7. Values of model parameters listed at the bottom of Figure 7 were used with Equations (14) and (15) to obtain these results. Figure 7 shows that the decrease of TWALL along the captube directions can be large when the captube mass flowrate is less than one lbm/hr , and the decrease of TWALL is relatively small when MCAP is greater than one lbm/hr .

Equations (14) and (15) can be useful in evaluating the anti-icing thermal performance of capillary tubes. However, they are not complete because MCAP is also a function of design parameters including the source and sink pressures and the captube length. Therefore it is necessary to develop a mathematical model which relates MCAP to design parameters.

In general, air flow in a capillary tube must be treated as a compressible flow. The length to diameter ratio of a one foot long tube with an inside diameter of 0.0209 inch is 574. Thus, viscous friction has an important effect upon the flow. That is, an inlet to exhaust pressure ratio of five or more is required in order to achieve significant mass flowrate through the tube. Since mass density for air is proportional to pressure then density can also

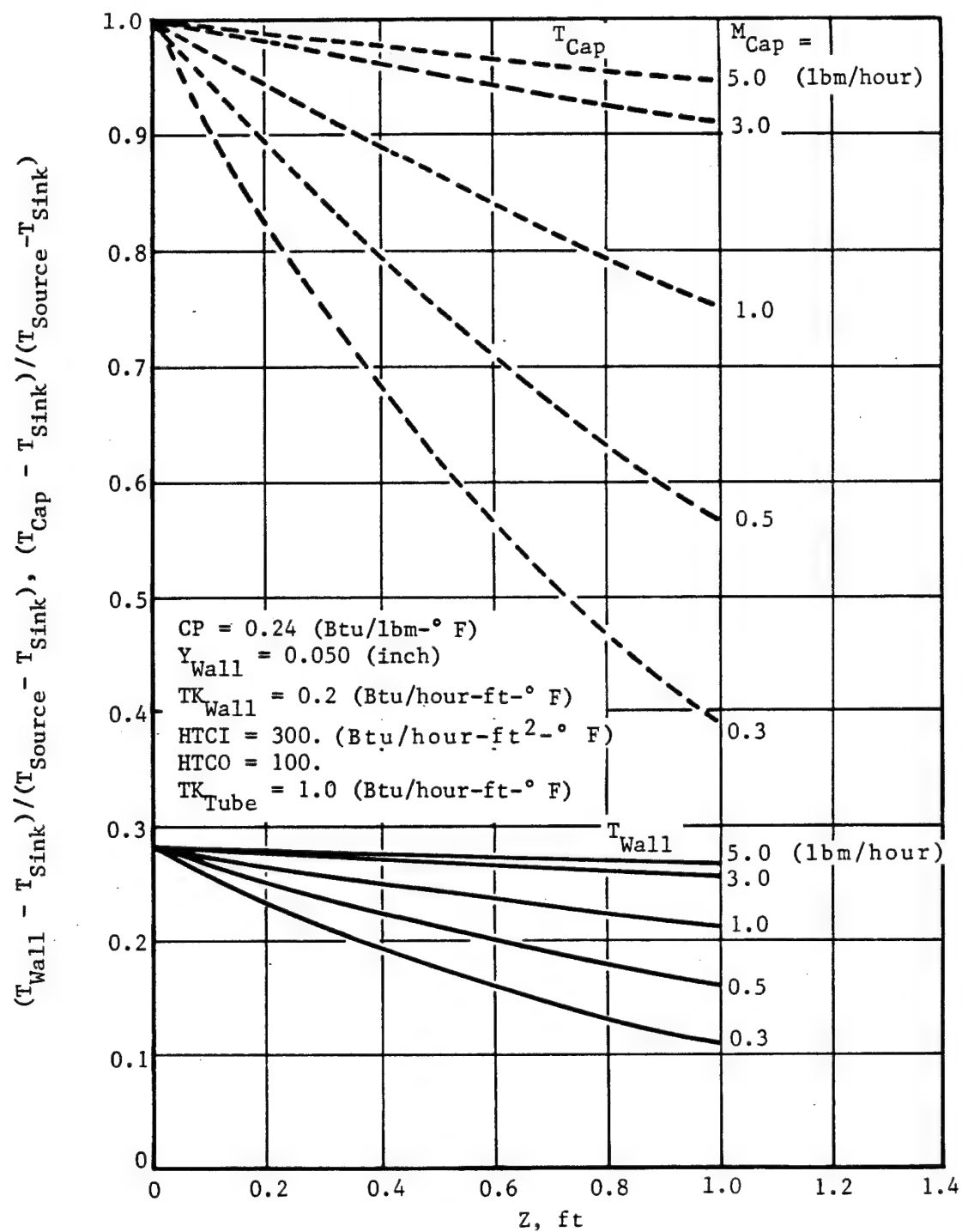


Figure 7. SS2D Heat Transfer Model Effect of Capture Mass Flowrate on T_{Cap} and T_{Wall} .

decrease by a factor of five or more. Since local air speed in the tube is inversely proportional to mass density, the air speed can also accelerate by a factor of five or more along the tube length, and can approach the local acoustic speed of the air. In fact, compressible flow theory indicates that the air speed can accelerate along a constant diameter tube only until it reaches the limiting value of its acoustic speed at the tube exit; that is, until the Mach number is one at the exit. This compressible flow phenomenon is called "choking".

If the tube inlet pressure at a choked flow condition is increased, then the mass flowrate will also increase, however, the Mach number at the exit will remain equal to one, and the pressure in the exit plane will rise above the exhaust pressure. Thus, the choked mass flowrate in a tube becomes independent of its exhaust pressure.

Heat transfer can also affect compressible flow in a tube. For example, if the air is heated, then its temperature will increase, its density will decrease, and the local air speed will tend to increase. Thus, compressible flow in a tube is very complex and, in general, it is necessary to numerically integrate a coupled set of differential equations satisfying conservation of mass, momentum and energy as well as the equation of state for the gas.

For flow in a constant diameter tube with heat transfer and viscous friction, the general equations reduce to the following forms convenient for calculation. The equation describing the variation of Mach number is

$$\frac{dM}{dz} = \frac{M(1+0.5(GAM-1)MSQ)}{2(1-MSQ)} \left[\frac{(1+GAM*MSQ)}{T_0} \frac{dT_0}{dz} + GAM*MSQ*4*FF/DI \right] \quad (16)$$

where MSQ is M^2 , GAM is the specific heat ratio for the air, T_0 is the stagnation temperature of the air, and FF is the friction factor for flow in a tube. Therefore, the last term on the RHS of Equation (16) describes the effect of viscous friction, and the next to last term includes the effect of heat transfer. That is, the variation of stagnation temperature is related to the local heat transfer rate by

$$\frac{dT_0}{dz} = - \frac{q'}{MCAP*CP} \quad (17)$$

The third and last differential equation needed for numerical solution is

$$\frac{dP_0}{dz} = - \frac{P_0 * \Gamma * M^2}{2} \frac{[1 - \frac{dT_0}{T_0} + 4 * FF / DI]}{dz} \quad (18)$$

Where P_0 is the local stagnation pressure of the air in the capture. After M , T_0 , and P_0 have been determined, then all remaining properties of the flow can be determined from algebraic equations.

Several additional relations are required in order to integrate Equations (16-18). Correlations for friction factor, FF , and tube inside heat transfer coefficient, $HTCI$, were taken from the literature; and a computer subroutine containing thermodynamic and thermophysical properties of air as a function of temperature was constructed. Equations (5-10) were used to evaluate the local heat transfer rate, q' , appearing in Equation (17); however, the temperature of the capture air was taken as its recovery (adiabatic wall) temperature which is related to stagnation temperature and Mach number as follows:

$$TCAP = \frac{T_0 * [1 + 0.89(\Gamma - 1)M^2/2]}{[1 + (\Gamma - 1)M^2/2]} \quad (19)$$

Note that $TCAP = .687.17R$ for $T_0 = 700R$, $\Gamma = 1.4$, and $M = 1$. Thus, the recovery effect becomes significant at high Mach number, especially in devices requiring small variation of wall surface temperature.

A computer program called SIMCAP was developed to simulate the complete steady-state two-dimensional capture model. Equations (16-18) are integrated using the Euler predictor-corrector method beginning at the tube inlet where $P_0 = PSOURCE$ and $T_0 = TSOURCE$. However, the inlet Mach number is unknown at the beginning of calculation. Therefore, SIMCAP uses the bisection method to iterate for the inlet Mach number which satisfies both the inlet and outlet conditions. That is, the lower and upper bounds for inlet Mach number are known to be zero and one. The inlet Mach number for each iteration is assumed to be the average of the upper and lower bounds (e.g., 0.5 for the first iteration), and integration proceeds from the tube inlet. If the local Mach number reaches a value of one upstream of the tube exit, or if the local pressure falls below $PSINK$, then the assumed inlet Mach number is too large and it becomes the upper bound for the next iteration. Alternately, if the integration reaches the tube exit with a calculated exit Mach number less than one, but the calculated exit pressure is greater than $PSINK$, then the assumed inlet Mach number is too small and it becomes the lower bound for the next iteration.

The iteration procedure in SIMCAP is converged when the exit Mach number is acceptably close to a value of one or, if less than one, the calculated exit pressure must be acceptably close to the value of PSINK. The process typically requires less than twenty iterations to converge to an acceptable solution. After convergence all quantities of interest, including MCAP and TWALL, are written to output files for printing or plotting.

The steady-state two-dimensional capture model contained in the SIMCAP program includes the following input parameters: PSOURCE, TSOURCE, PSINK, TSINK, HTCO, TKWALL, YWALL, DI, DO, and tube length. The program has been used to investigate the influence of several of these parameters upon capture performance.

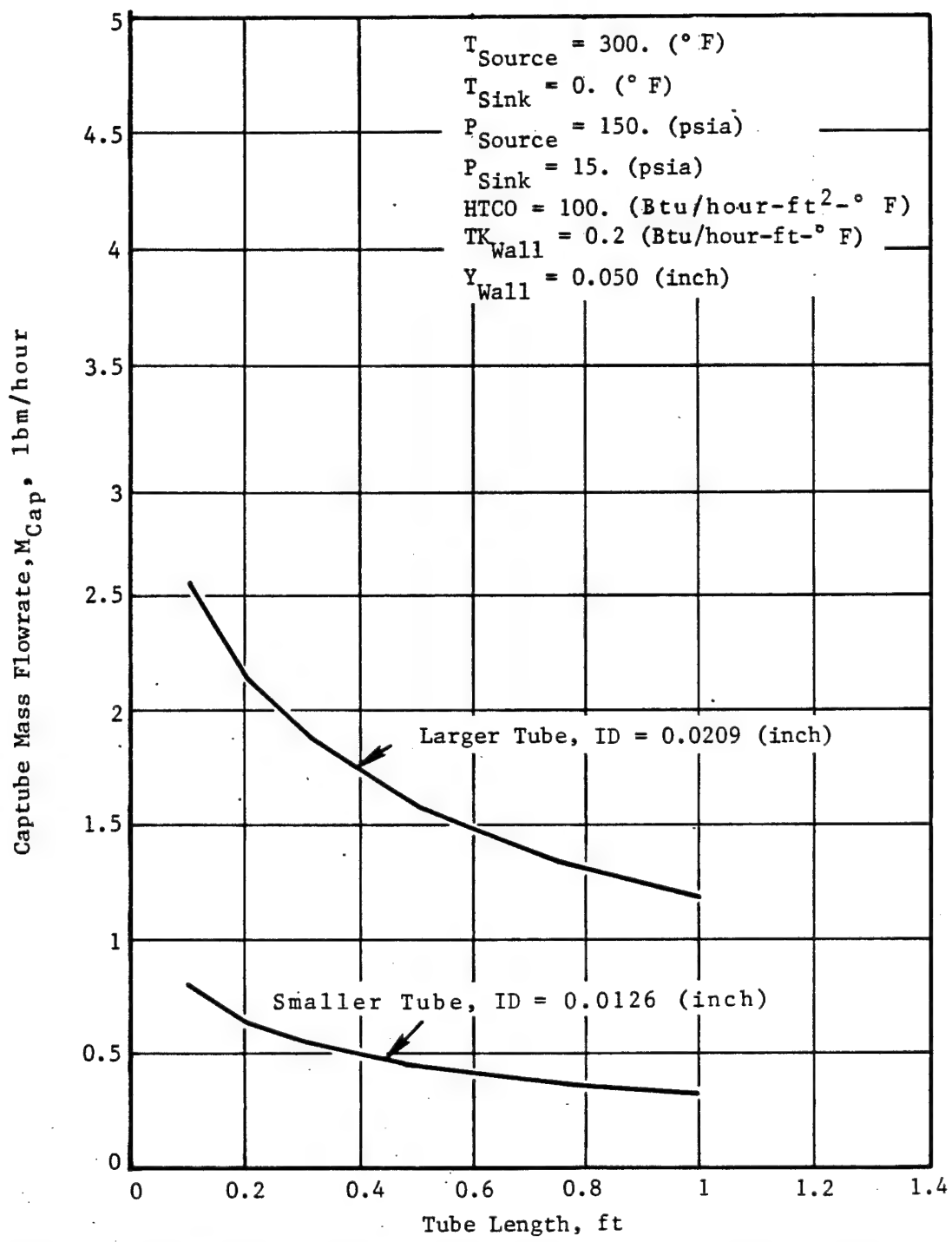
For example, the effects of capture diameter and length upon mass flowrate are shown in Figure 8. The parametric values listed at the top of Figure 8 were used for the calculations. The results show that values of MCAP are generally less than one lbm/hr for the smaller tube, and greater than one lbm/hr for the larger tube over a wide range of tube lengths. This means that the larger tube will have relatively small variations in wall surface temperature as illustrated at the higher mass flowrates shown in Figure 7.

SIMCAP results showing the effect of diameter on a capture having a length of one foot are plotted in Figures 9-12. Mach number distributions in the smaller and larger tubes are shown in Figure 9. Note that the larger tube has a larger inlet Mach number. Also, the exit Mach numbers are equal to one (both tubes are choked), and most of the Mach number increase occurs in the last 20% of the tube length.

The corresponding pressure distributions are plotted in Figure 10. Note that the exit pressure for these choked flows are 18.1 and 25.5 psia, both greater than the specified exhaust pressure of PSINK = 15 psia.

The corresponding capture air and wall surface temperature distributions are plotted in Figure 11. Note that the decrease in TWALL from tube inlet to exit is twice as great for the smaller tube as for the larger tube. Also note that the temperature distributions in Figure 11 curve downward near the tube exit, whereas the temperature distributions in Figure 7 have no such curvature. This is because the SIMCAP results plotted in Figure 11 include the effects of recovery temperature, variable air properties, and variable HTCI.

The effects of tube diameter and capture inlet temperature on HTCI are illustrated in Figure 12. Note that the larger tube has a value of HTCI about 20% greater than for the smaller tube, because of its greater mass flowrate. However, Figure 4 shows that this level of HTCI variation has a small influence upon wall temperature.



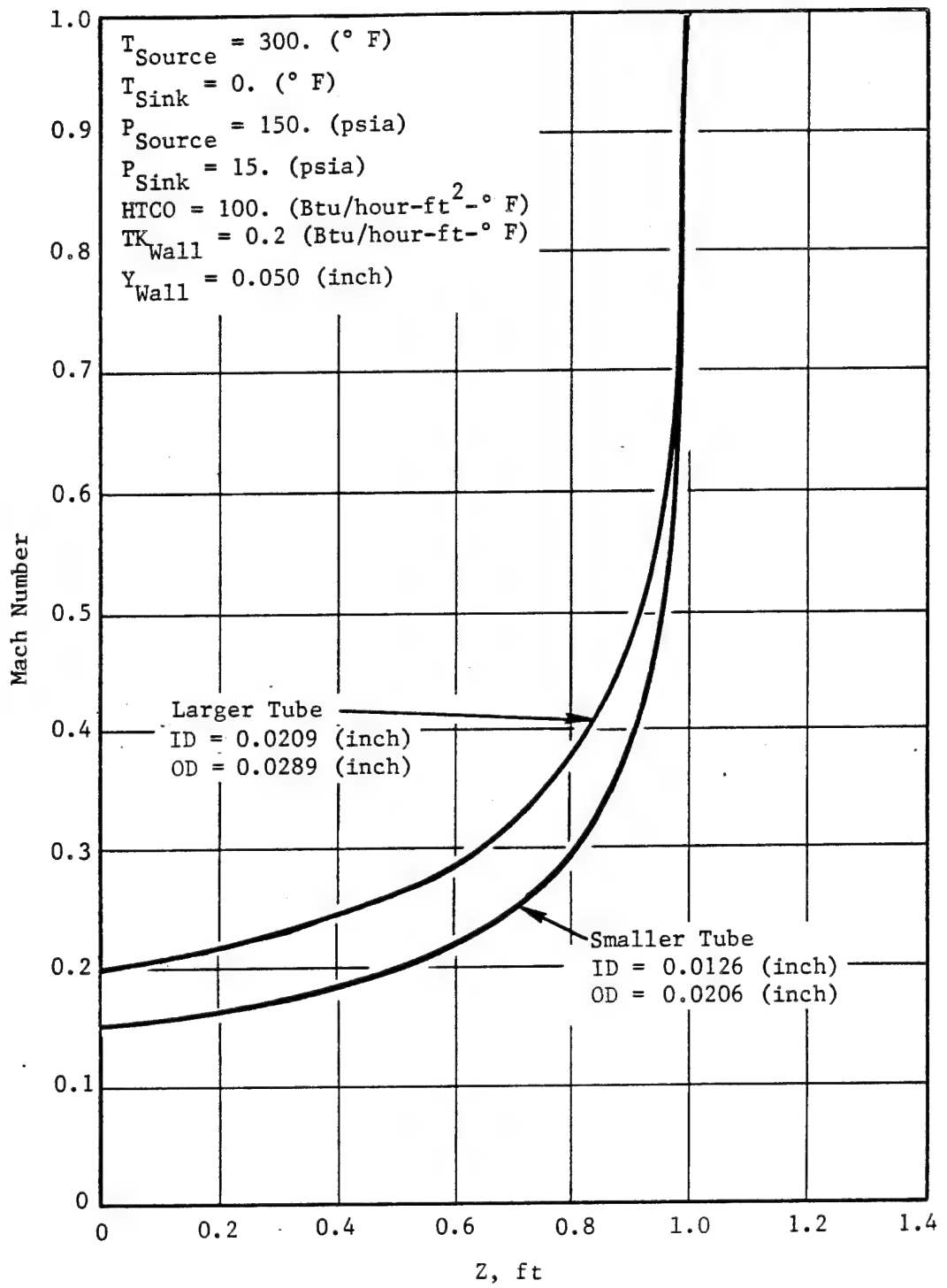


Figure 9. SS2D Captube Heat Transfer Model Effect of Tube Diameter on Mach Number Distribution.

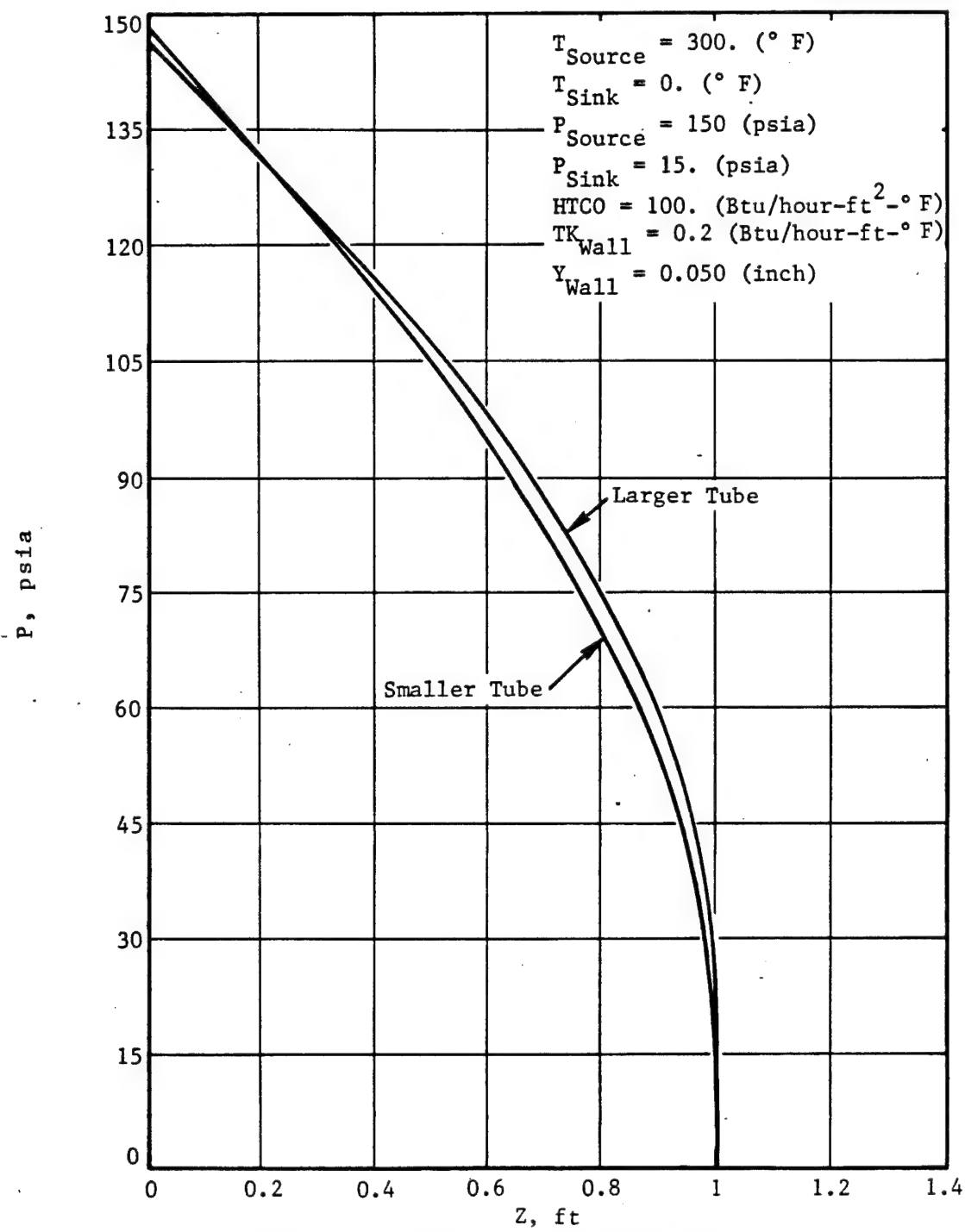


Figure 10. SS2D Captube Heat Transfer Model Effect of Tube Diameter on Pressure Distribution.

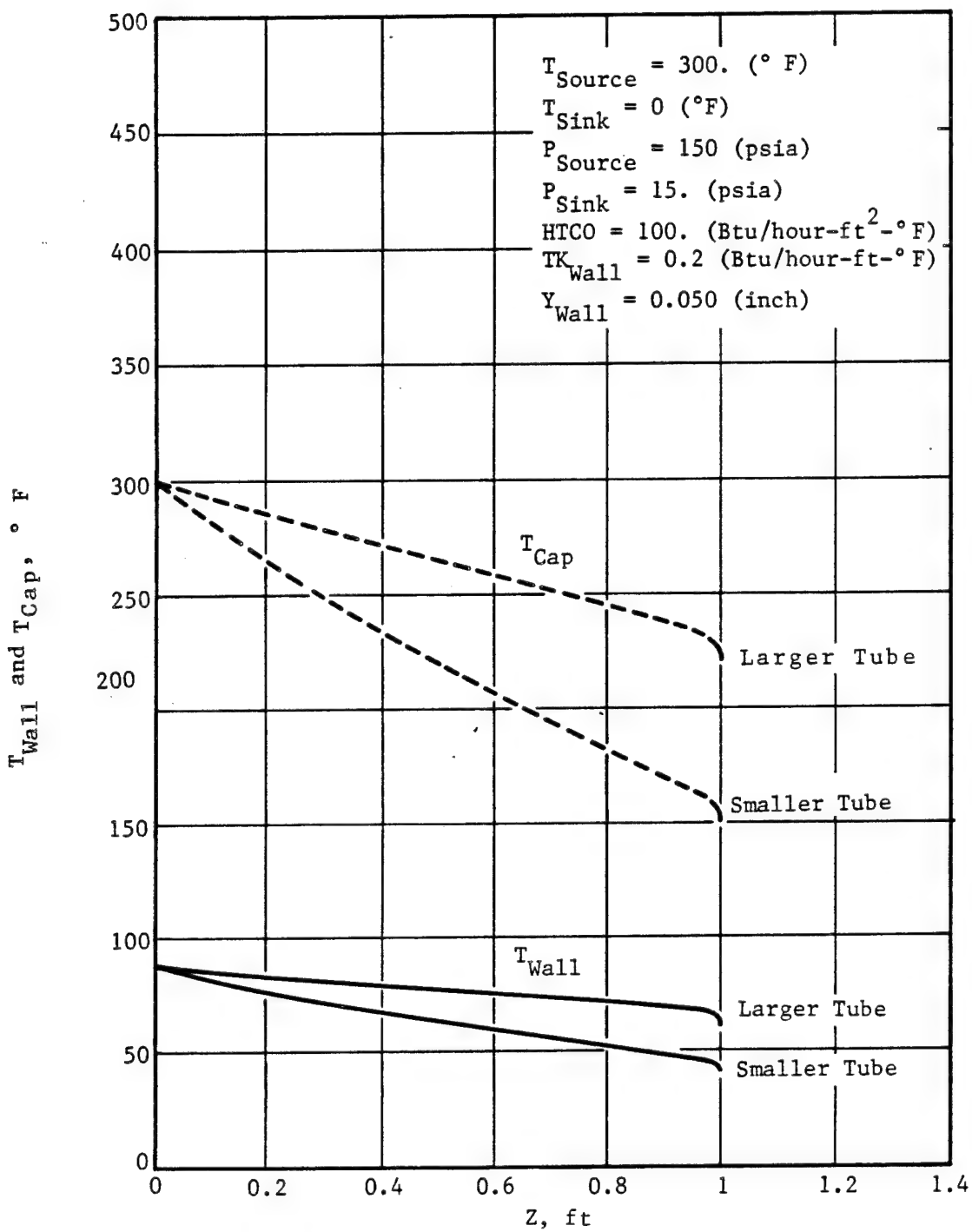


Figure 11. SS2D Captube Heat Transfer Model Effect of Tube Diameter on T_{Wall} and T_{Cap} .

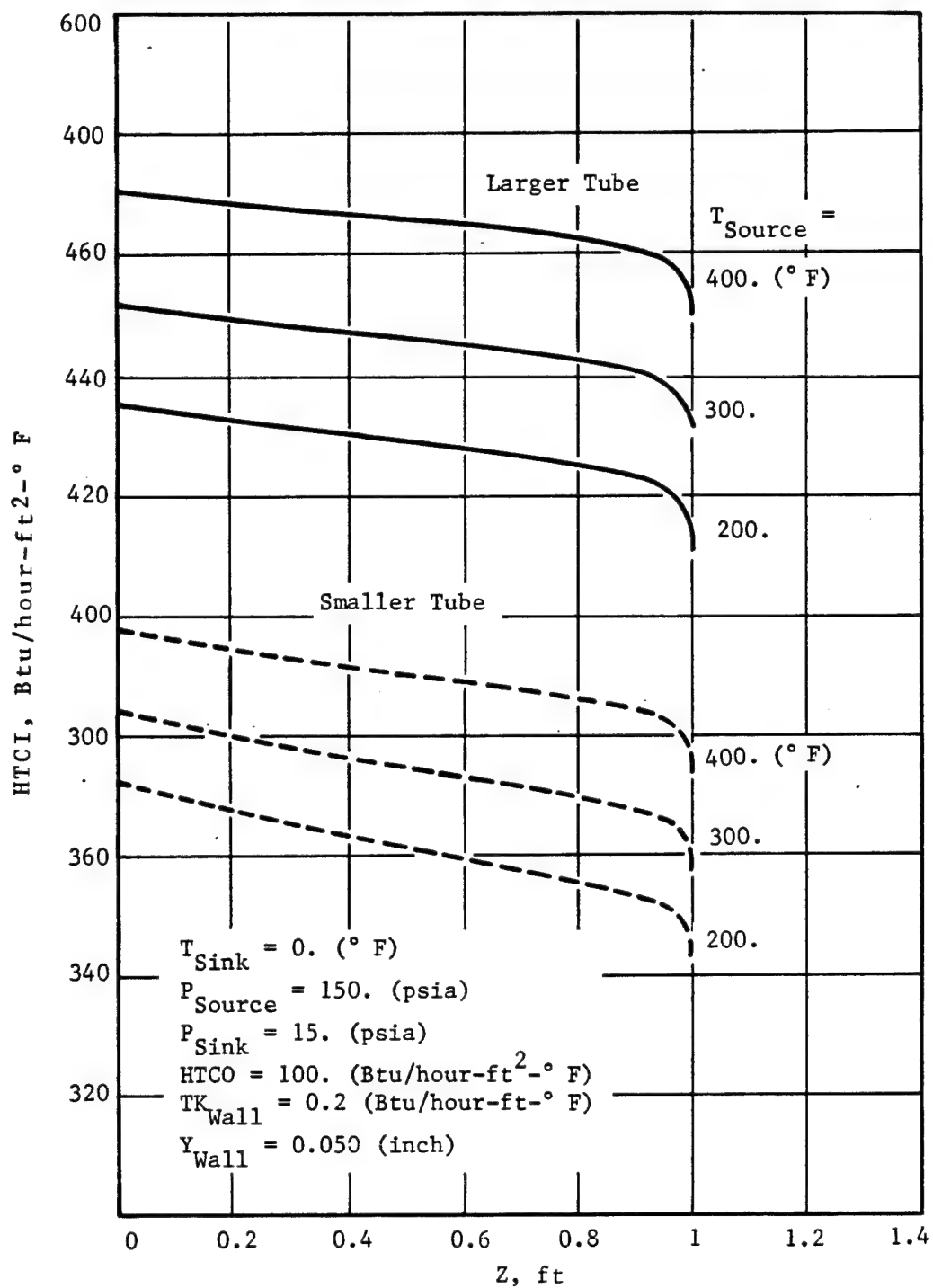


Figure 12. SS2D Captube Heat Transfer Model Effect of
Tube Diameter and T_{Source} on HTCI.

SIMCAP results showing the effects of PSOURCE, YWALL and HTCO on MCAP within the larger tube for a range of tube lengths are plotted in Figures 13, 14 and 15. These results show that PSOURCE has a big effect upon MCAP, as expected; however, YWALL and HTCO have a negligible effect upon MCAP.

Results showing the effects of PSOURCE, YWALL, and HTCO upon TWALL and TCAP distributions along the larger tube having a length of one foot are plotted in Figures 16, 17, and 18. These results show that YWALL and HTCO have a big effect upon the value of TWALL near the tube inlet, and a small effect upon the slope of the TWALL distribution. Conversely, PSOURCE has a negligible effect upon the value of TWALL at the tube inlet, and a significant influence upon the slope of the TWALL distribution.

The effects of PSOURCE, YWALL, and HTCO can be understood by considering Equations (14) and (15). That is, the primary effect of PSOURCE is to change MCAP which appears only in the argument of the exponential function in Equation (14). However, the primary effects of HTCO and YWALL are to change the thermal resistance terms (R_0 and R_{TOT}) which appear on the RHS of Equation (15) and influence the $z = 0$ intercept of the TWALL distribution.

This parametric study has demonstrated the capability and usefulness of the SIMCAP computer program. It has also demonstrated that Equations (14) and (15) can assist in interpreting the influence of design parameters upon capture performance.

The SIMCAP computer program developed here includes the following ten design parameters which are defined above in the text of the derivation: PSOURCE, TSOURCE, PSINK, TSINK, HTCO, YWALL, TKWALL, TKTUBE, tube diameter, and tube length. Negligible spacing between adjacent captubes is assumed; however, the model can be easily extended to include tube spacing. It is concluded here that the anti-icing ability of the larger tube is feasible, and its performance is much better than the smaller tube.

4.4 Experimental Test Panels

Five 2" x 2" x .05" graphite/epoxy panels with parallel clusters of capillary glass fibers bonded to one full surface were prepared with the following adhesive systems in order to select the most accomodating system for further evaluations.

1. HT-424
2. HT-424 Premeir
3. Metalbond 328
4. FM-123-2
5. 3109 (3M)

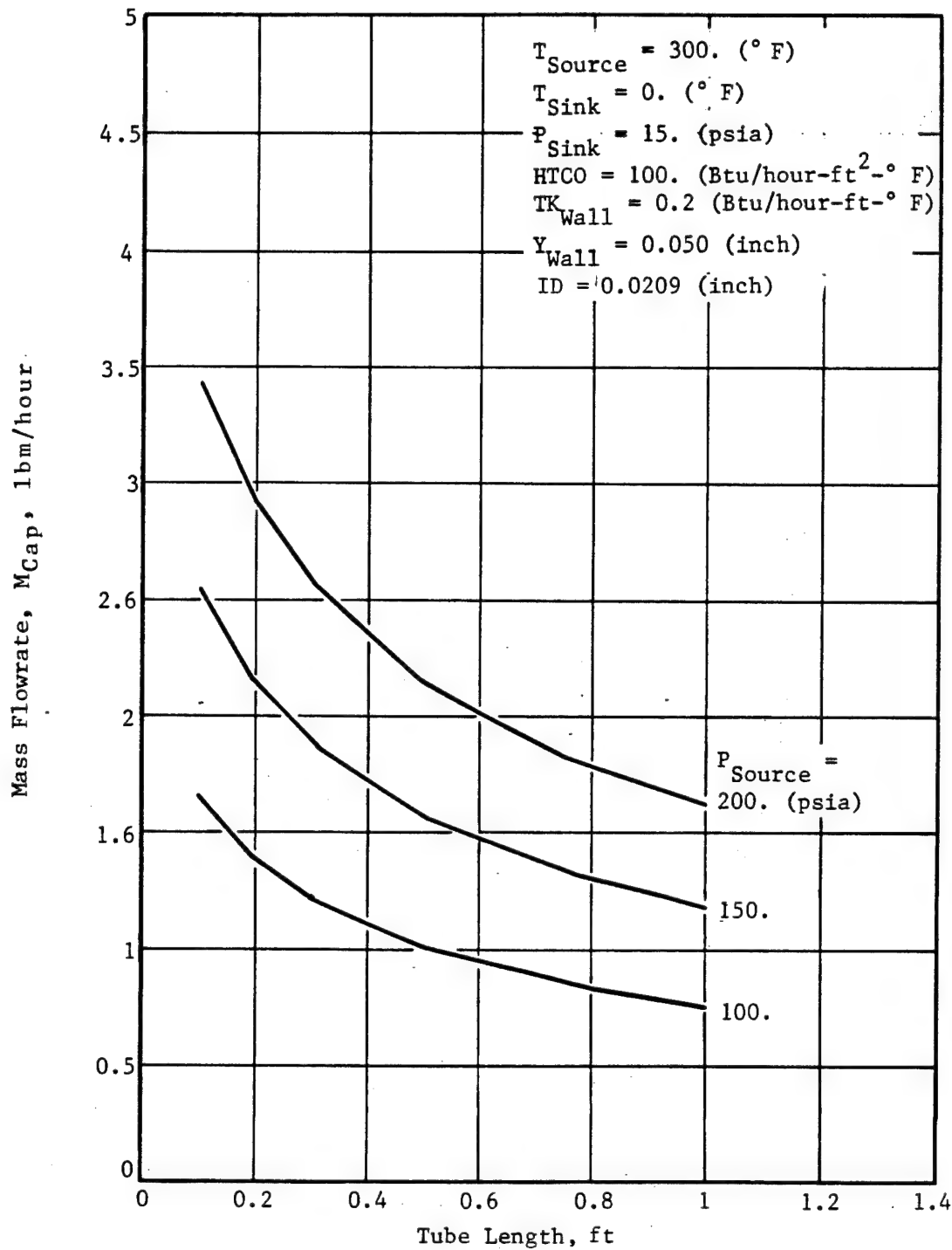


Figure 13. SS2D Captube Heat Transfer Model Effect of P_{Source} on M_{Cap} Within Larger Tube.

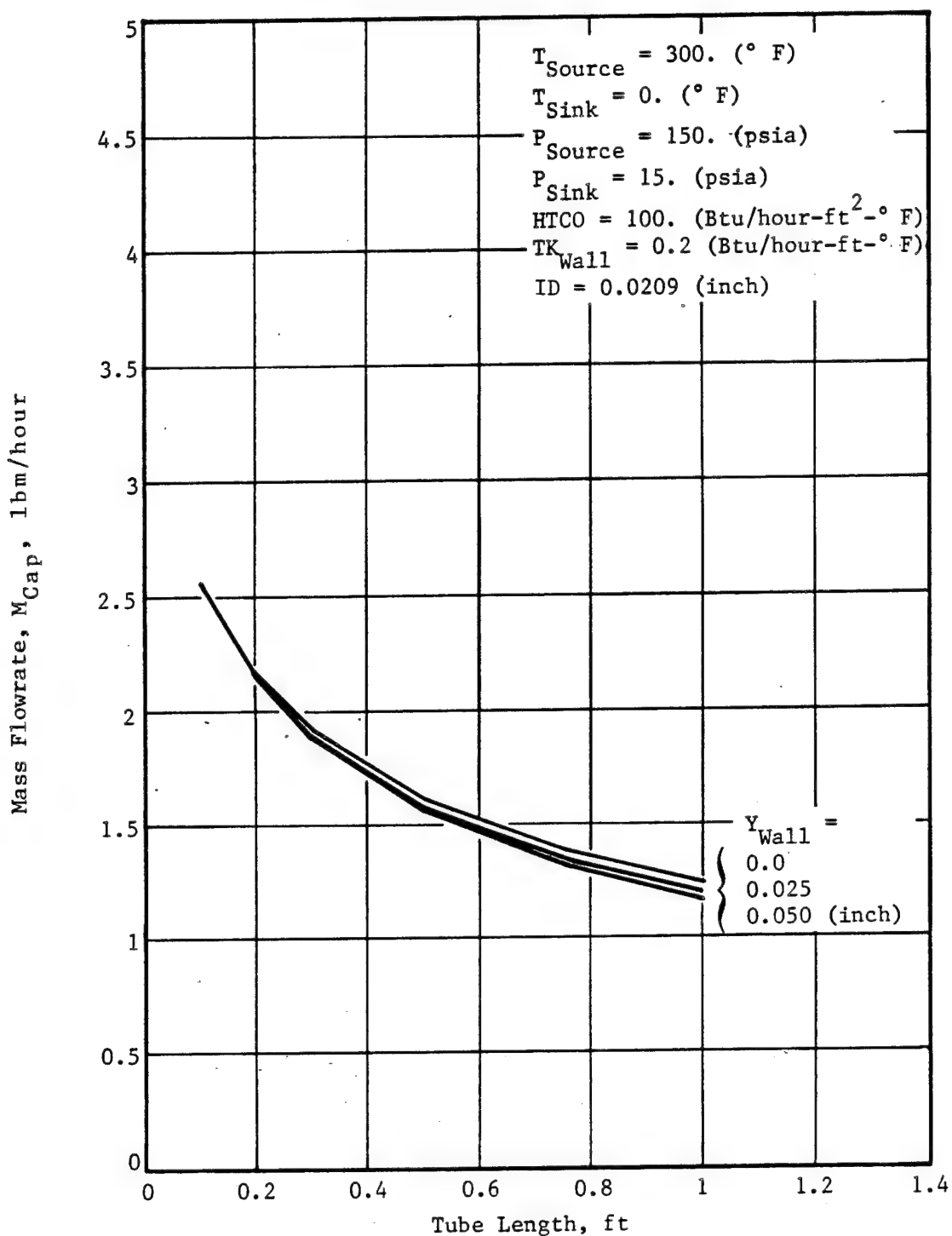


Figure 14. SS2D Captube Heat Transfer Model Effect of Y_{Wall} on M_{Cap} Within Larger Tube.

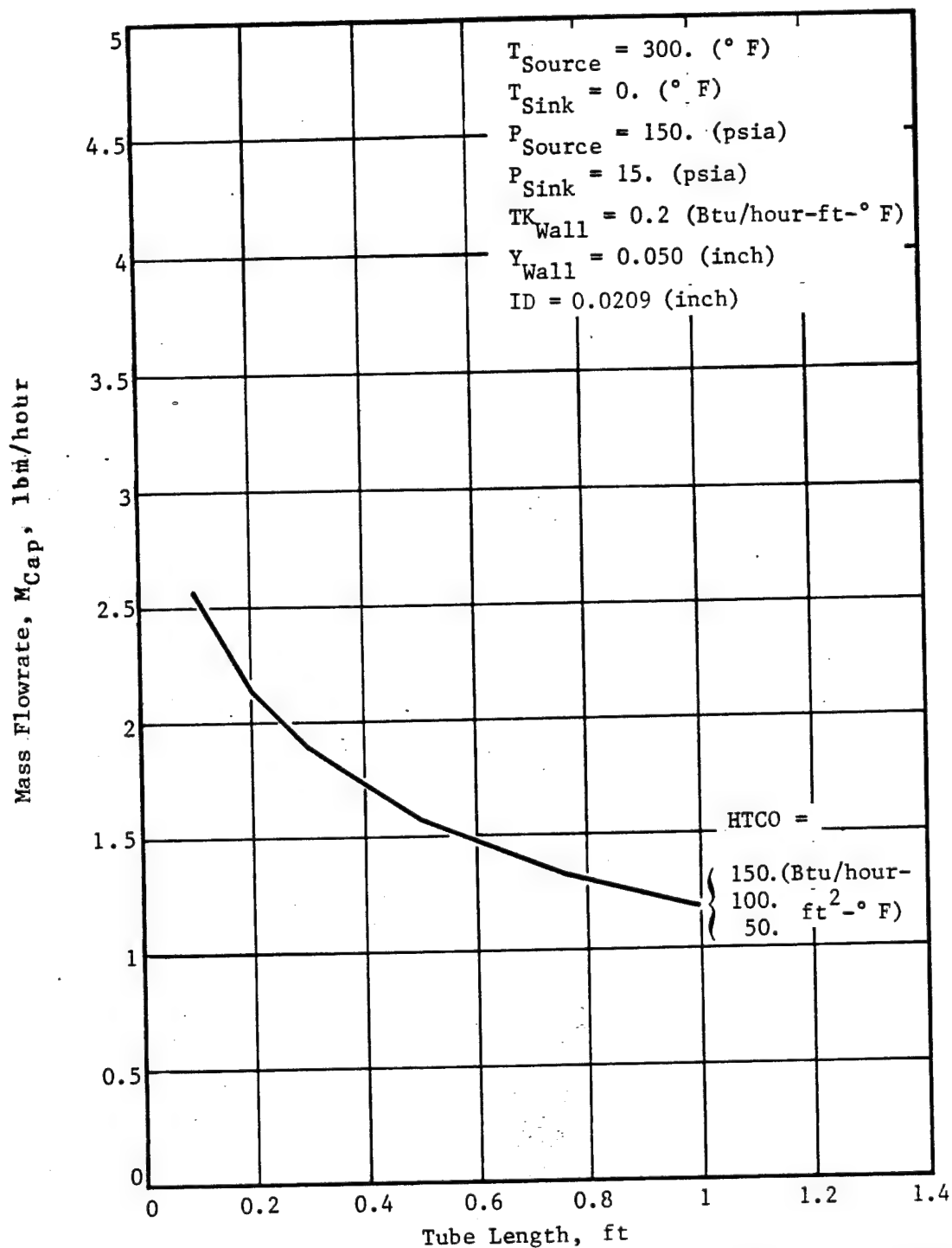


Figure 15. SS2D Captube Heat Transfer Model Effect of HTCO on M_{Cap} Within Larger Tube.

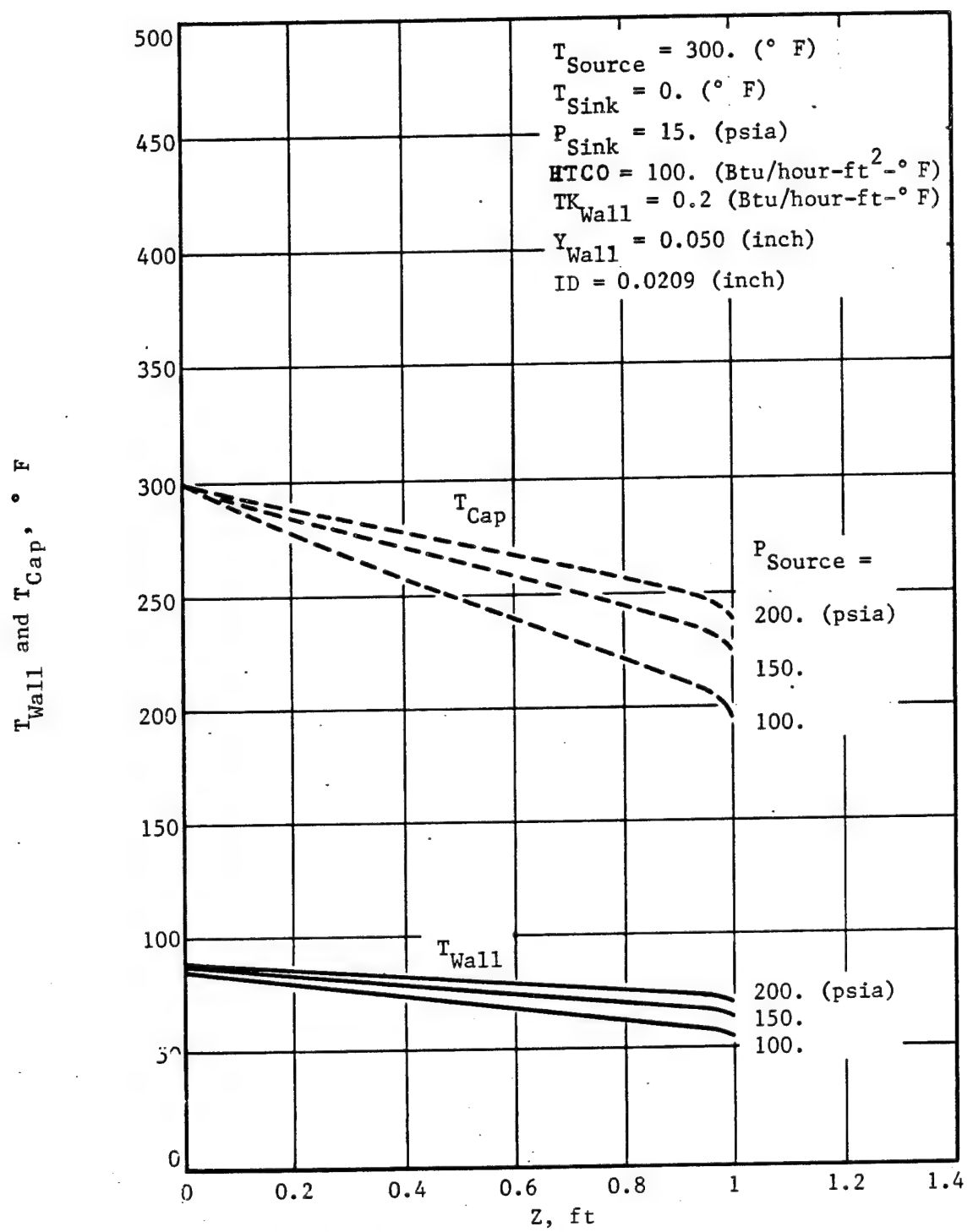


Figure 16. SS2D Captube Heat Transfer Model Effect of P_{Source} on T_{Wall} and T_{Cap} Within Larger Tube.

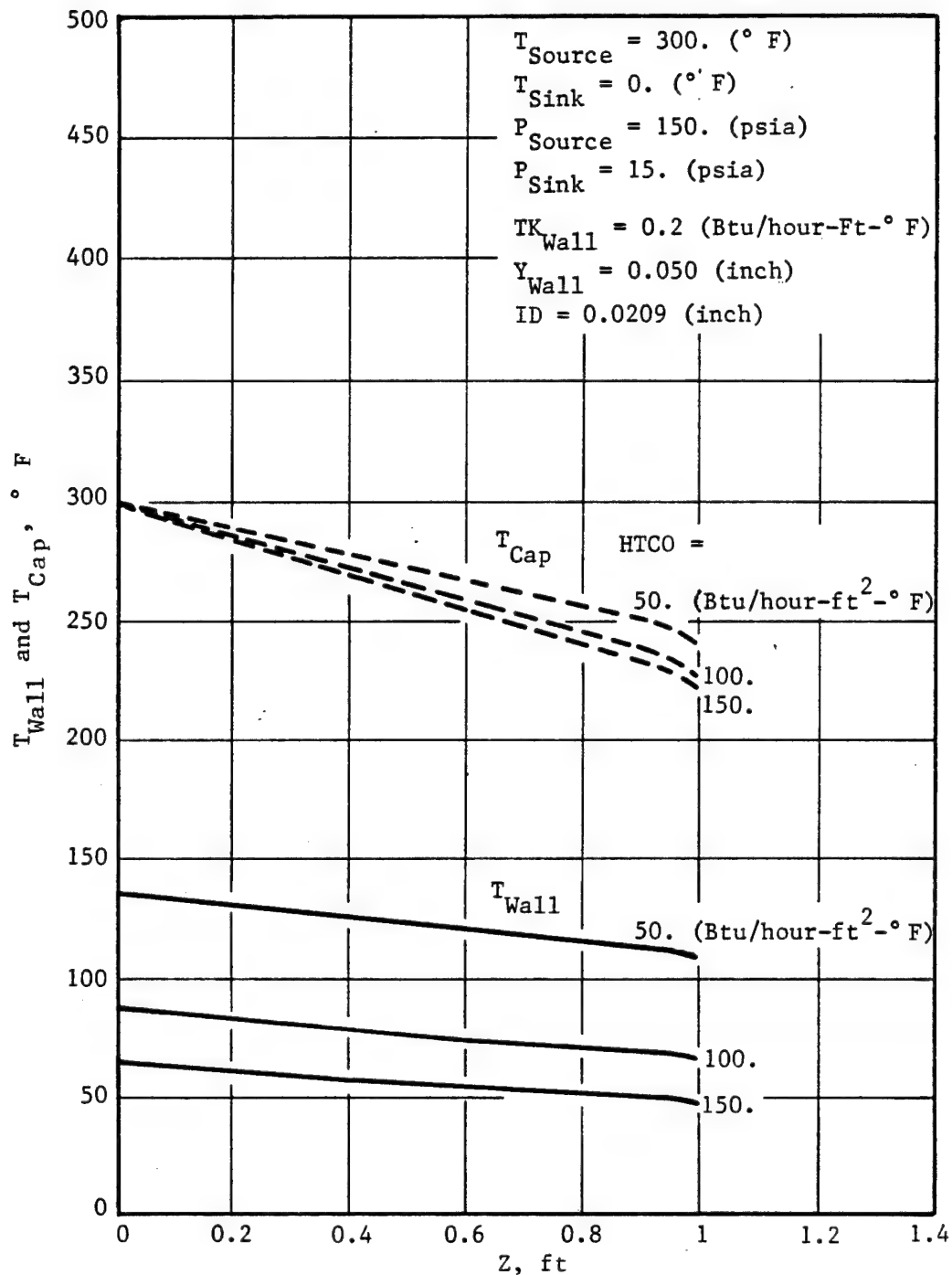


Figure 17. SS2D Captube Heat Transfer Model Effect of HTCO on T_{Wall} and T_{Cap} Within Larger Tube.

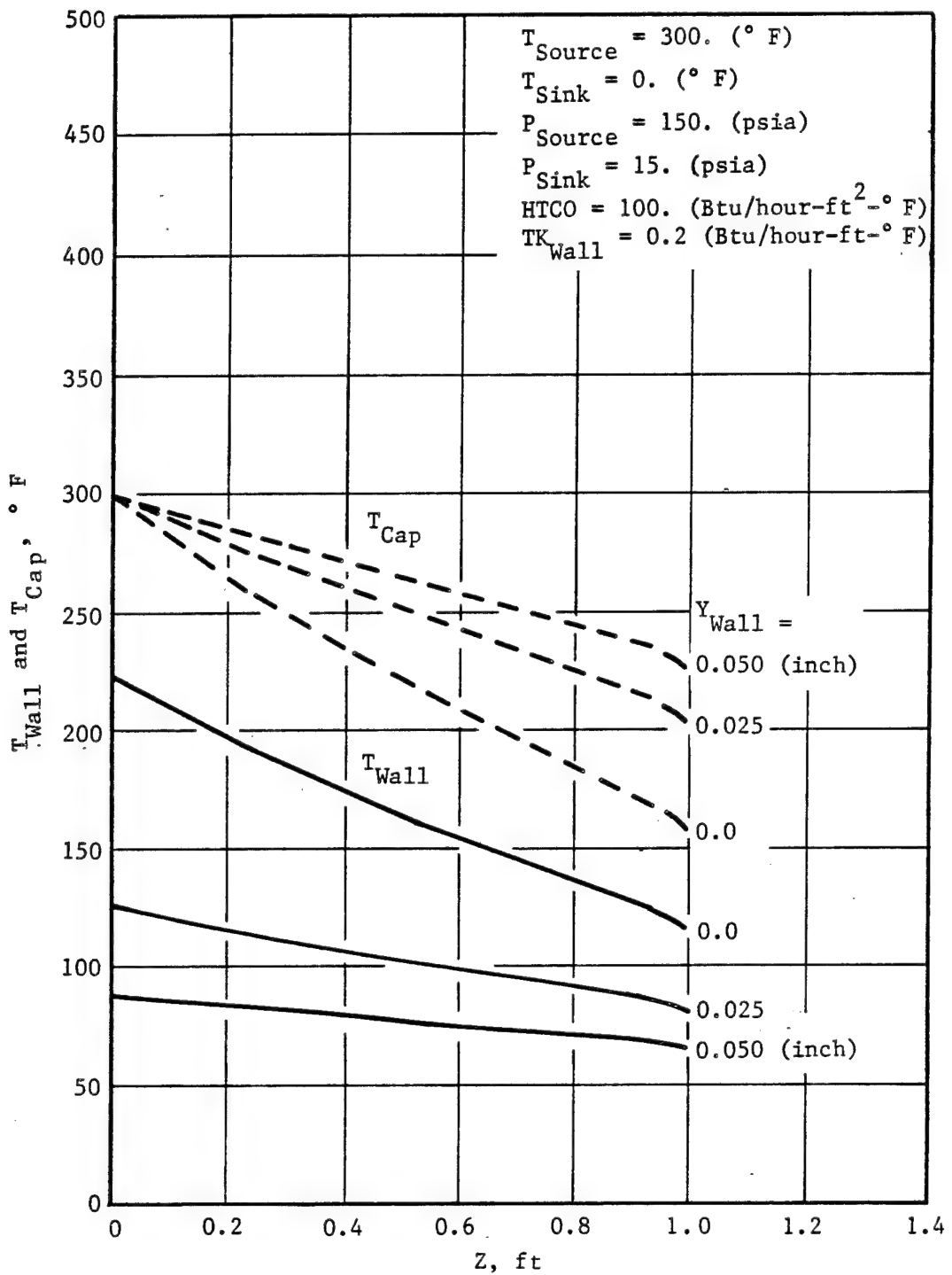


Figure 18. SS2D Captube Heat Transfer Model Effect of Y_{Wall} on T_{Wall} and T_{Cap} Within Larger Tube.

Cosmetically, all five panels looked good, however there was some concern that the aluminum in the first three panels might react electrochemically with the graphite over long duration. The fourth adhesive is limited to about 250°F service so with the prospect of 300°F compressor bleed air, it was dropped as a candidate. The 3109 adhesive from 3M will display 1250 psi shear at 300°F and has no galvanic concern, so it was selected for use on the eventual wind tunnel test panels.

Thermocouple instrumentation was then designed to fit within the physical geometry of one capillary tube for future panels. Work was initiated to provide a series of such thermocouples for integration in discreet areas of the array of cluster surface capillaries on the test panels. By keeping the thermocouples within the profile of a tube, they would not interfere with the laminar flow of test air. Figure 19 illustrates the final experimental wind tunnel panel designs.

A total of twenty-four special thermocouples were prepared (with 5 spares) for incorporation in the wind tunnel capillary tube test panels. The thermocouples were made by precision butt welding the wires end-to-end then benching away any weld flash at the joint. A very light touch of contrasting paint was applied directly at the weld joint so it would be easy to observe exactly where the thermocouple joint was being located during test panel assembly. Half of the thermocouples were made with thin wire and half with thick wire to match the respective 0.017 inch and 0.027 inch outside diameter of the capillary tubes being used for this program. The thermocouples were delivered to the fabricator where they were bonded in columnar array on graphite/PMP15 test panels using 3109 adhesive as illustrated in Figure 20 and 21. Four wind tunnel test panels were prepared. Two incorporated the 0.017 O.D. inch tubes and two had the 0.027 inch O.D. in the two respected 0° and 90° directions. Tubes initially extended about three inches beyond the edges of the panels to facilitate manifold connection.

4.5 Physical Properties of Test Panels

Two more 12-inch by 3-inch test panels of identical construction to the wind tunnel panels were prepared for physical evaluation as shown in Figure 22. Tensile, flexural, beam shear and compression tests were performed on these two panels which incorporate the 0.017-inch and 0.027-inch outside diameter tubing respectively. Figure 23 depicts the method of cutting the test specimen from these two panels. Cincinnati Testing Laboratory evaluated the physical properties of these two panels which are listed on their test data sheets in Figures 24 thru 28.

FINAL EXPERIMENTAL DESIGNS

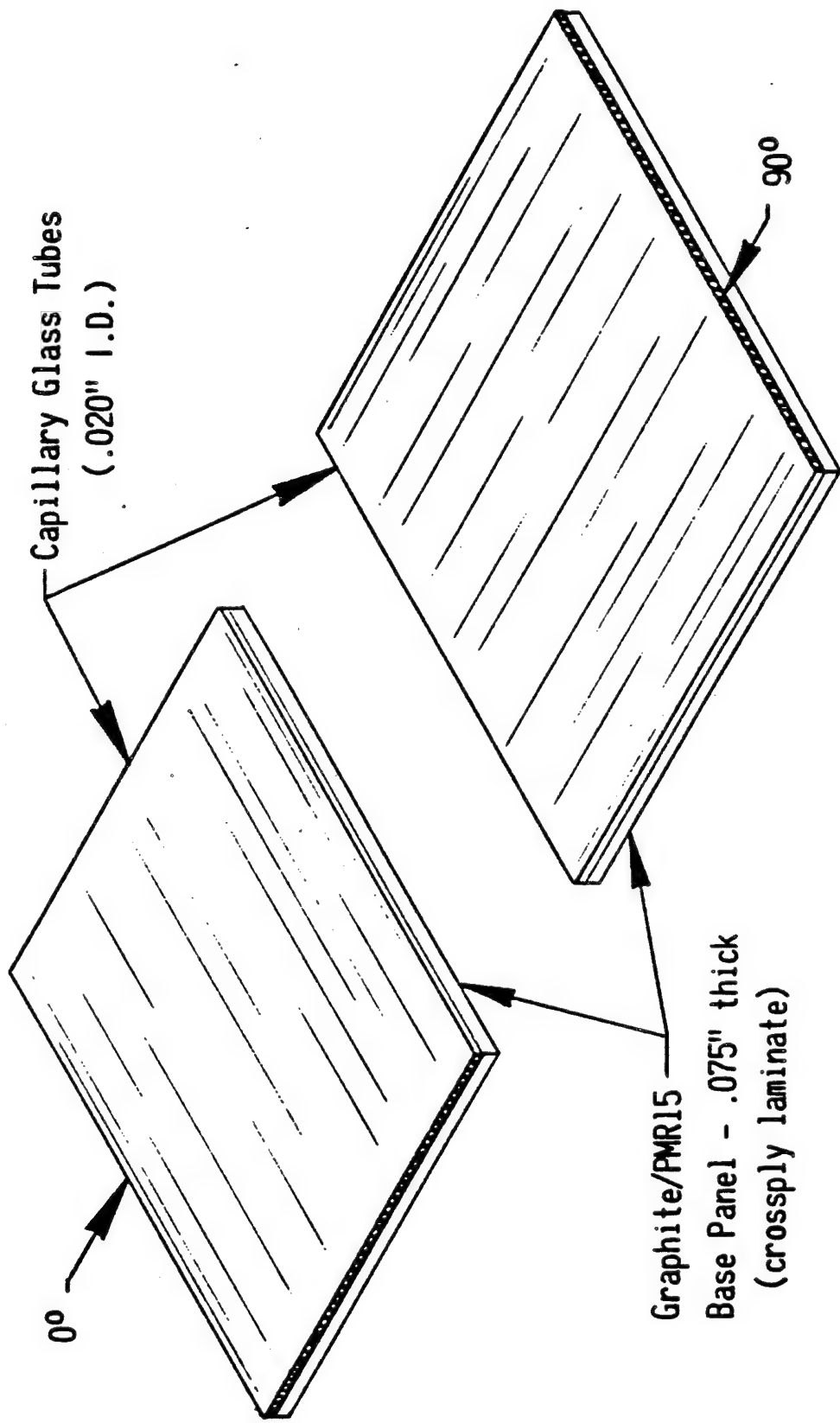


Figure 19

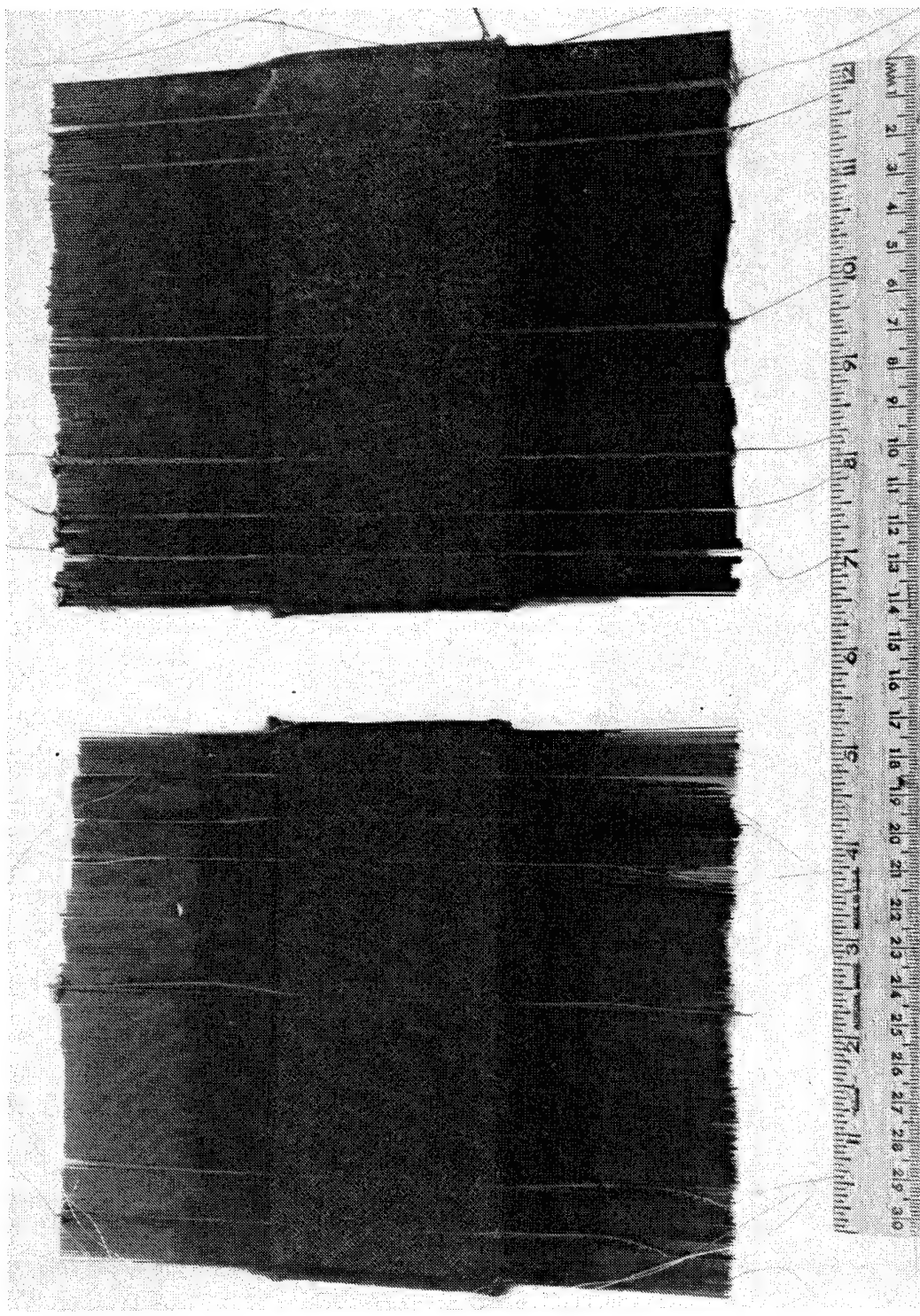


Figure 20 Wind Tunnel Test Panels, 90°.

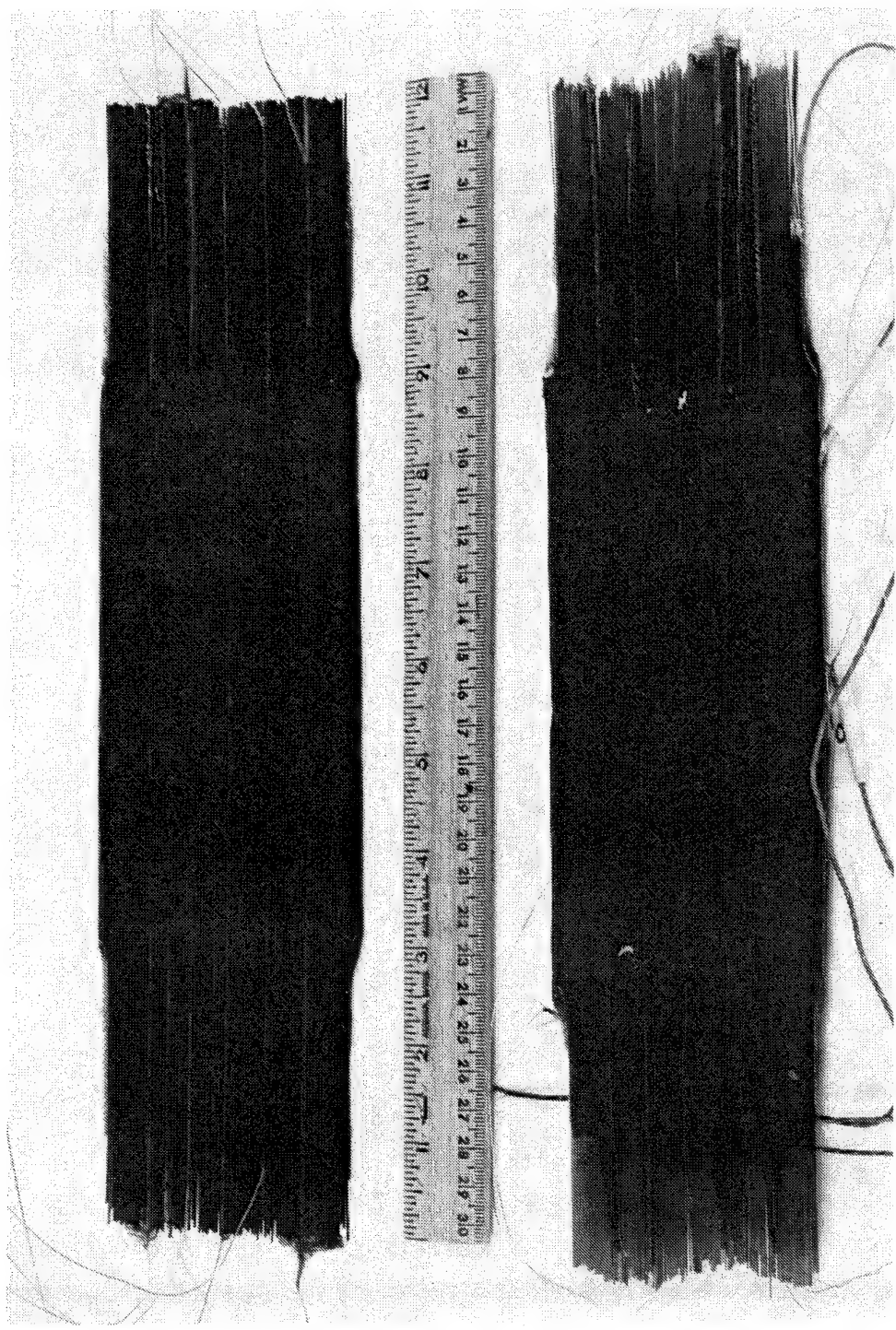


Figure 21 Wind Tunnel Test Panels, 0° .

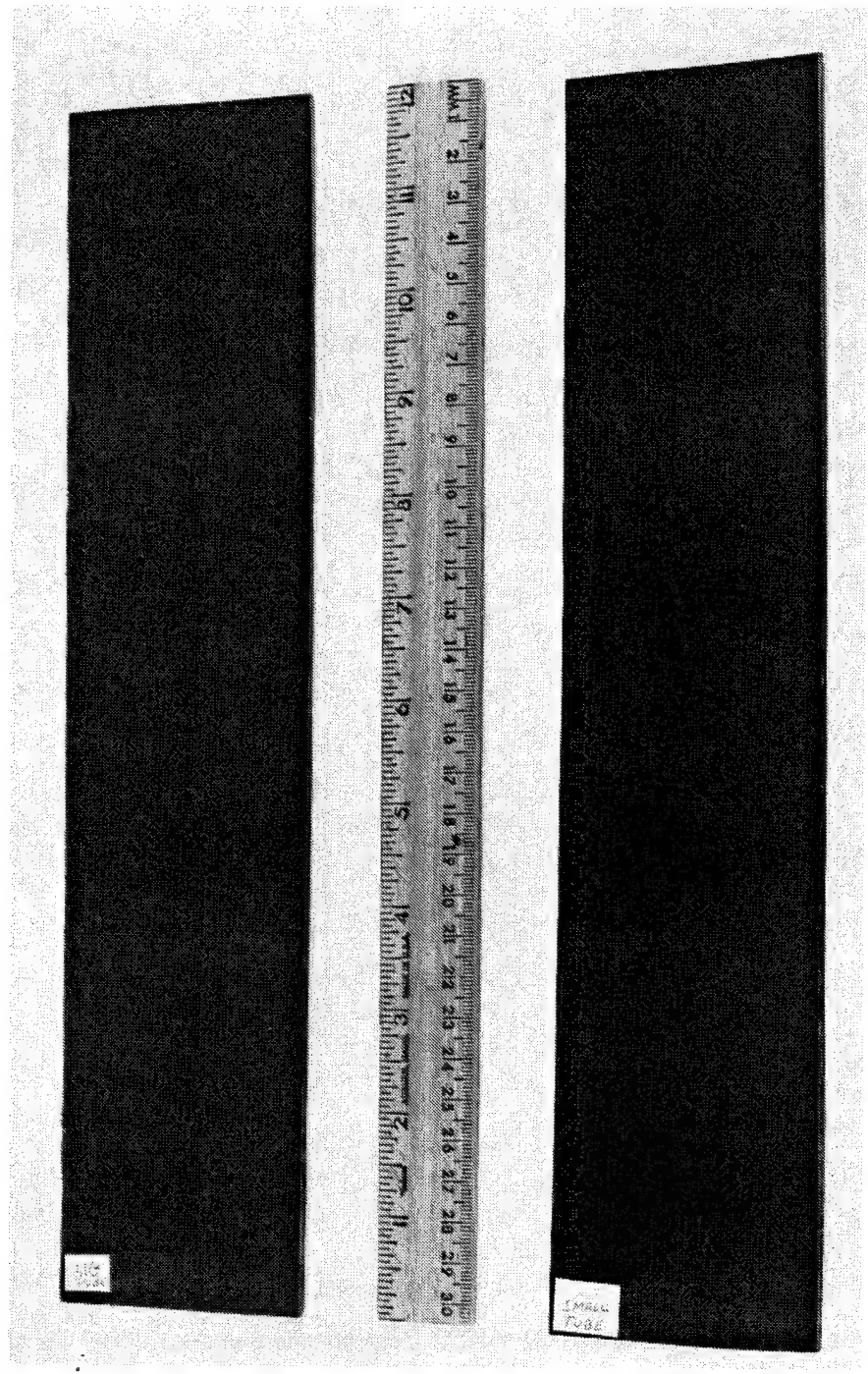
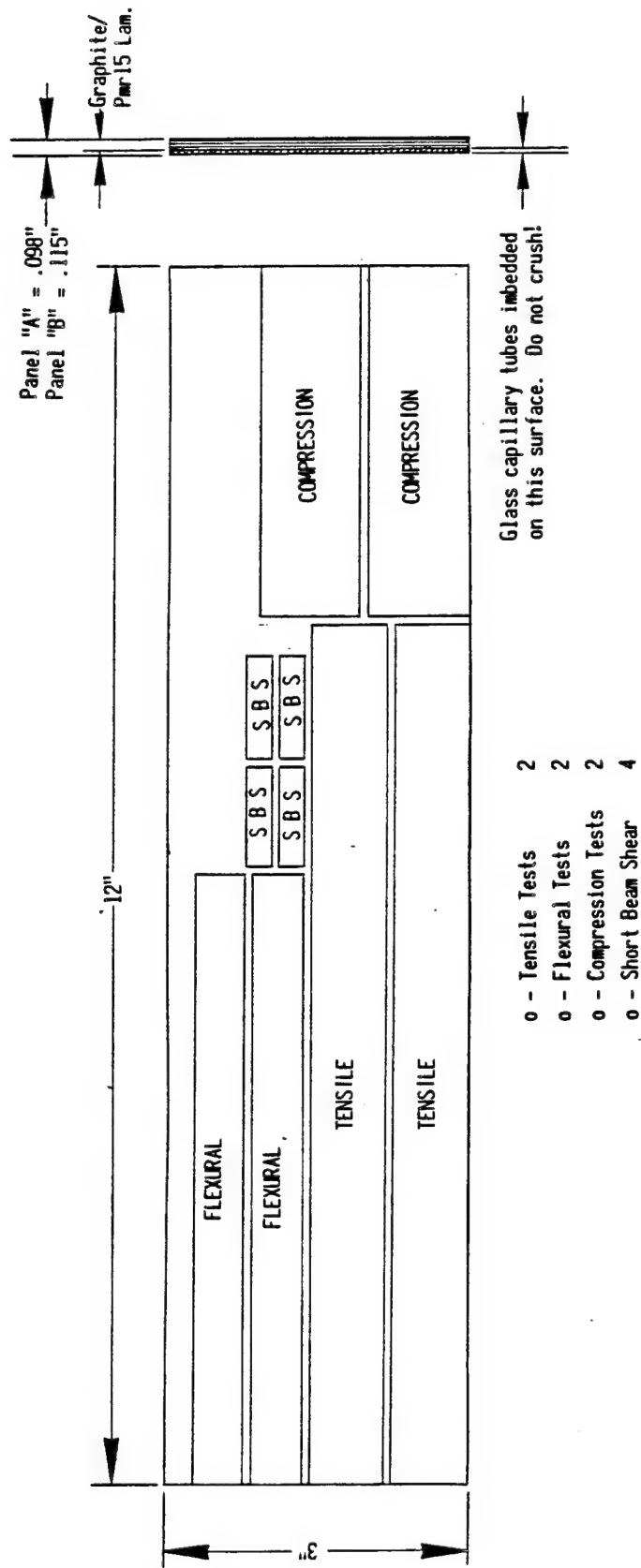


Figure 22 Tube Panels for Property Testing.



SK-31985

Refer: Lew Stoffer, 513 243-8178

Figure 23 Capillary Panel for Physical Test.

TEST REPORT



CINCINNATI TESTING LABORATORIES, INC.

REPORT NO. TO 6041

FLEXURAL STRENGTH

CUSTOMER: GENERAL ELECTRIC COMPANY

Date: April 23, 1985

Material: graphite PMR-15/glass capillary tubing (sk-31985) Panel A

Support radius: $\frac{1}{8}$ "

Specification: ASTM D790-81 (Method I)

Nose radius: $\frac{1}{4}$ "

Pre Conditioning: 40 hrs./23°C/50%R.H.

Test

Test Condition: 23°C/50%R.H.

Speed: .20 in./min.

Specimen length: $4\frac{1}{2}$ "

Span (L) 2.9 L/d Ratio: 32/1

 S = flexural strength in psi E_B = Modulus of elasticity in psi $\times 10^6$ P = Break load in lbs. b = specimen width in inches d = depth of beam in inches L = span in inches m = initial slope of load-deflection curve
in lbs./in.

$$\text{Flexural Strength (S)} = \frac{3PL}{2bd^2}$$

$$\text{Modulus of Elasticity (E}_B\text{)} = \frac{L^3m}{4bd^3}$$

Tubes	Specimen (No.)	S (psi)	d (in.)	b (in.)	P (lbs.)	m (lbs./in.)	E_B (psi $\times 10^6$)
own	A1	68,200	.089	.496	61.6	217	3.78
Up	A2	61,190	.086	.495	51.5	207	4.01
own	A3	42,470	.098	.497	46.6	237	3.09
	Avg.	57,290	.091				3.63

Respectfully Submitted

CINCINNATI TESTING LABORATORIES, INC.

417 NORTHLAND ROAD
CINCINNATI, OHIO 45240

Figure 24

37

Test Technician: J. Myers

J. Myers

Approved:

D. Browning

D. Browning

SBS

TEST REPORT



CINCINNATI TESTING LABORATORIES, INC.

REPORT NO. TO 6041

FLEXURAL STRENGTH

CUSTOMER: GENERAL ELECTRIC COMPANY

Date: April 23, 1985

Material: graphite PMR-15/glass capillary tubing (sk-31985) Panel B

Support radius: $1\frac{1}{8}$ "

Specification: ASTM D790-81 (Method I)

Nose radius: $1\frac{1}{4}$ "Pre Conditioning: 40 hrs./ 23°C /50%R.H.

Test

Test Condition: 23°C /50%R.H.Speed: .20 in./min.
Specimen length: $4\frac{1}{2}$ "

Span (L) 3.6 L/d Ratio: 32/1

S = flexural strength in psi

 E_B = Modulus of elasticity in psi $\times 10^6$

$$\text{Flexural Strength (S)} = \frac{3PL}{2bd^2}$$

P = Break load in lbs.

$$\text{Modulus of Elasticity (E}_B\text{)} = \frac{L^3m}{4bd^3}$$

b = specimen width in inches

d = depth of beam in inches

L = span in inches

m = initial slope of load-deflection curve
in lbs./in.

Tubes	Specimen (No.)	S (psi)	d (in.)	b (in.)	P (lbs.)	m (lbs./in.)	E_B (psi $\times 10^6$)
Down	B1	41,340	.111	.494	46.6	194	3.35
Up	B2	62,820	.108	.493	66.9	186	3.49
Down	B3	40,440	.118	.492	51.3	190	2.74
	Avg.	48,200	.112				3.19

Respectfully Submitted

CINCINNATI TESTING LABORATORIES, INC.

417 NORTHLAND ROAD
CINCINNATI, OHIO 45240

Figure 25

Test Technician:

38

Approved:
D. Browning SBS

TEST REPORT



CINCINNATI TESTING LABORATORIES, INC.

REPORT NO. TO 6041

COMPRESSIVE STRENGTH

CUSTOMER: GENERAL ELECTRIC COMPANY

Date: April 23, 1985

Material: graphite PMR-15/glass capillary tubing (sk-31985) Panels A & B

Specification: ASTM D695-80

Testing Speed: .05 in./min.

Pre-Conditioning: 40 hrs./23°C/50%R.H.

Test Condition: 23°C/50%R.H.

Specimen Type: dogbone (fig. 5)

S = Compression strength in psi

 $E_c = \text{Modulus of elasticity in psi} \times 10^6$

P = break load in lbs.

b = specimen width in inches

d = specimen thickness in inches

Y = strain in in./in.

Specimen (No.)	S (psi)	P (lbs.)	d (in.)	b (in.)	E_c (psi $\times 10^6$)
A 1	37,090	1592	.085	.505	4.69
A 2	39,270	1702	.086	.504	4.51
AVG	38,180				4.60
B 3	43,650	2319	.105	.506	4.04
B 4	46,160	2466	.106	.504	4.17
Avg.	44,910				4.11

Respectfully Submitted

CINCINNATI TESTING LABORATORIES, INC.

417 NORTHLAND ROAD
CINCINNATI, OHIO 45240

Figure 26

Test Technician:

J. Myers

39

Approved:

D. Browning

TEST REPORT



CINCINNATI TESTING LABORATORIES, INC.

REPORT NO. TO 6041

TENSILE STRENGTH

CUSTOMER: GENERAL ELECTRIC COMPANY Date April 23, 1985
 Material: graphite PMR-15/glass capillary tubing (sk-31985) Panels A & B
 Specification: ASTM D638-82a
 Pre Conditioning: 40 hrs/23°C/50%R.H. Testing Speed: 0.20 in./min.
 Test Condition: 23°C/50%R.H.
 Specimen Type: I

S = Ultimate Tensile Strength in PSI

Sy = yield strength in PSI

Et = modulus of elasticity in PSI $\times 10^6$

P = break load in lbs.

b = specimen width in inches

d = specimen thickness in inches

Y = strain in in./in.

@ break

Specimen (no.)	S (PSI)	Sy (PSI)	P (lbs.)	d (in.)	b (in.)	Et (psi $\times 10^6$)	Elongation (%)
A1	35,430		1747	.099	.498	3.85	0.94
A2	35,950		1758	.098	.499	3.82	1.00
AVG	35,690					3.84	0.97
B3	34,400		1962	.115	.496	3.91	* 0.89
B4	33,150		1944	.118	.497	3.67	0.96
Avg.	33,780					3.79	0.93

Respectfully Submitted

*Failed outside 2" gage

CINCINNATI TESTING LABORATORIES, INC.

417 NORTHLAND ROAD
CINCINNATI, OHIO 45240

Figure 27

Test Technician:

J. Myers

40

Approved:

D. Browning

TEST REPORT



CINCINNATI TESTING LABORATORIES, INC.

Report No. TO 6041

SHORT BEAM SHEAR

CUSTOMER: GENERAL ELECTRIC COMPANY Date: April 23, 1985
 Material: graphite PMR-15/glass capillary tubing (sk-31985) Panels A & B
 Specification: ASTM D2344-76

Pre Condition: 40 hrs./23°C/50%R.H. Test Speed: .05 in./Min.

L/d ratio: 5/1

Test Temp: 23 °C Rel. Humid. 50 % Specimen Size: $\frac{1}{4}$ "x $\frac{3}{4}$ " Load Points Radius: $\frac{1}{8}$ " nose
 $\frac{1}{16}$ " supports

Specimen (No.)	Thickness-d (in.)	Width-b (in.)	Break Load (lbs.) - P	Shear Strength: $S = \frac{3P}{4bd}$ PSI	Span: .485"
A 1	.097	.259	185	5520	
A 2	.096	.263	150	4460	
A 3	.098	.259	193	5700	
A 4	.097	.266	150	4360	

Code: Panel A

Avg. S = 5010 PSI

Specimen (No.)	Thickness-d (in.)	Width-b (in.)	Break Load (lbs.) - P	Shear Strength: $S = \frac{3P}{4bd}$ PSI	Span: .570"
B 1	.114	.252	240	6270	
B 2	.112	.258	156	4050	
B 3	.115	.251	225	5850	
B 4	.113	.259	140	3590	

Code: Panel B

Avg. S = 4940 PSI

Respectfully Submitted,

CINCINNATI TESTING LABORATORIES, INC.

417 NORTHLAND ROAD
 CINCINNATI, OHIO 45240

Figure 28

Test Technician: T. Burns
 T. Burns

41

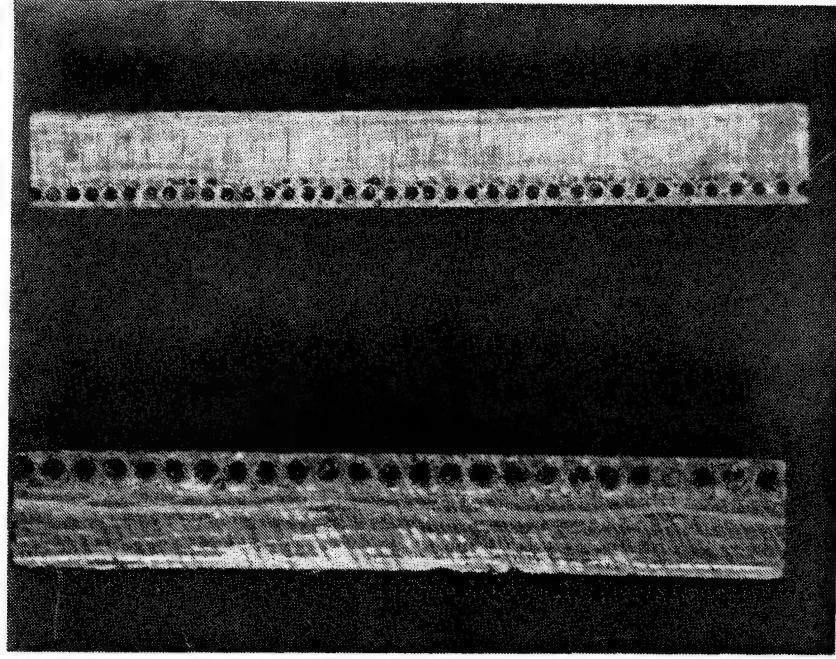
Approved:

D. Browning
 D. Browning SBS

Panel A as referred to in Figures 24 through 28, was composited with the smaller 0.012 inch I.D. tubes and Panel B had the larger 0.020 inch I.D. tubes. The test identified "down" or "up" refers to which side the bonded tubes were placed during testing. Figure 29 shows a microphotograph of sections taken from both panels. In each case, test failure was typical with no unexpected results. However, conclusions expressed at the end of this report caution against relying on any physical influence from the bonded tubes due to long term stress corrosion and contamination corrosion that may occur within the tubes.

In addition to the fabrication of composite panels with capillary tubes on one surface, an all-capillary tube panel was also fabricated under this program as a possible means for displaying isolated material properties of captubes alone.

An order was placed to fabricate a 3ply $0^\circ/90^\circ$ all tube panel 9-inches by 7-inches for delivery to the NASA Project Manager as required by Task II-C. This panel, illustrated in Figure 30 together with the tested panels described above constitute an excess of the one square foot (active surface) of capillary reinforced composites to be submitted to the NASA Project Manager at the completion of this program.



Microphotograph of Capillary Tube Panels Showing
0.012 inch ID Tubes Above and 0.020 inch
Tubes Below

Figure 29

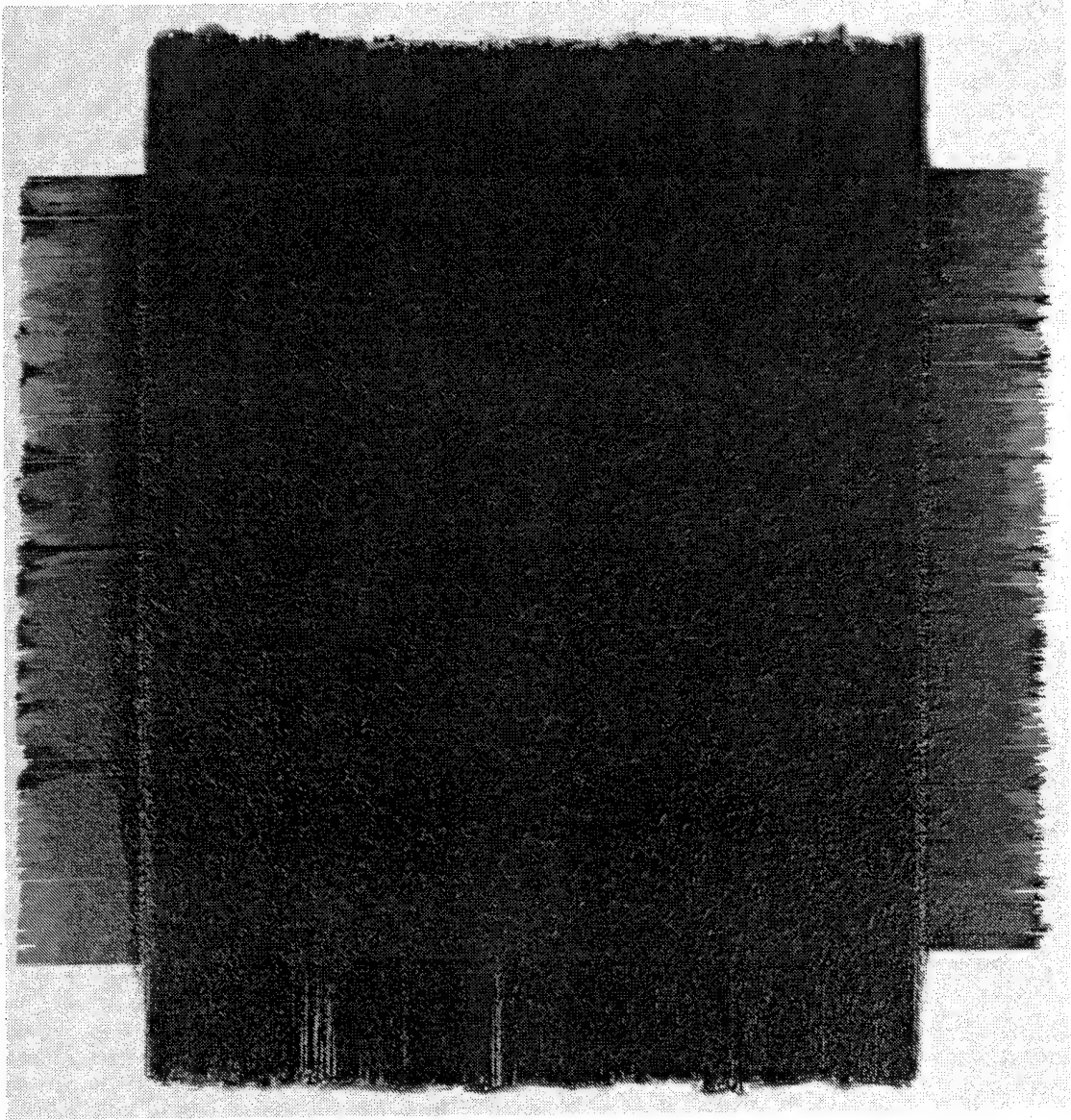


Figure 30. Cross Ply Capillary Tube Test Panel.

5.0 Wind Tunnel Test Rig

In order to simulate an isolated engine inlet arrangement, a wind tunnel test rig was designed with a six inch test section as illustrated in Figure 31. A "Sodium Chloride Window" would allow undiminished monitoring of infra-red detail during testing. The capillary tubes would emerge into the two manifold sections as shown with rubber sealing their respective connection to either manifold. The 40/60% screen blockage in the air supply plenum would act to smooth out airflow turbulence before it enters the test section.

A satisfactory method for manifolding the ends of the capillary tubes for the wind tunnel tests was worked out as illustrated in Figure 32. The tubes were cut off flush with the edge of the base graphite/PMR15 test panel, then a clamp bracket was capped over the top surface of the clustered tubes to create a flow path into each manifold. Some plastic filler caulking material was applied to smooth the transition areas as indicated.

The wind tunnel test rig was fabricated as illustrated in Figures 33, 34 and 35. Figure 35 shows the interior of the feed air plenum with porous interior wall intended to even-out the feed air turbulence which enters equally from four walls. Figure 36 shows the wind tunnel test rig set up. Figure 37 and 38 show the capillary tube panel manifold box which fits to the opening in the wind tunnel. The original plan to simply bend the tubes into slots feeding air to and from the manifold plenum chambers did not work. The tubes broke where they joined the rigid panel. Earlier tests showed that the tubes could be bent to the required radius, but it was found that after the tubes were composited into panels, the excess resin that flowed out along the tubes changed their bending characteristics such that they broke when forced into the required radius necessary to penetrate the plenum slots. Accordingly, another approach was investigated that allowed the tubes to be cut off abruptly at the edges of the test panel exactly where the tubes broke.

5.1 Wind Tunnel Testing

Wind tunnel testing was initiated and several points were taken before an air leak was detected in the vicinity of the test panel. In order to repair the leak, it was necessary to remove the test section manifold/panel system from the wind tunnel. It was then discovered that the test panel was warped severely in two directions. The side with the 3 inch glass tubes bonded in the parallel cluster simply expanded in both directions. In the 6 inch direction, the center was lifted about 3/16 inch and in the 3 inch direction the center was lifted about 1/16 inch relative to the bowed

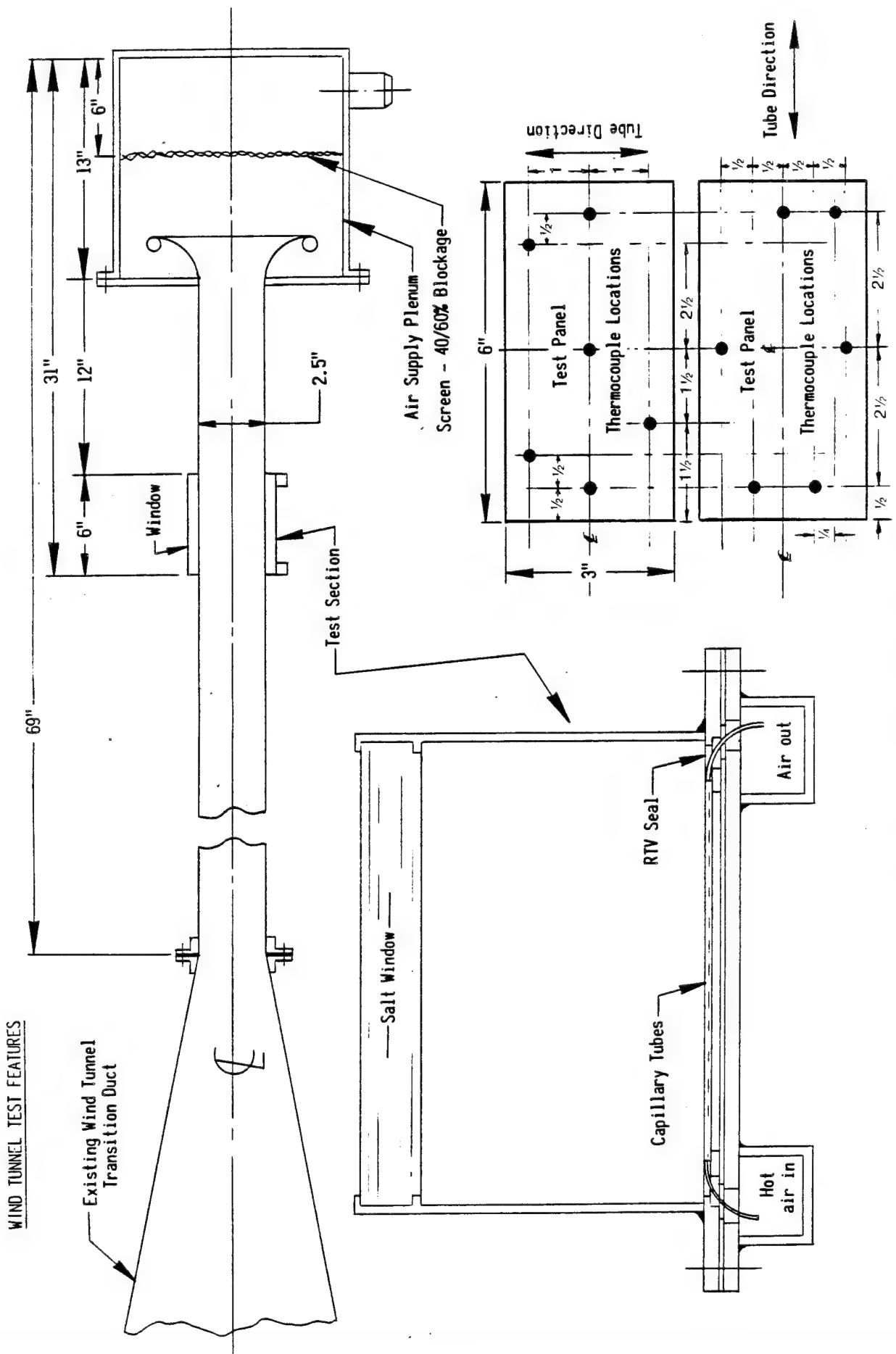


Figure 31 Wind Tunnel Test Features.

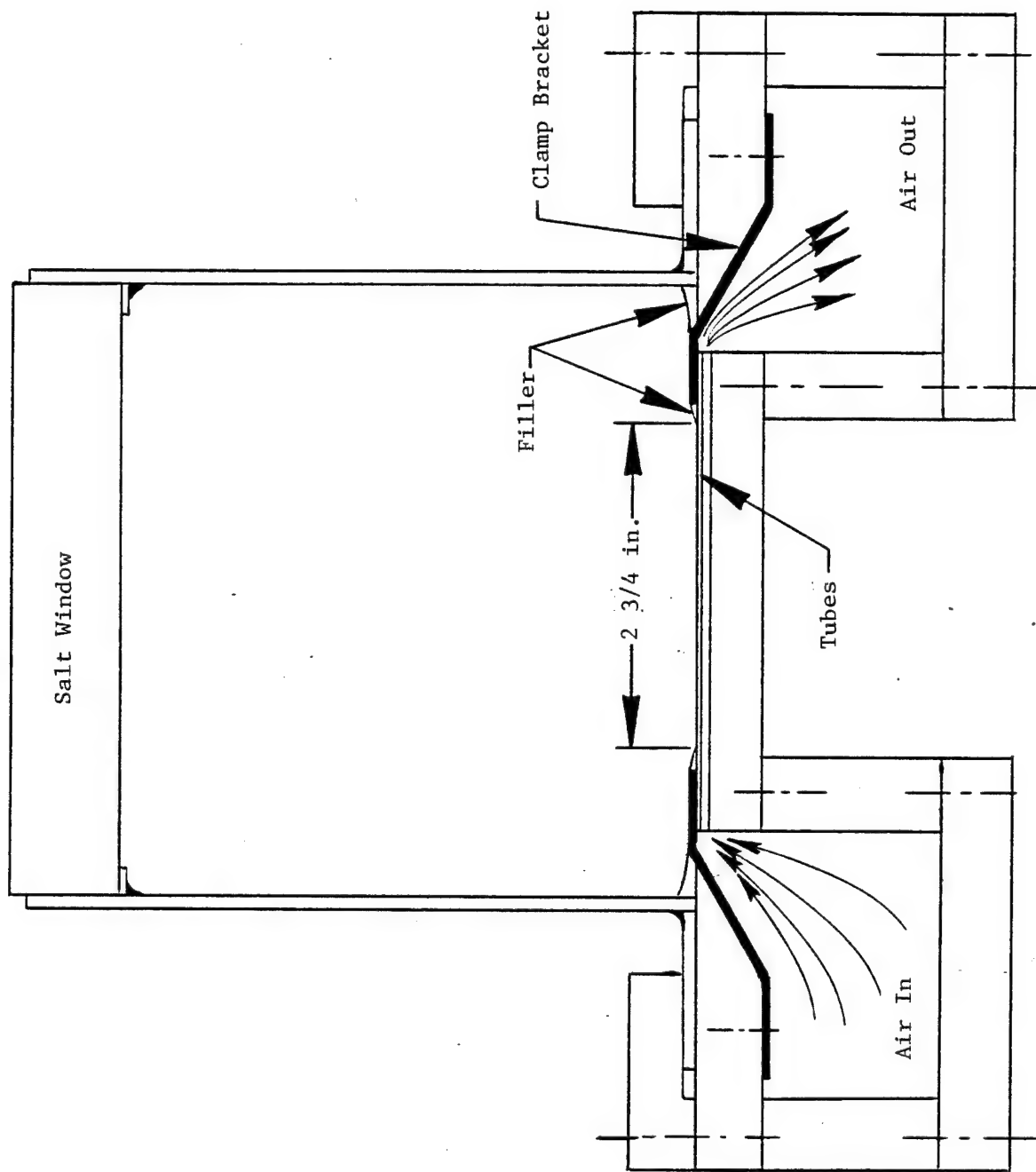


Figure 32. Wind Tunnel Test Section with
Captubes at Crossflow

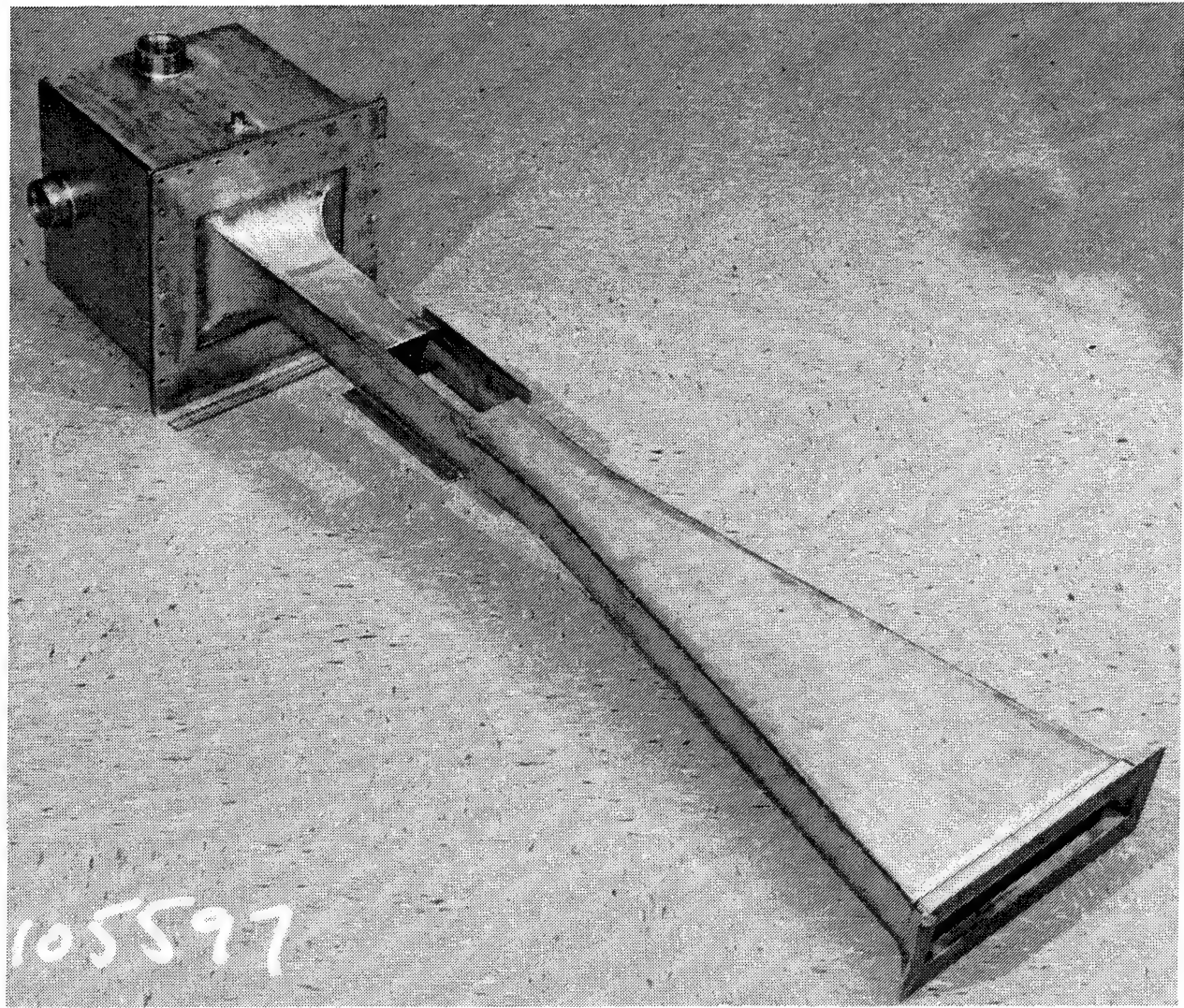


Figure 33. Wind Tunnel Test Rig Assembly

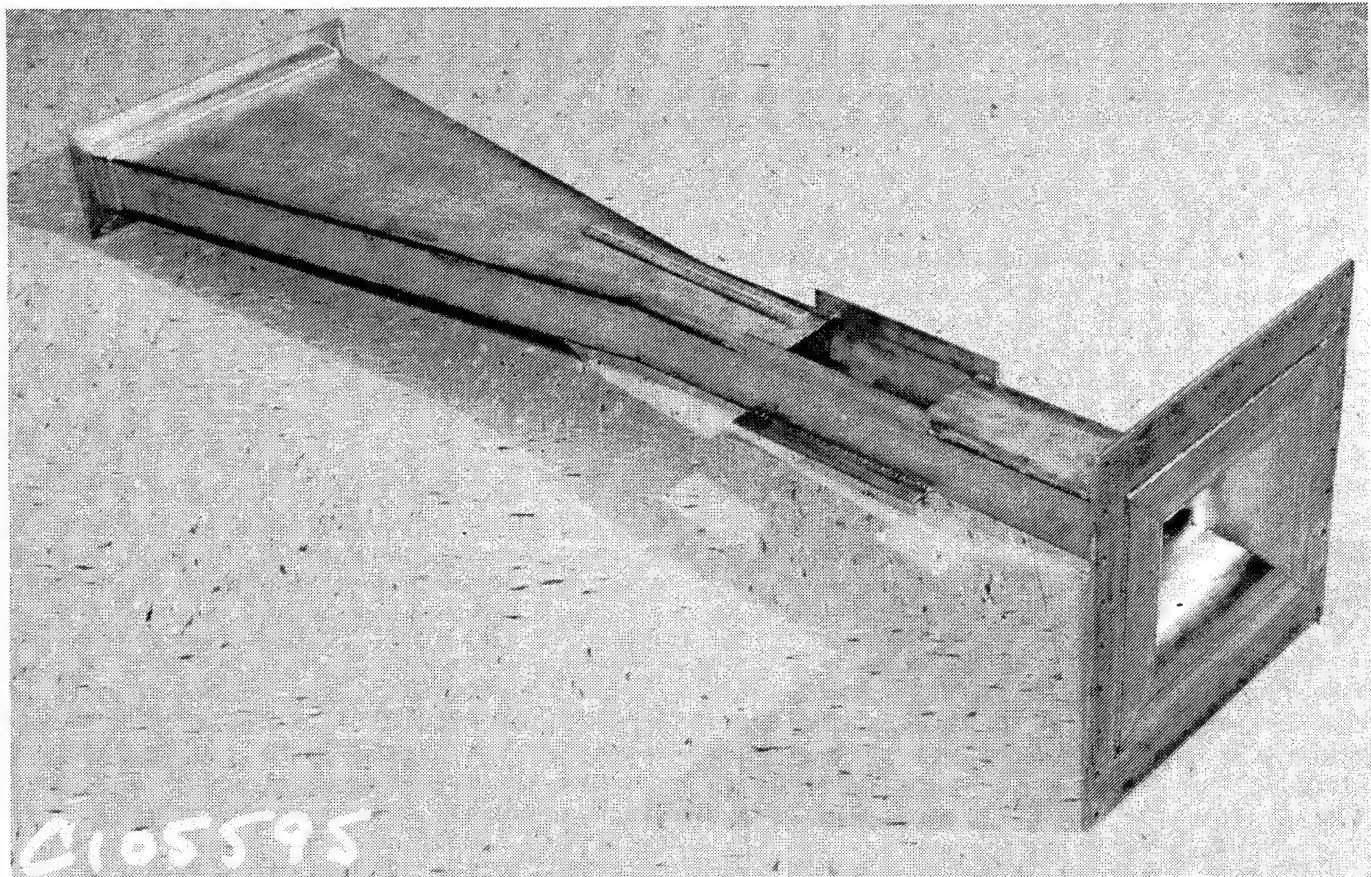


Figure 34. Wind Tunnel Test Rig Horn.

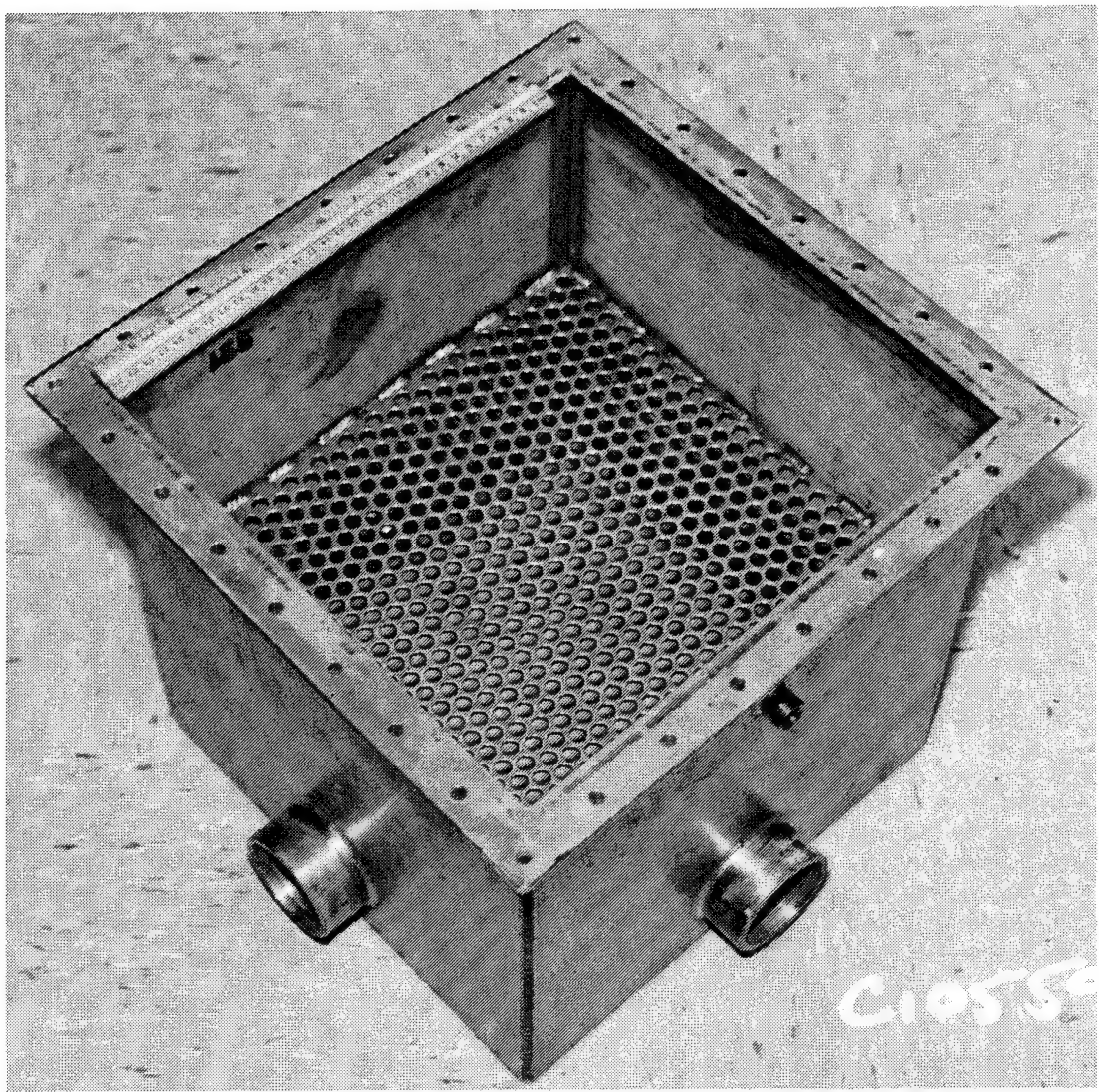


Figure 35. Wind Tunnel Test Rig Plenum Chamber.

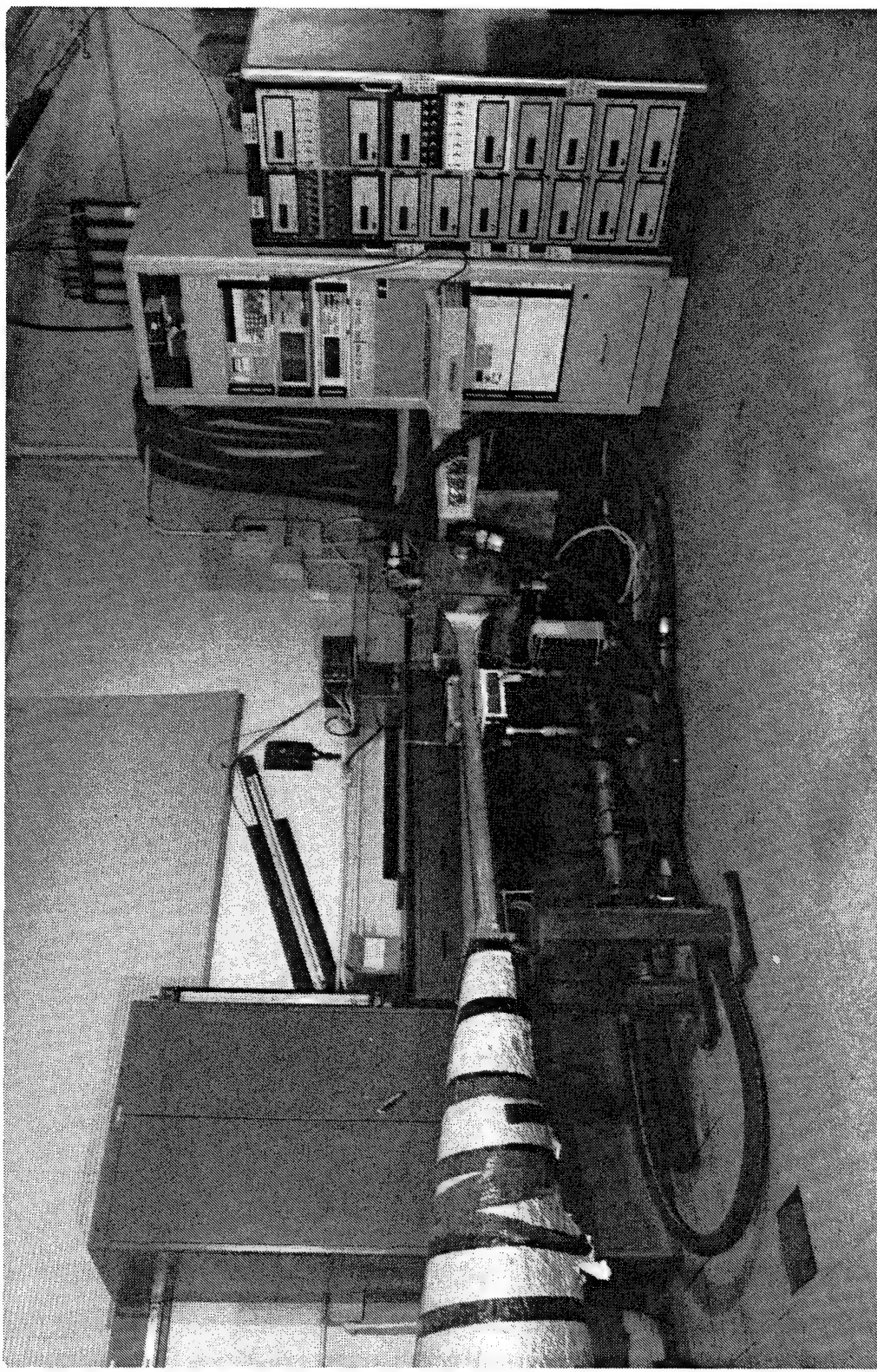


Figure 36.

Wind Tunnel Test Rig

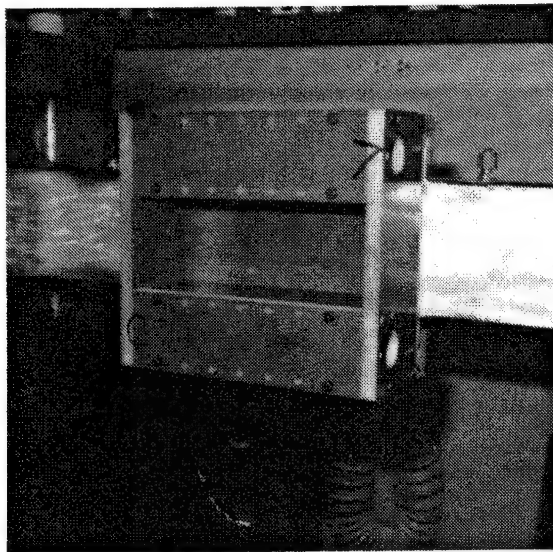


Figure 37. Test Panel Plenum,
Bottom View.

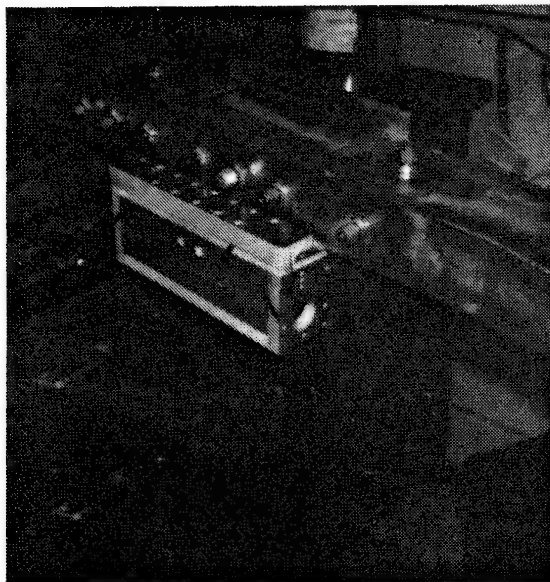


Figure 38. Test Panel Plenum,
Side View.

edge. During testing, air temperature in the tubes got as high as 185°F with pressure at about 80 psia. Since 185°F was not high enough to cause permanent thermal degradation of any of the materials in the capillary tube test panel, it is assumed that the 80 psia must have induced some stretching or micro-cracking to cover the observed residual warp which remained after the panel was released from its clamped assembly at room temperature. Since the panel had been rigidly restrained on all four sides, any expansion from temperature or pressure would manifest in an upward bulge at the center. However, if temperature was the main contributor to expansion, the bulge should have retracted at cool down, but it remained. Accordingly, it is suspected that pressure induced stretching and/or micro-cracks may be a contributing factor. At any rate, the panel was reassembled to the test section by bonding it clamped flat in place using 630 RTV adhesive leaving clearance on all four sides for expansion. Testing was resumed and no further bulging occurred at the original 185°F and 80 psia as before. Figure 39 shows the wind tunnel test rig arranged for this program.

5.2 Test Data Analysis

The SIMCAP computer program was used to simulate the conditions existing in the composite wall/capillary tube flow check No. 2 dated 4-23-85, listed in Table I. Predicted results for total mass flowrate, Mach number and Reynolds number at tube exit are plotted versus source pressure in Figures 40 through 42. Test data for mass flowrate are also plotted in Figure 40. Conclusions based on these results are:

1. Predicted and measured mass flowrates agree within 1%. This is a remarkable agreement considering the number of parameters and the large ranges of Mach and Reynolds numbers involved in this test.
2. Figure 41 shows that the flow was choked for source pressure greater than about 51 psia. Therefore, the three data points at the highest source pressure were at choked flow conditions.
3. Figure 42 shows that the Reynolds numbers for all of the test runs were in the turbulent range (2300).

5.3 Heat Transfer Analysis

An air flow check or measurement was conducted on a total of 94 parallel capillary tubes with inside diameter of 0.0126 inch and length of 10 inches using air at 75°F . The 94 tubes were potted air tight through a slotted panel that formed on one side of a manifold as shown in Figure 43. Air fed into the manifold was

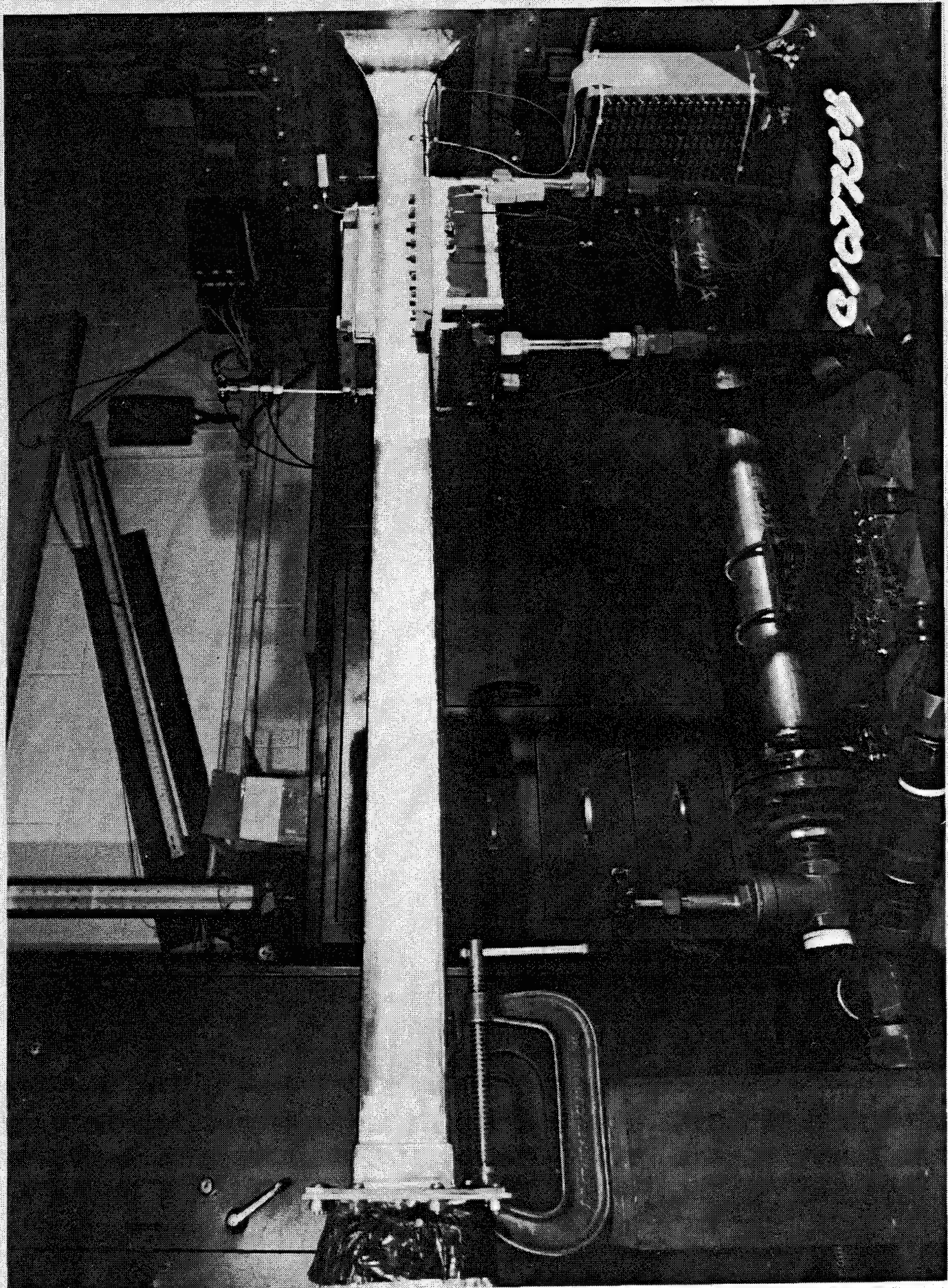


Figure 39 Wind Tunnel Test Set-Up For Check Out

Table I.

*** FLOW CHECK DATA SHEET ***

10:12:47 04-23-1985

PART DESCRIPTION IS: .02DIA. ID CAPILLARY PANEL W/T TEST

PURPOSE OF FLOW CHECK IS: DETERMINE FLOW CHARACTERISTICS

TECHNICIAN; JIM CAHILL EXT. 3-9302

BAROMETRIC PRESSURE IS 29.37 IN HG./ 14.42067 PSIA

IDENT NO.	STEP NO.	PLEN PRESS IN.HG	* W * (ACTUAL) LB/SEC	PRESS RATIO	FLOW FUNC	PLEN PSIA	AIR TEMP DEG.	ROTO PRESS IN.HG	ROTO SCALE RDG.
2.0*	1.0*	8.81*	0.010239*	1.300*	0.01263*	18.8*	75.0*	101.0*	0.004680
2.0*	2.0*	14.66*	0.013790*	1.499*	0.01476*	21.6*	76.0*	101.0*	0.006300
2.0*	3.0*	20.56*	0.017182*	1.700*	0.01622*	24.5*	76.0*	101.0*	0.007850
2.0*	4.0*	26.43*	0.020451*	1.900*	0.01727*	27.4*	76.0*	101.0*	0.009350
2.0*	5.0*	29.37*	0.021868*	2.000*	0.01754*	28.9*	76.0*	101.0*	0.010000
2.0*	6.0*	32.30*	0.023265*	2.100*	0.01778*	30.3*	76.0*	101.0*	0.010650
2.0*	7.0*	38.18*	0.026165*	2.300*	0.01825*	33.2*	76.0*	101.0*	0.012000
2.0*	8.0*	44.05*	0.029145*	2.500*	0.01872*	36.1*	77.0*	101.0*	0.013400
2.0*	9.0*	49.93*	0.031659*	2.700*	0.01883*	39.0*	77.0*	100.5*	0.014600
2.0*	10.0*	55.80*	0.034497*	2.900*	0.01911*	41.8*	77.0*	100.5*	0.016000
2.0*	11.0*	58.74*	0.035653*	3.000*	0.01910*	43.3*	78.0*	100.5*	0.016600
2.0*	12.0*	61.67*	0.037038*	3.100*	0.01921*	44.7*	78.0*	100.5*	0.017300
2.0*	13.0*	67.55*	0.039733*	3.300*	0.01936*	47.6*	78.0*	100.0*	0.018700
2.0*	14.0*	73.43*	0.042696*	3.500*	0.01961*	50.5*	78.0*	100.0*	0.020200
2.0*	15.0*	79.30*	0.045500*	3.700*	0.01977*	53.4*	78.0*	100.0*	0.021300
2.0*	16.0*	85.17*	0.047864*	3.900*	0.01975*	56.3*	79.0*	100.0*	0.022500
2.0*	17.0*	88.11*	0.049268*	4.000*	0.01982*	57.7*	79.0*	100.0*	0.023200

ADIABATIC FLOW CHECK #2
204 TUBES ; ID=0.0209 INCH ; L=3 INCHES ; TSOURCE=77.F

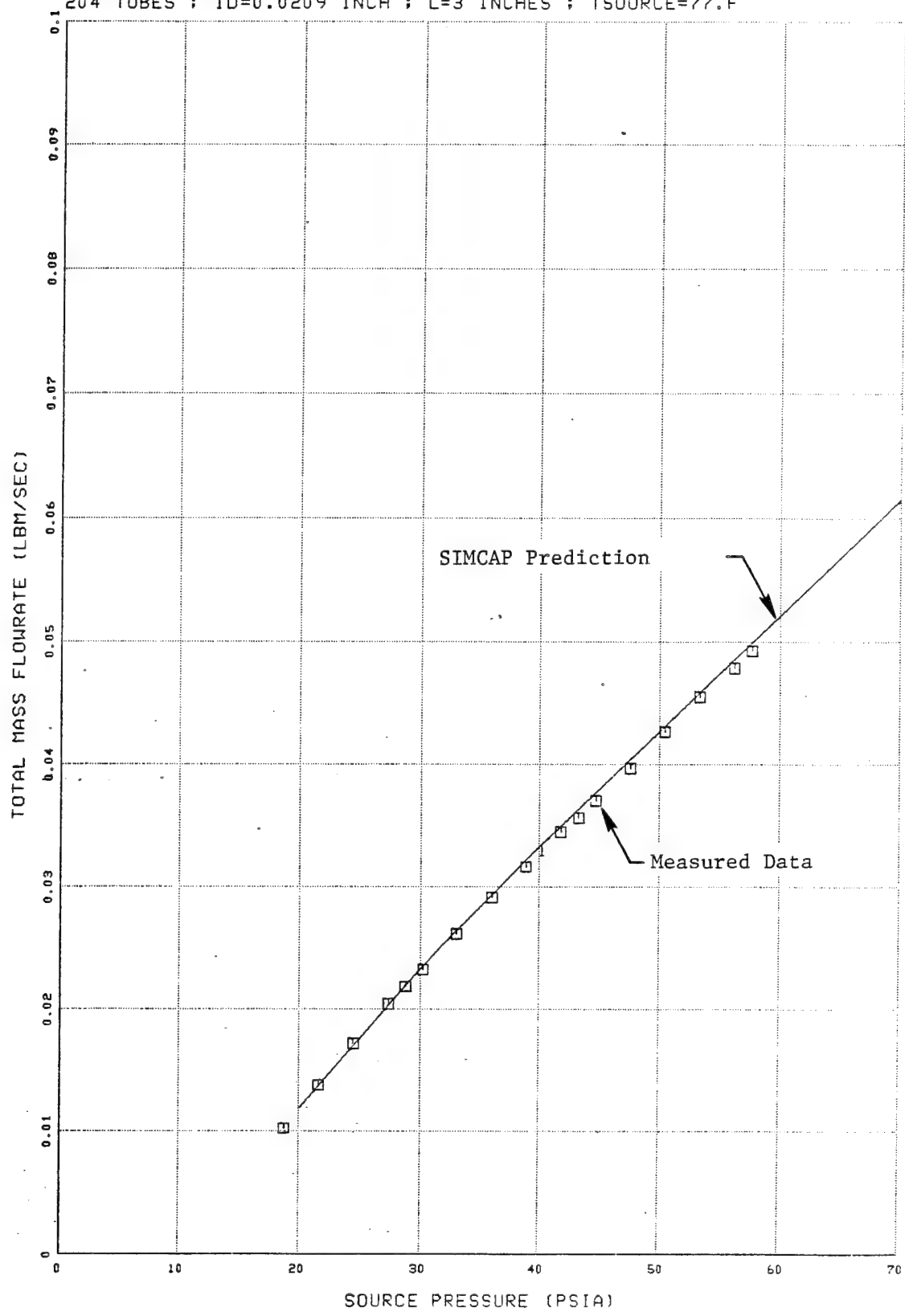


Figure 40.

ADIABATIC FLOW CHECK #2
ID=0.0209 INCH ; L=3 INCHES ; TSOURCE=77.F

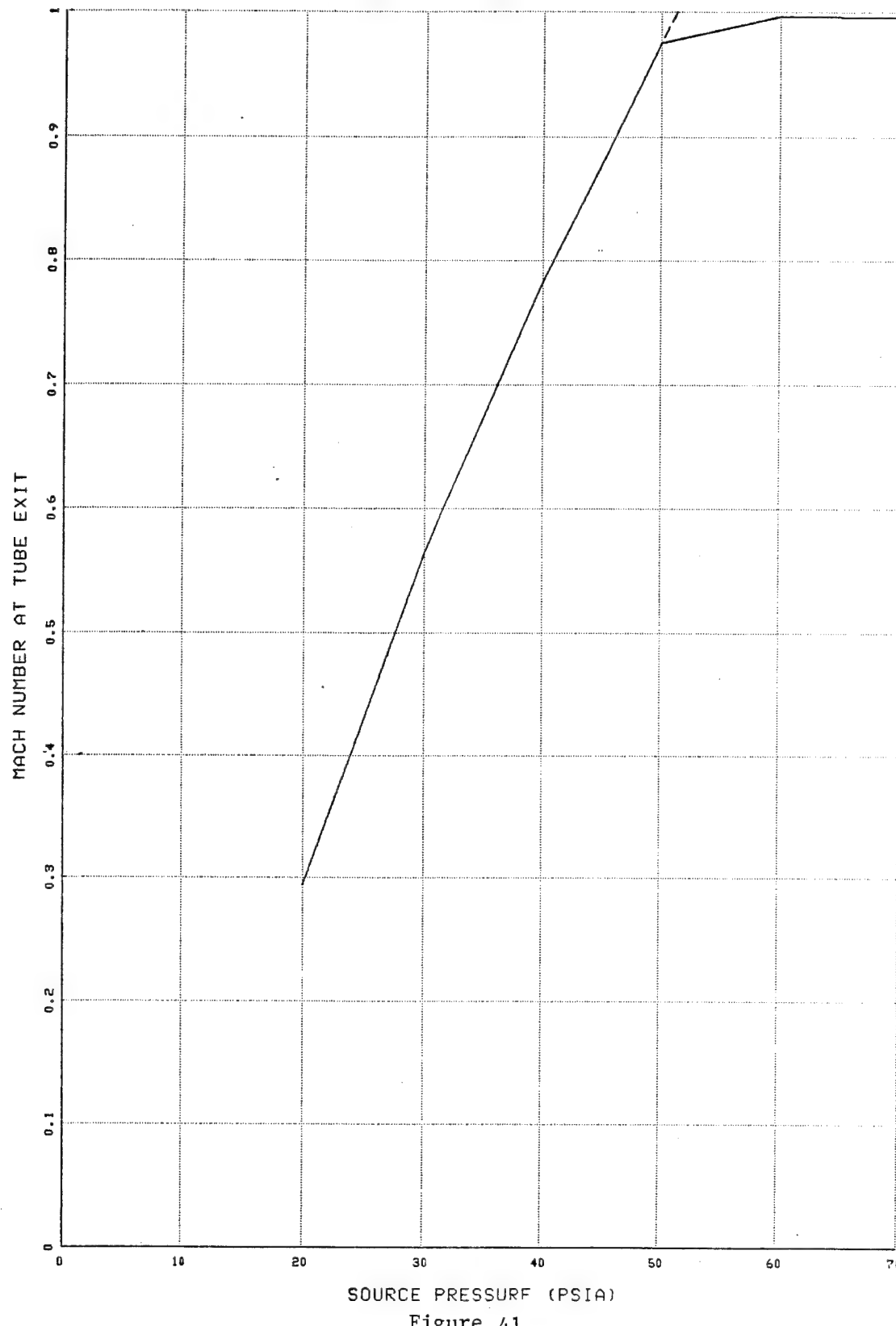


Figure 41.

ADIABATIC FLOW CHECK #2
ID=0.0209 INCH ; L=3 INCHES ; TSOURCE=77.F

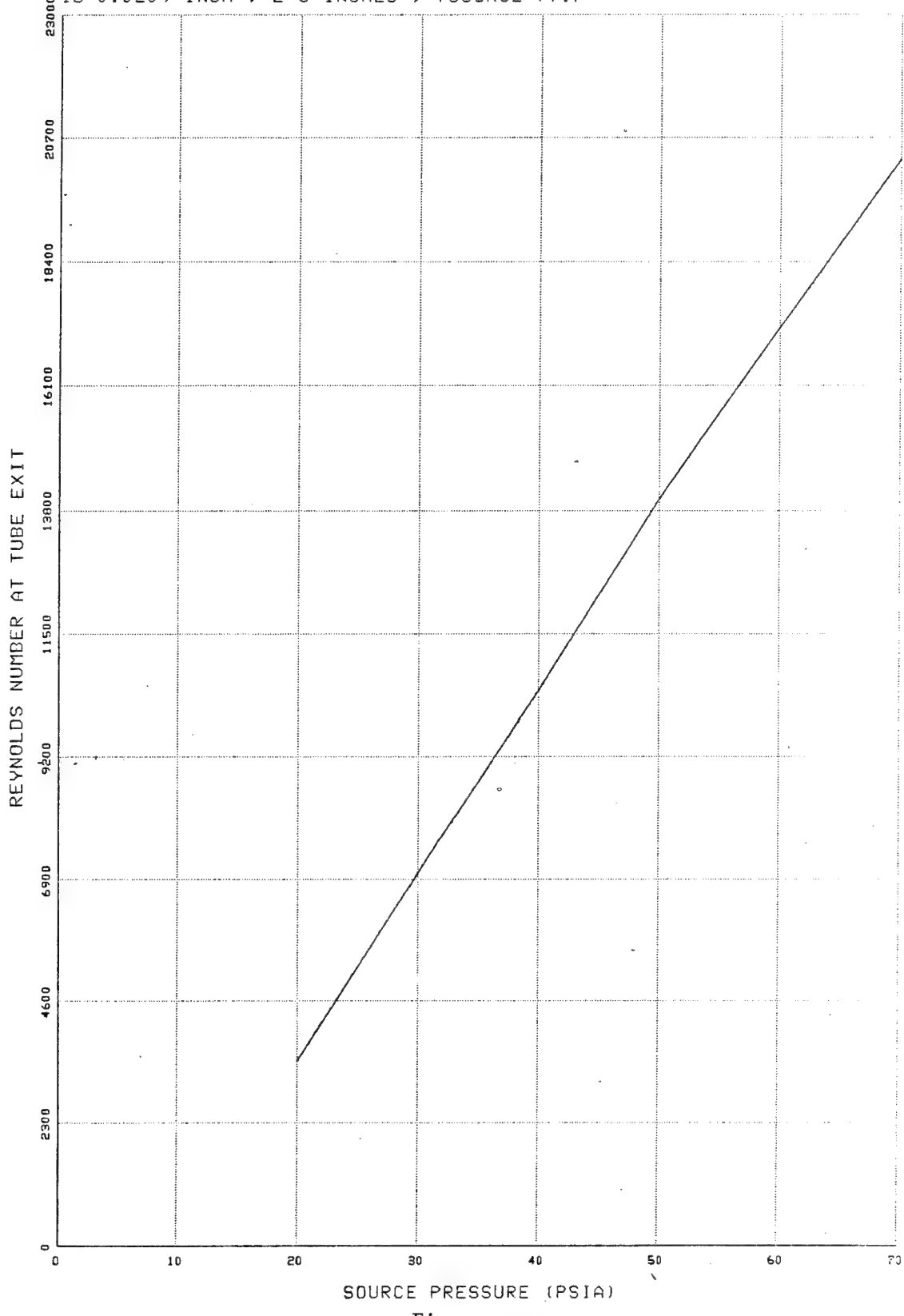


Figure 42.

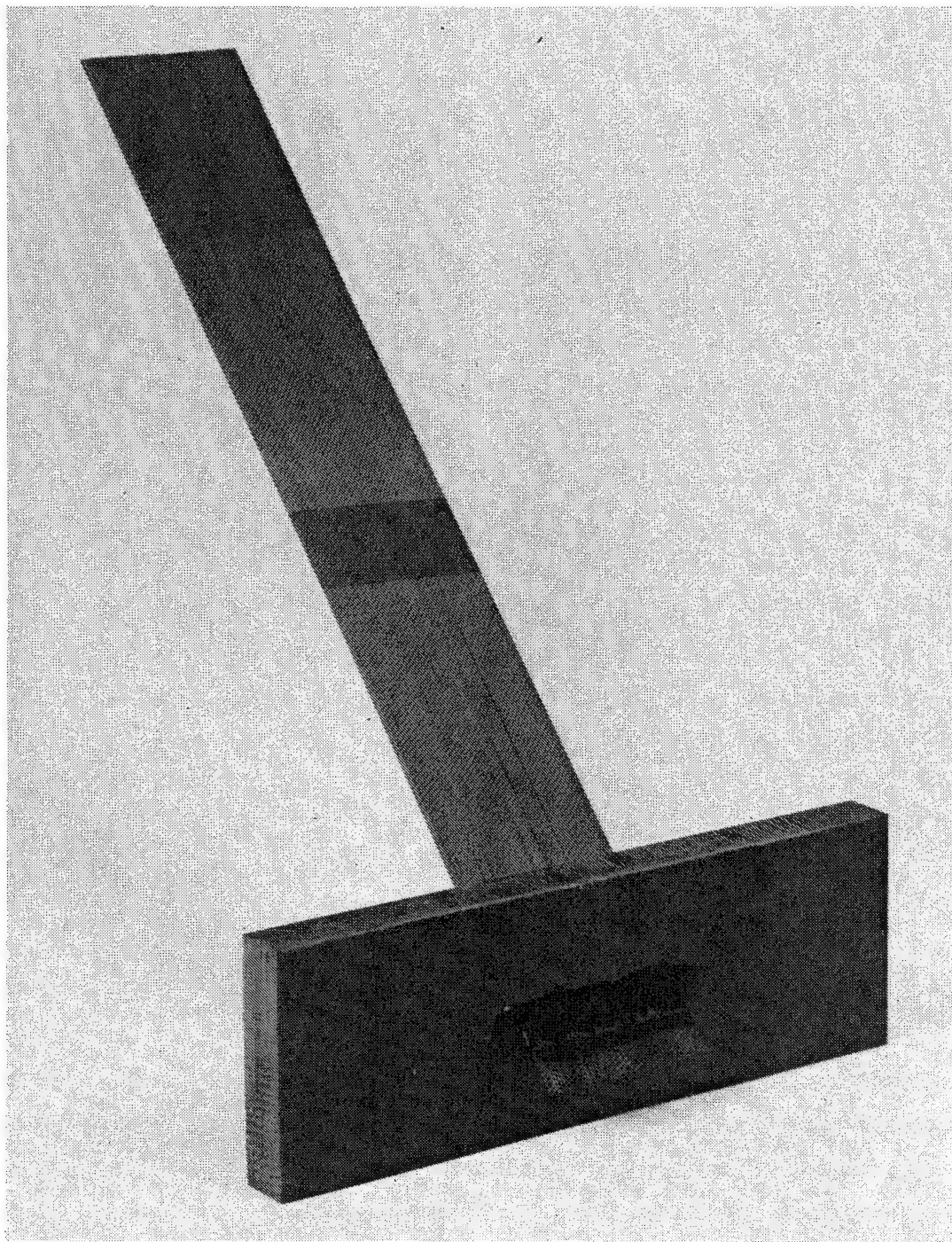


Figure 43.

measured for flow rate and pressure. The only escape for the air was through the 94 tubes. Results of this flow check are tabulated in Figures 44, Table 2 & 3 and Figure 45. The SIMCAP computer program was then used to simulate the conditions established in Table 2. Predicted results for mass flowrate, Reynolds number at tube exit, and Mach number at tube exit are plotted versus source pressure in Figures 46 through 48. Test data for mass flowrate are also plotted in Figure 46.

Conclusions based on these results are as follows:

1. Transition from laminar to turbulent flow begins to occur at a source pressure of about 30 psia, there the Reynolds number at the tube exit is about 2300.
2. There is a very good agreement between predicted and measured mass flowrates, even within the transition range.
3. Figure 47 shows that the largest Mach number achieved in these tests was about 0.45 at a source pressure of about 50 psia. In order to achieve choked flow conditions, the source pressure would have to be increased above 105 psia.
4. If the relatively small source pressure level used in the flow check is also used in the heat transfer tests, then small flowrates and very large temperature drops will be produced.

In the text that follows there are twenty-four figures containing predictions for heat transfer tests projected for four different assemblies of captubes. Two samples have an external heat transfer surface which is six inches wide by three inches long, and two samples are three inches wide by six inches long. One sample of each size contains the larger diameter tubes (0.0209-inch inside diameter) and one sample of each size contains the smaller diameter tubes (0.0126-inch diameter).

The captube simulation code (SIMCAP) was used to calculate results plotted in Figures 49 through 65. In addition, the KEPS boundary layer code was used to simulate the fluid flow in the cold air duct to which the samples would be exposed. Boundary layer results for the duct wall and the sample external surface are plotted in Figures 66 through 72.

***** FLOW CHECK DATA SHEET *****

FROM THE LABORATORIES OF THE DEVELOPMENT HEAT TRANSFER UNIT
W. K. SOUTH MANAGER

ITEM	DESCRIPTION
FLOW METER:	COX SERIES 12 ROTOMETER CALIBRATED AT 50 PSIG.
PRESSES:	HEISE GAUGES , IN.HG 'MENSOR' DIGITAL PRESS. GA. IN.HG \ H2O
TEMPERATURE:	DORIC TYPE 400A
BAROMETRIC PRESSURE:	HEISE GAUGE , ABSOLUTE PRESSURE
DATA:	MANUALLY ENTERED INTO I.B.M. P-C
ALL HARDWARE AND PROCEDURES CONFORM TO 'AEBG 'SPECIFICATION ** E50TF218 ** UNLESS OTHERWISE NOTED.	
DEFINITIONS:	
IDENT NO.:	A NUMBER ON THE PART THAT IS UNIQUE
STEP NO.:	THE ORDER OF PROGRESSION OF A PRE-DETERMINED PROCEDURE
PLEN PRESS: IN.HG	THE WALL STATIC PRESSURE IN THE SUPPLY PLENUM
* W * (ACTUAL)	THE CORRECTED TRUE MASS FLOW IN LBM / SECOND
PRESS RATIO:	THE RATIO OF PLEN PRESS TO P. BARO $FR = (P. BARO + P. PLEN) / P. BARO$
FLOW FUNC:	A CALCULATED VALUE, DOESN'T INCLUDE AREA $W_{ACTUAL} * (AIR TEMP + 460)^{.5} / P. PLEN PSIA$
PLEN PRESS: PSIA	A CALCULATED VALUE, $(P. PLEN + P. BARO) * (14.699/29.92)$
AIR TEMP:	THE TEMPERATURE OF THE AIR SUPPLY
ROTO PRESS:	THE INTERNAL PRESSURE OF THE ROTOMETER
ROTO SCALE: RDG.	THE NUMERICAL VALUE READ FROM THE SCALES ON THE ROTOMETER TUBES

Figure 44.

*** FLOW CHECK DATA SHEET ***

15:35:12

03-11-1985

PART DESCRIPTION IS: (94) CAPILLARY TUBES W/RAGGED ENDS

PURPOSE OF FLOW CHECK IS: DETERMINE FLOW CHARACTERISTICS

TECHNICIAN; JIM CAHILL EX. 3-9302

BAROMETRIC PRESSURE IS 29.045 IN HG./ 14.2611 PSIA

IDENT NO.	STEP NO.	PLEN PRESS IN.HG	* W * (ACTUAL) LB/SEC	PRESS RATIO	FLOW FUNC	PLEN PRESS PSIA	AIR TEMP	ROTO PRESS DEG. IN.HG	ROTO SCALE RDG.
1.0*	1.0*	8.70*	0.000424*	1.300*	0.00053*	18.5*	75.0*	103.0*	0.000187
1.0*	2.0*	14.50*	0.000738*	1.499*	0.00080*	21.4*	75.0*	103.0*	0.000345
1.0*	3.0*	20.30*	0.001100*	1.699*	0.00105*	24.2*	74.0*	103.0*	0.000525
1.0*	4.0*	26.10*	0.001446*	1.899*	0.00123*	27.1*	74.0*	103.0*	0.000650
1.0*	5.0*	29.00*	0.001611*	1.998*	0.00131*	28.5*	74.0*	103.0*	0.000730
1.0*	6.0*	32.00*	0.001797*	2.102*	0.00138*	30.0*	74.0*	103.0*	0.000820
1.0*	7.0*	37.70*	0.002150*	2.298*	0.00152*	32.8*	75.0*	103.0*	0.000990
1.0*	8.0*	43.50*	0.002339*	2.498*	0.00152*	35.6*	75.0*	103.0*	0.001080
1.0*	9.0*	49.40*	0.002444*	2.701*	0.00147*	38.5*	75.0*	103.0*	0.001130
1.0*	10.0*	55.20*	0.002570*	2.900*	0.00144*	41.4*	75.0*	103.0*	0.001190
1.0*	11.0*	58.00*	0.002633*	2.997*	0.00142*	42.8*	75.0*	103.0*	0.001220
1.0*	12.0*	63.00*	0.002800*	3.169*	0.00143*	45.2*	75.0*	103.0*	0.001300
1.0*	13.0*	68.00*	0.002948*	3.341*	0.00143*	47.7*	75.0*	103.0*	0.001370
1.0*	14.0*	73.00*	0.003065*	3.513*	0.00141*	50.1*	75.0*	103.0*	0.001425

Table II

CAPILLARY TUBES W/RAGGED ENDS FLOW CHECK

PLEN PRES	W ACTUAL	PRESSURE RATIO	FLOW FUNC
8.7	0.000424	1.3	0.00053
14.5	0.000738	1.499	0.0008
20.3	0.0011	1.699	0.00105
26.1	0.001446	1.899	0.00123
29	0.001611	1.998	0.00131
32	0.001797	2.102	0.00138
37.7	0.00215	2.298	0.00152
43.5	0.002339	2.498	0.00152
49.4	0.002444	2.701	0.00147
55.2	0.00257	2.9	0.00144
58	0.002633	2.997	0.00142
63	0.0028	3.169	0.00143
68	0.002948	3.341	0.00143
73	0.003065	3.513	0.00141

Table III

F/F VS PRESSURE RATIO
CAPILLARY TUBES

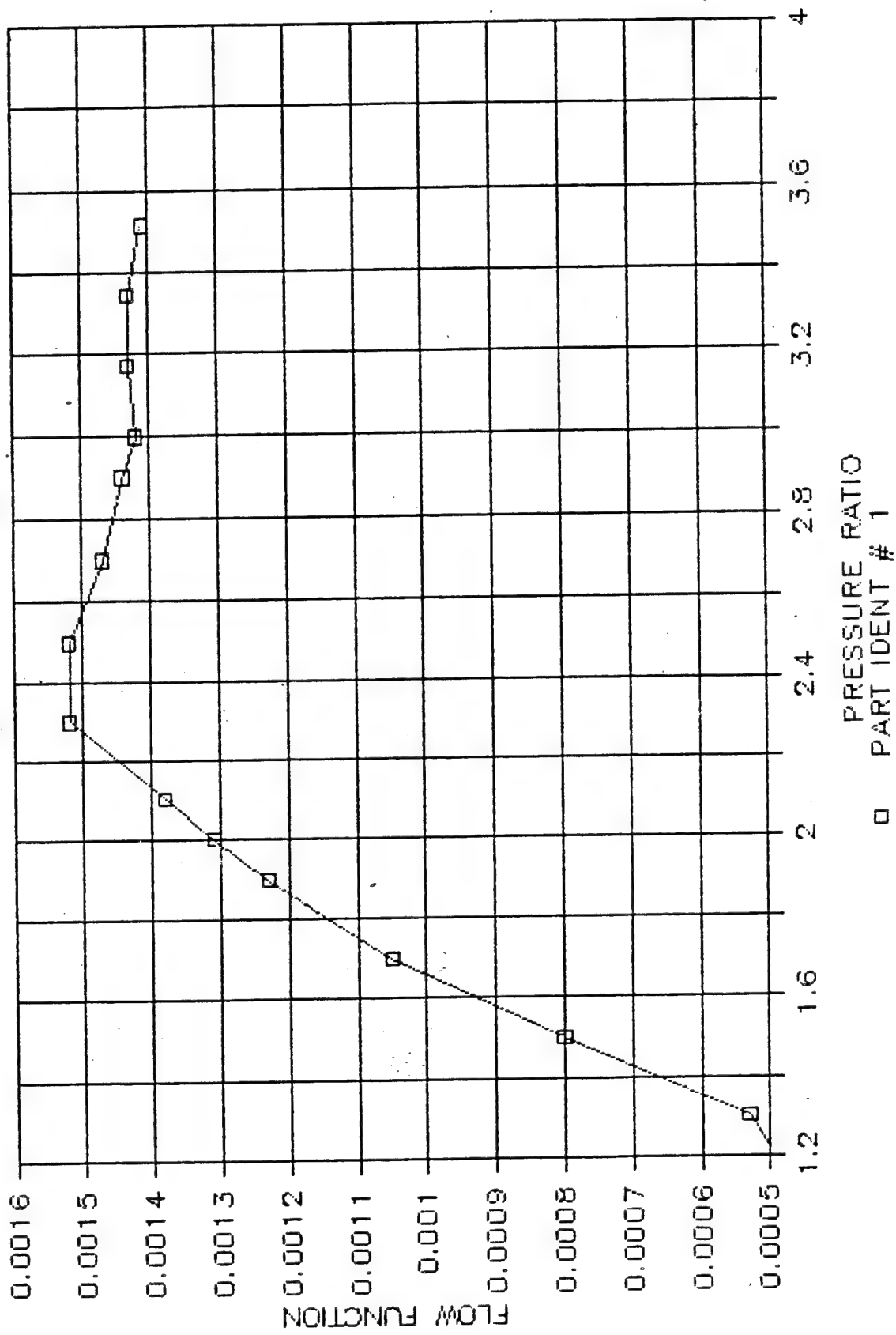


Figure 45.

ADIABATIC FLOW CHECK OF SMALLER TUBING (94 PARALLEL TUBES)
ID=0.0126 INCH ; L=10 INCHES ; TSOURCE=75.F

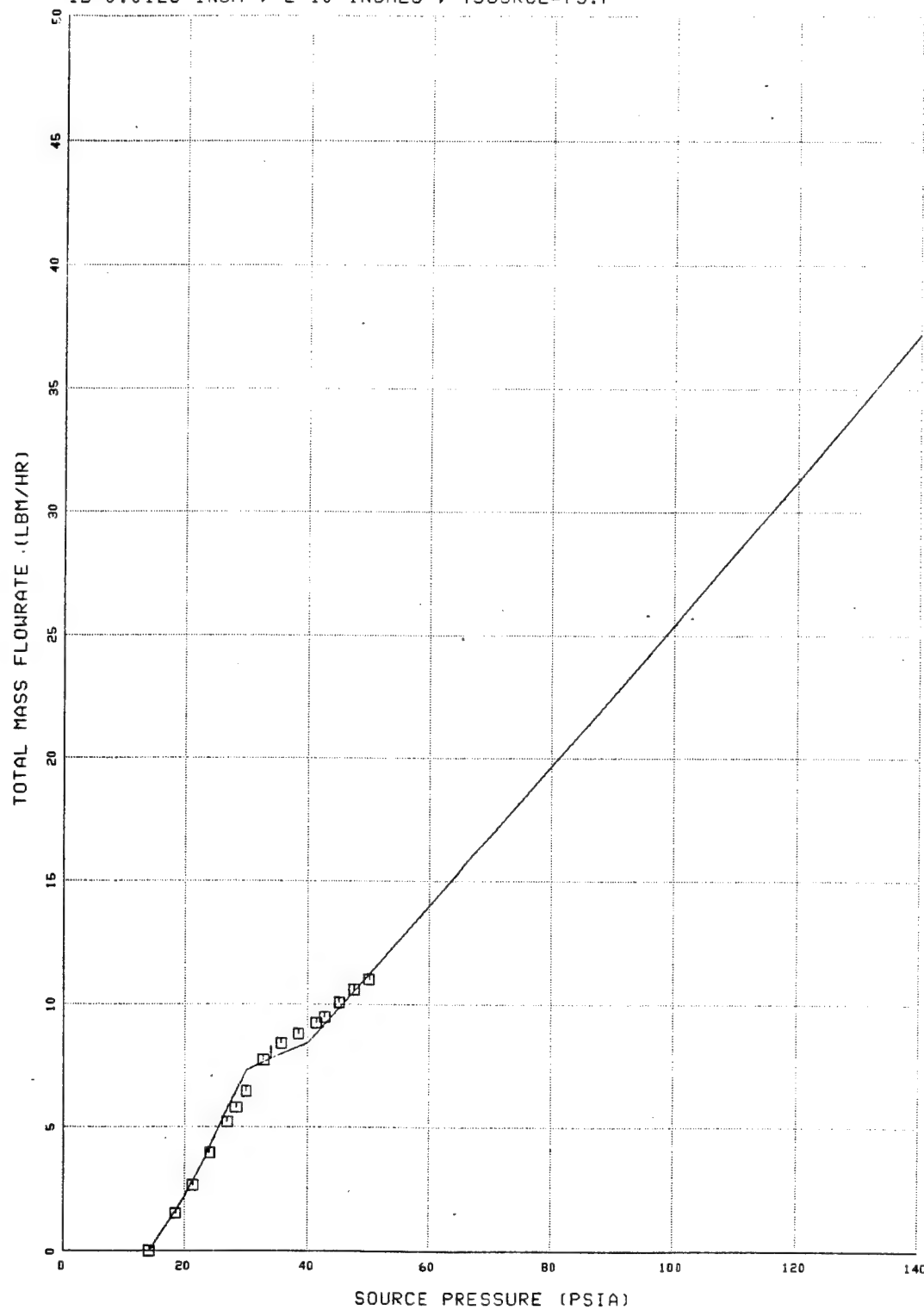


Figure 46

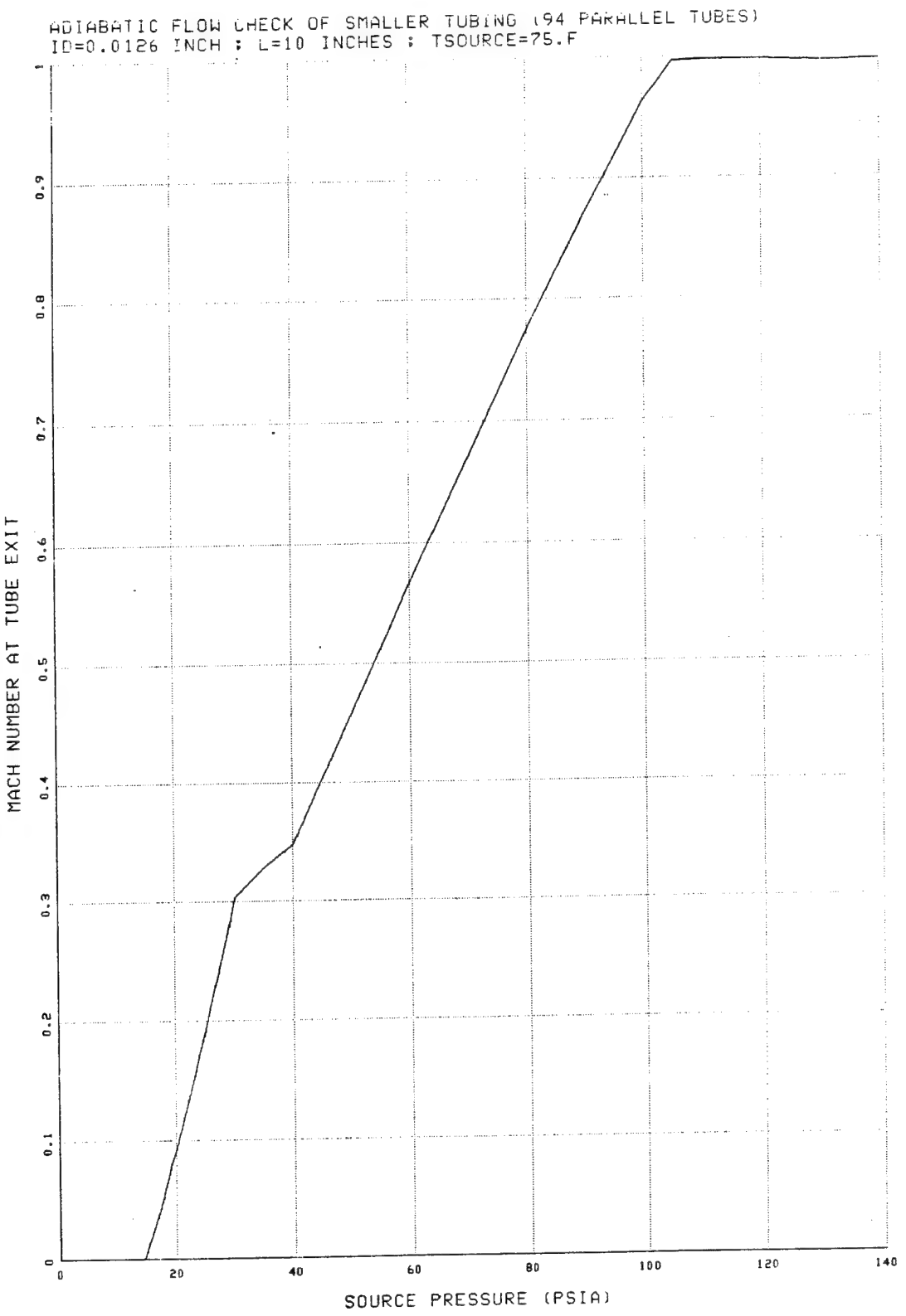


FIGURE 47

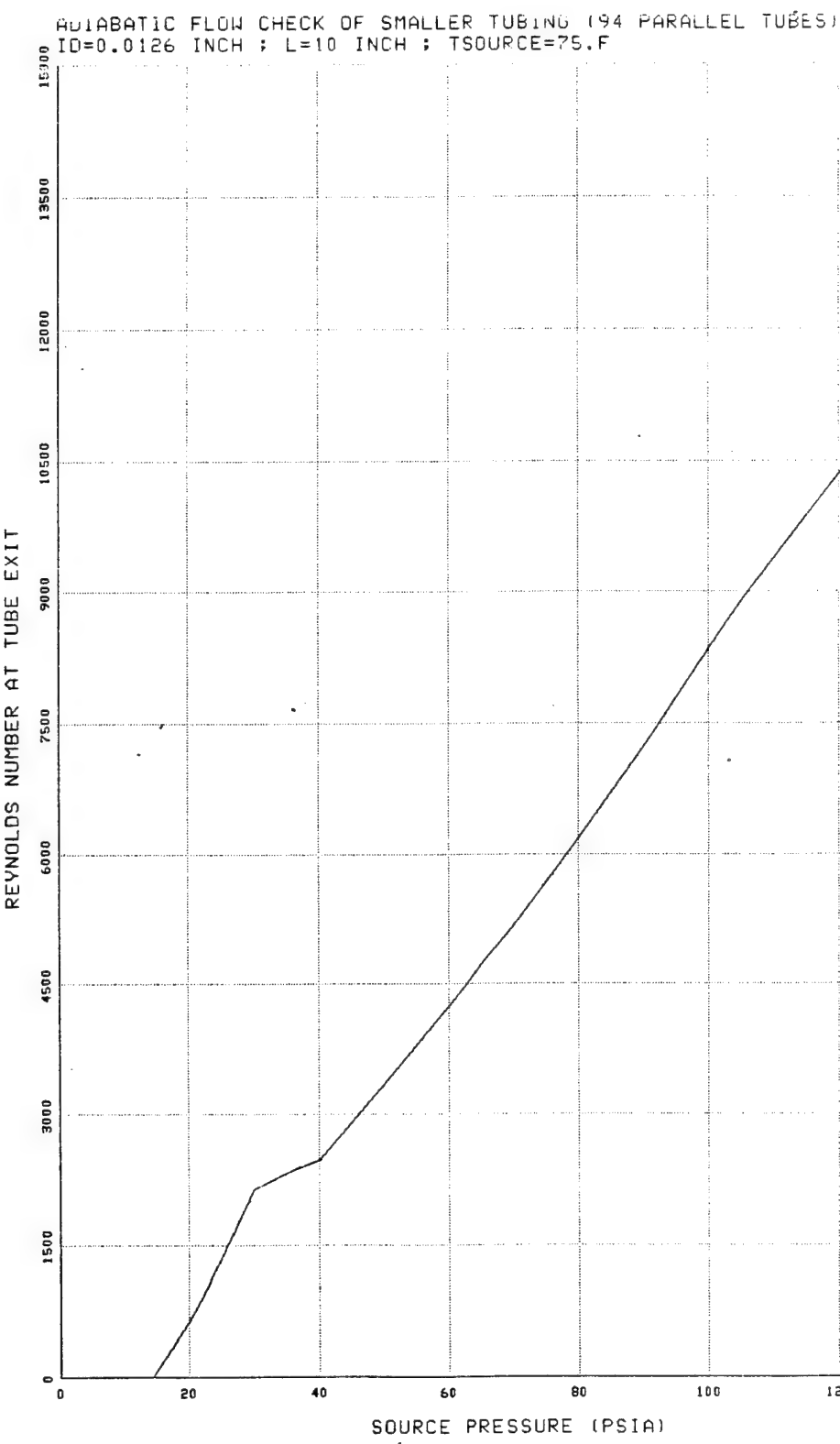


Figure 48

PRETEST PREDICTION FOR 6-IN. WIDE CAPTUBE HEAT TRANSFER TEST
204 TUBES : TSINK=70.F : TSOURCE=95, 120, 170, 250.F

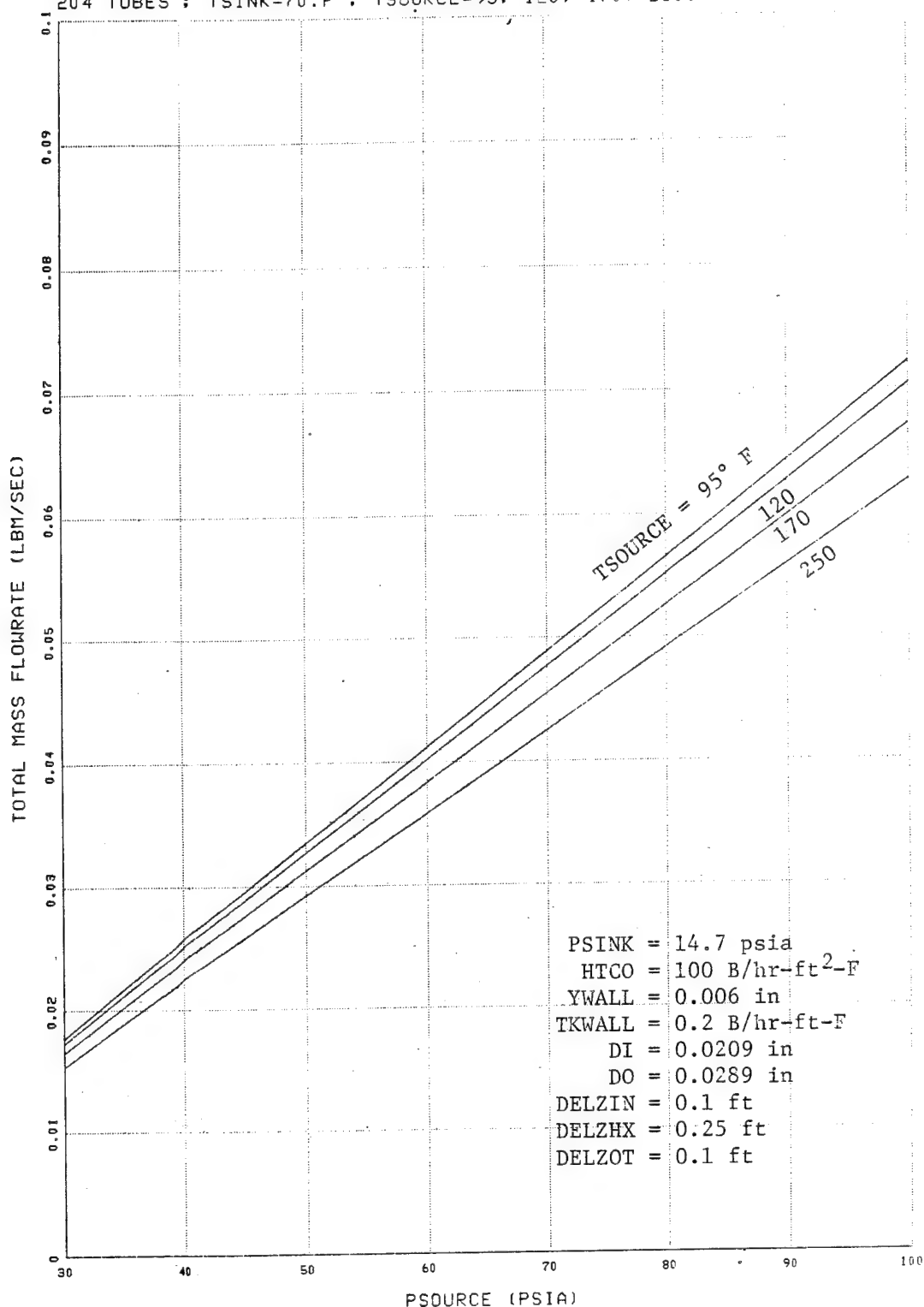


Figure 49

PRETEST PREDICTION FOR 6-IN. WIDE CAPTUBE HEAT TRANSFER TEST
TSINK=70.F ; TSOURCE=95, 120, 170, 250.F

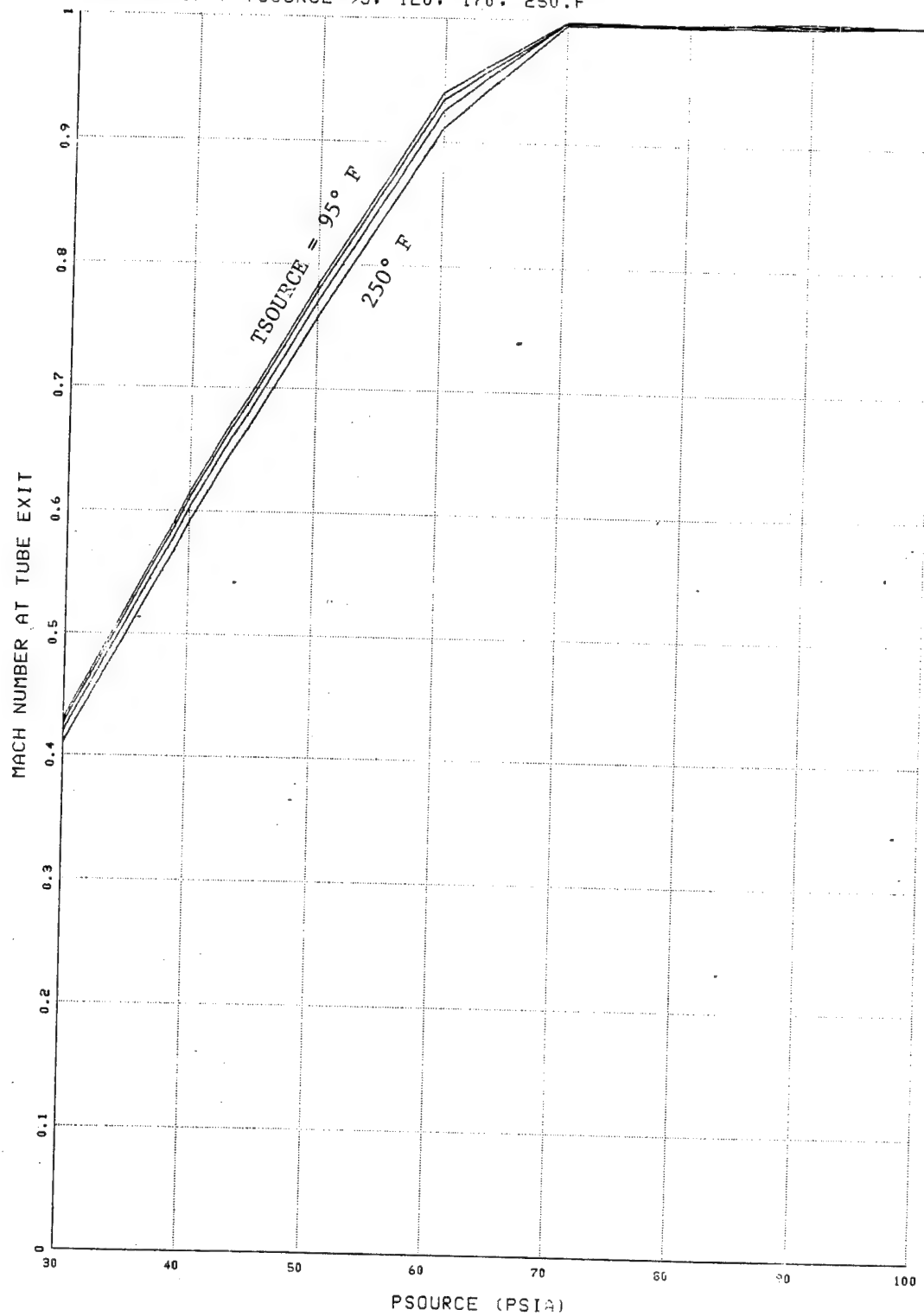


Figure 50

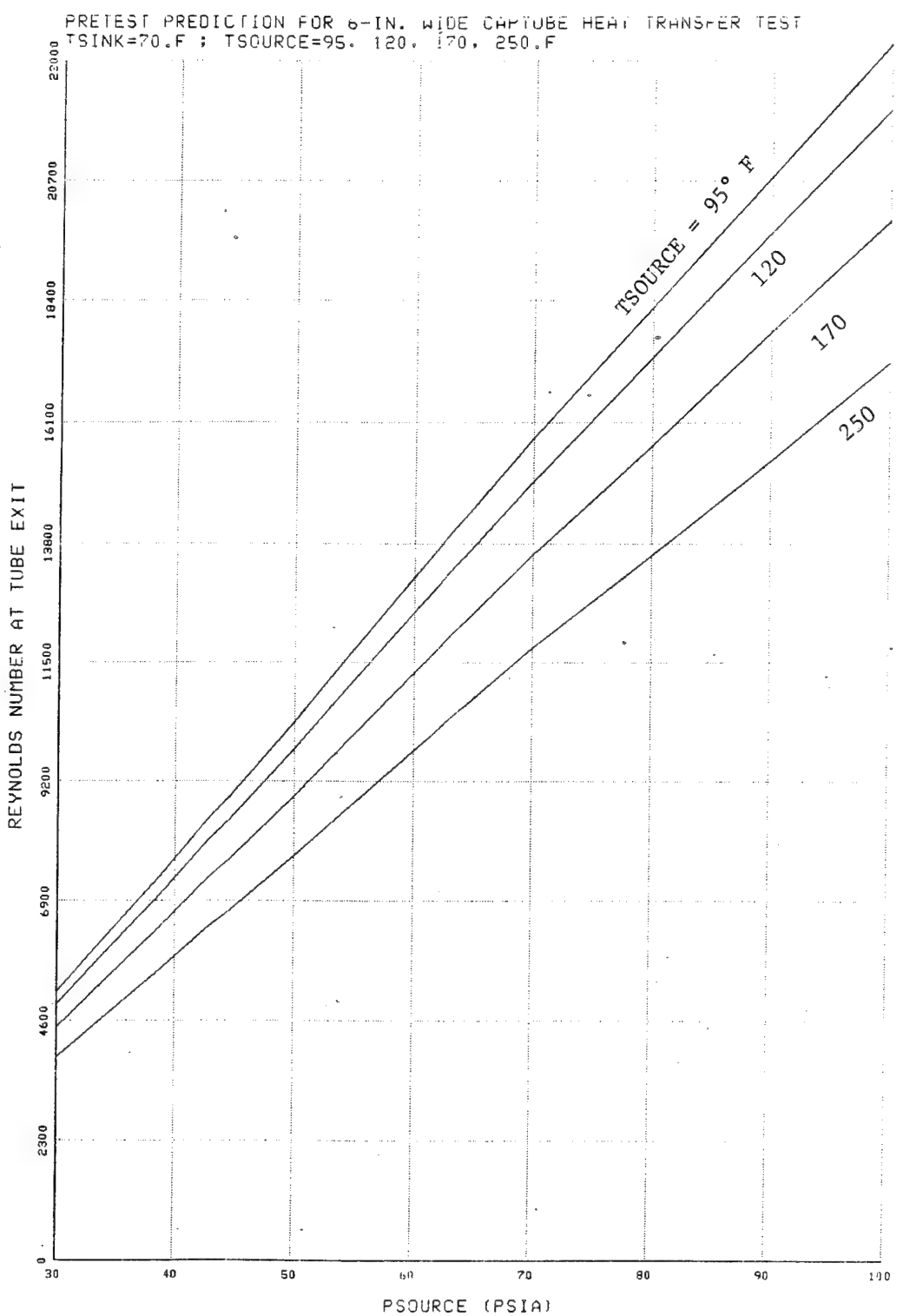


Figure 51

PRETEST PREDICTION FOR 6-IN. WIDE CAPTIVE HEAT TRANSFER TEST
EFFECT OF PSOURCE WITH TSOURCE=95.F & TSINK=70.F

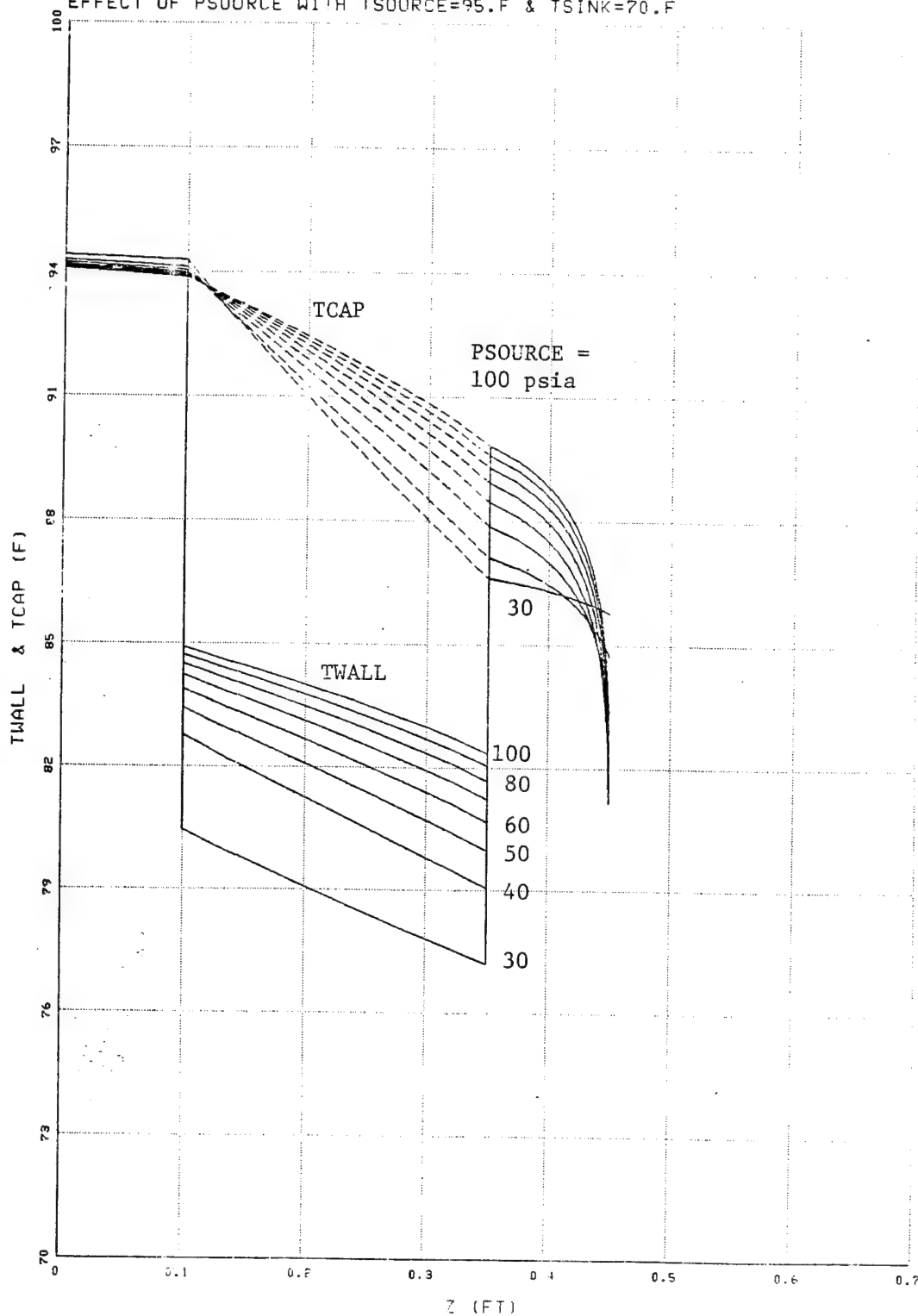


Figure 52

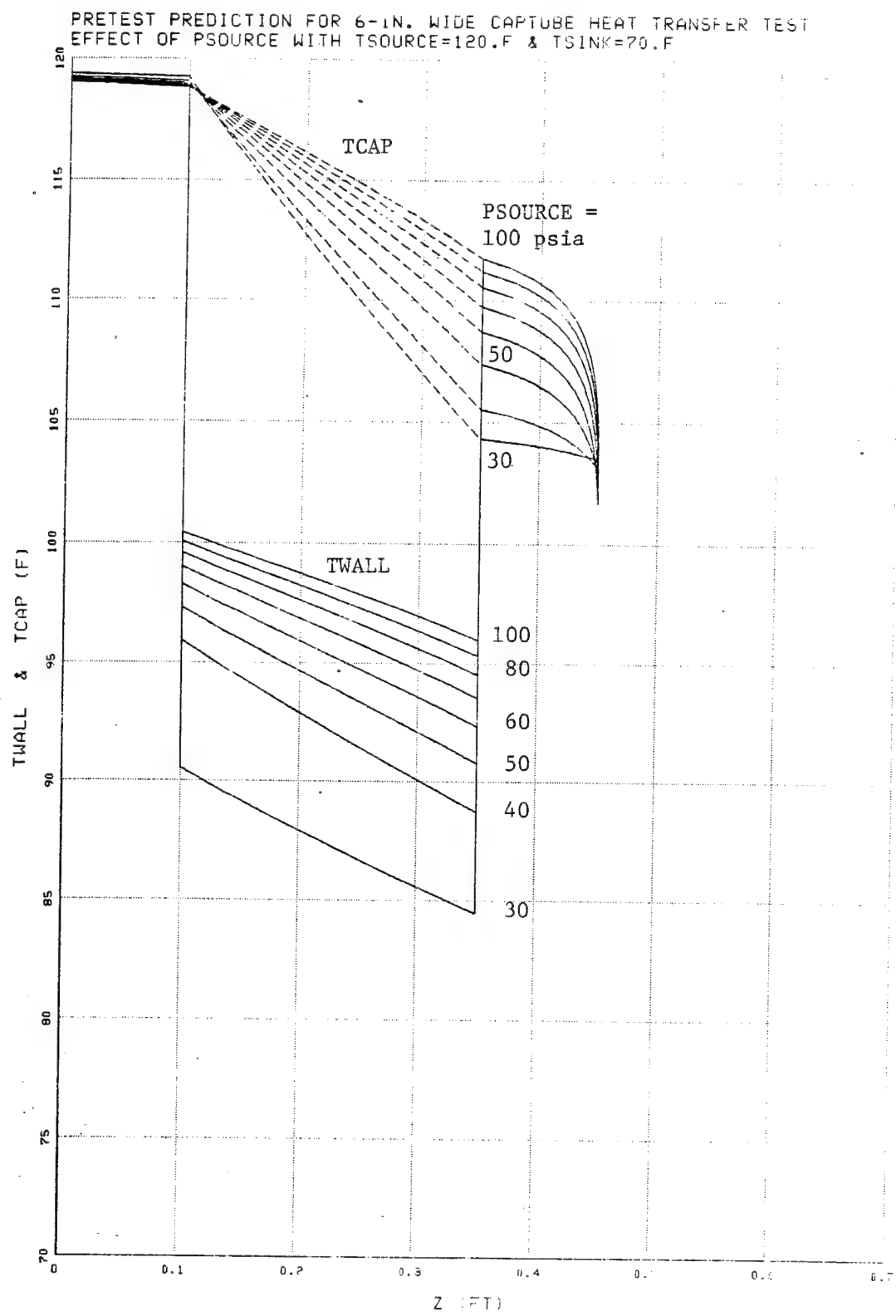


Figure 53

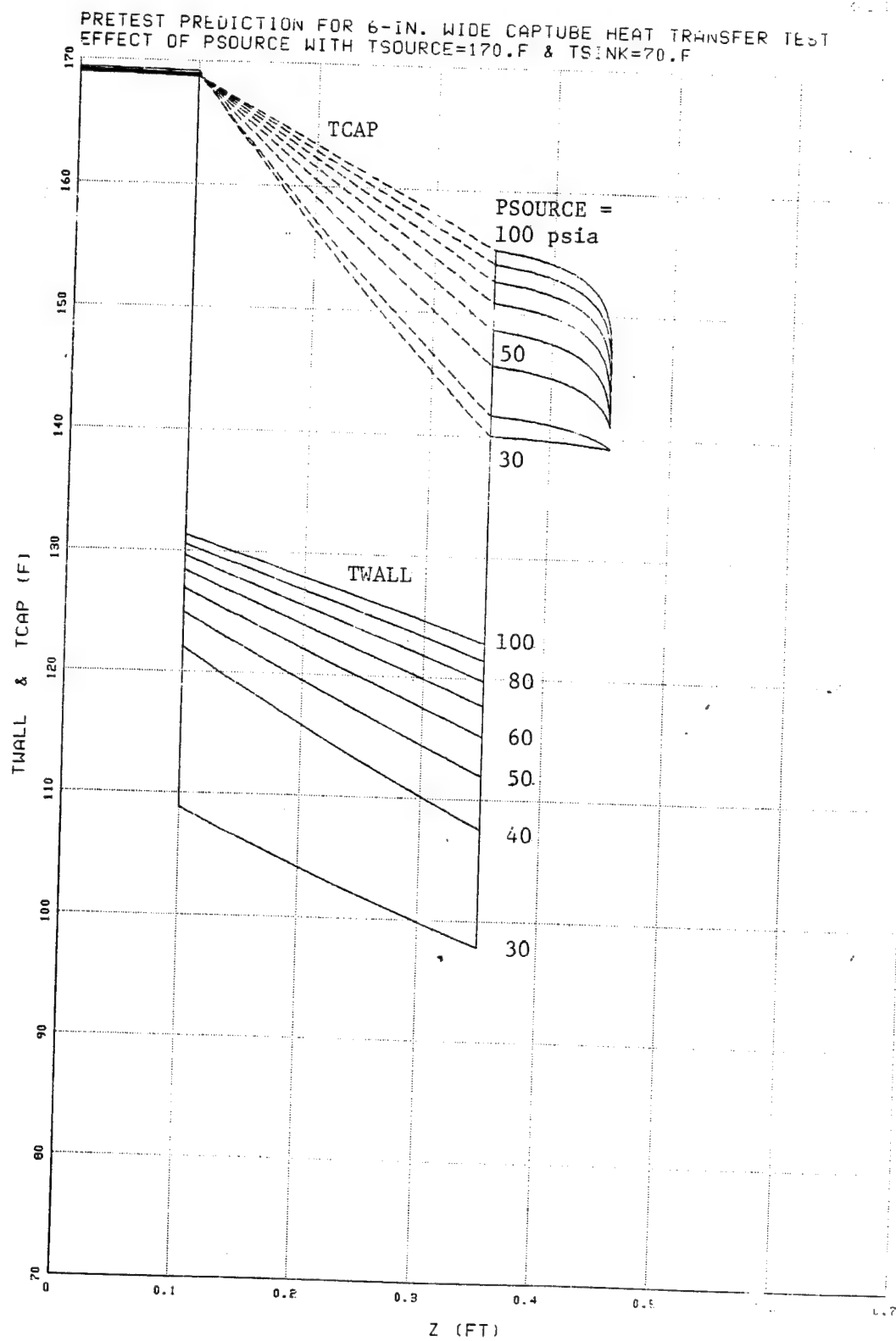


Figure 54

PRETEST PREDICTION FOR 6-IN. WIDE CAPTIVE HEAT TRANSFER TEST
EFFECT OF PSOURCE WITH TSOURCE=250.F & TSINK=70.F

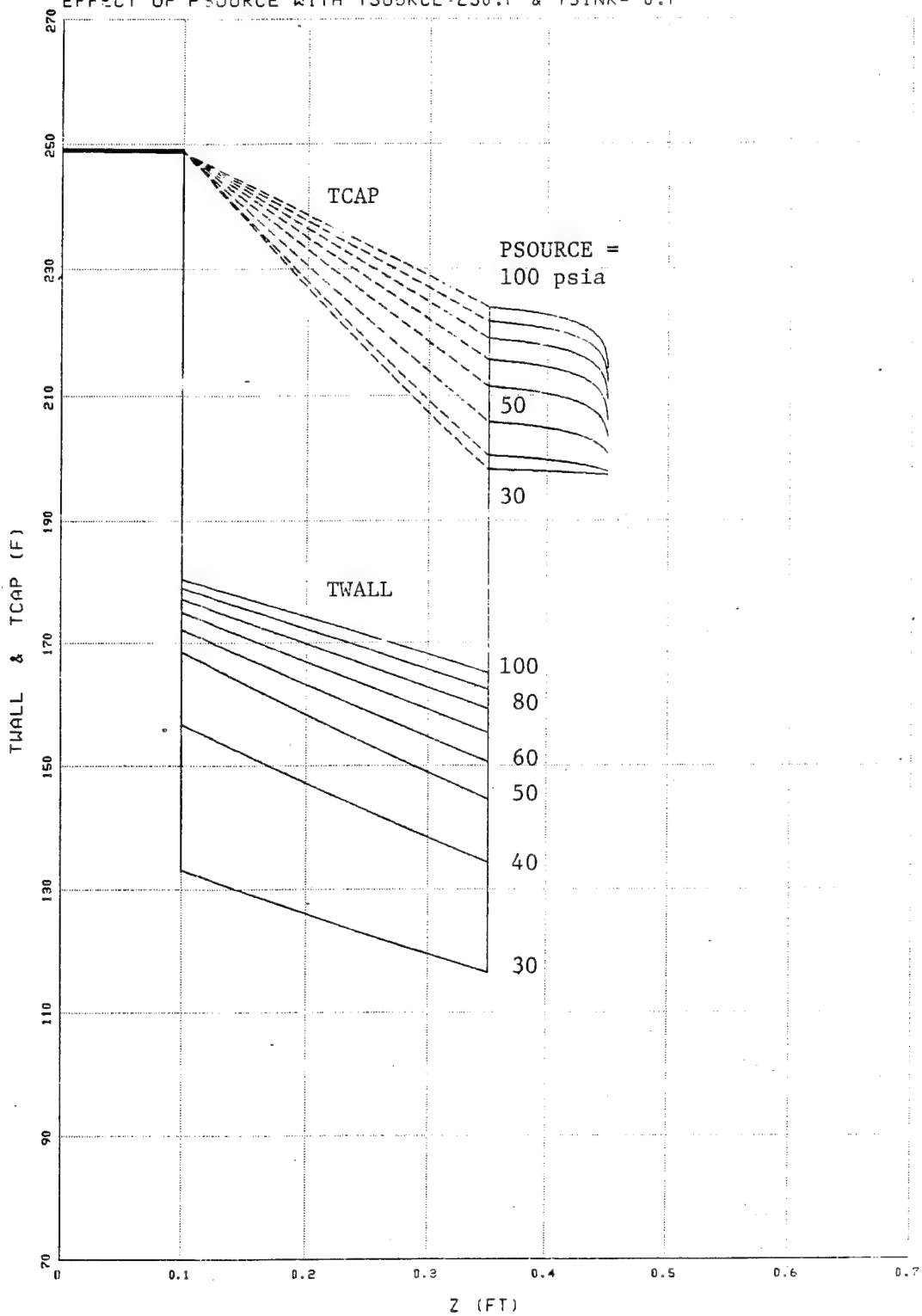


Figure 55

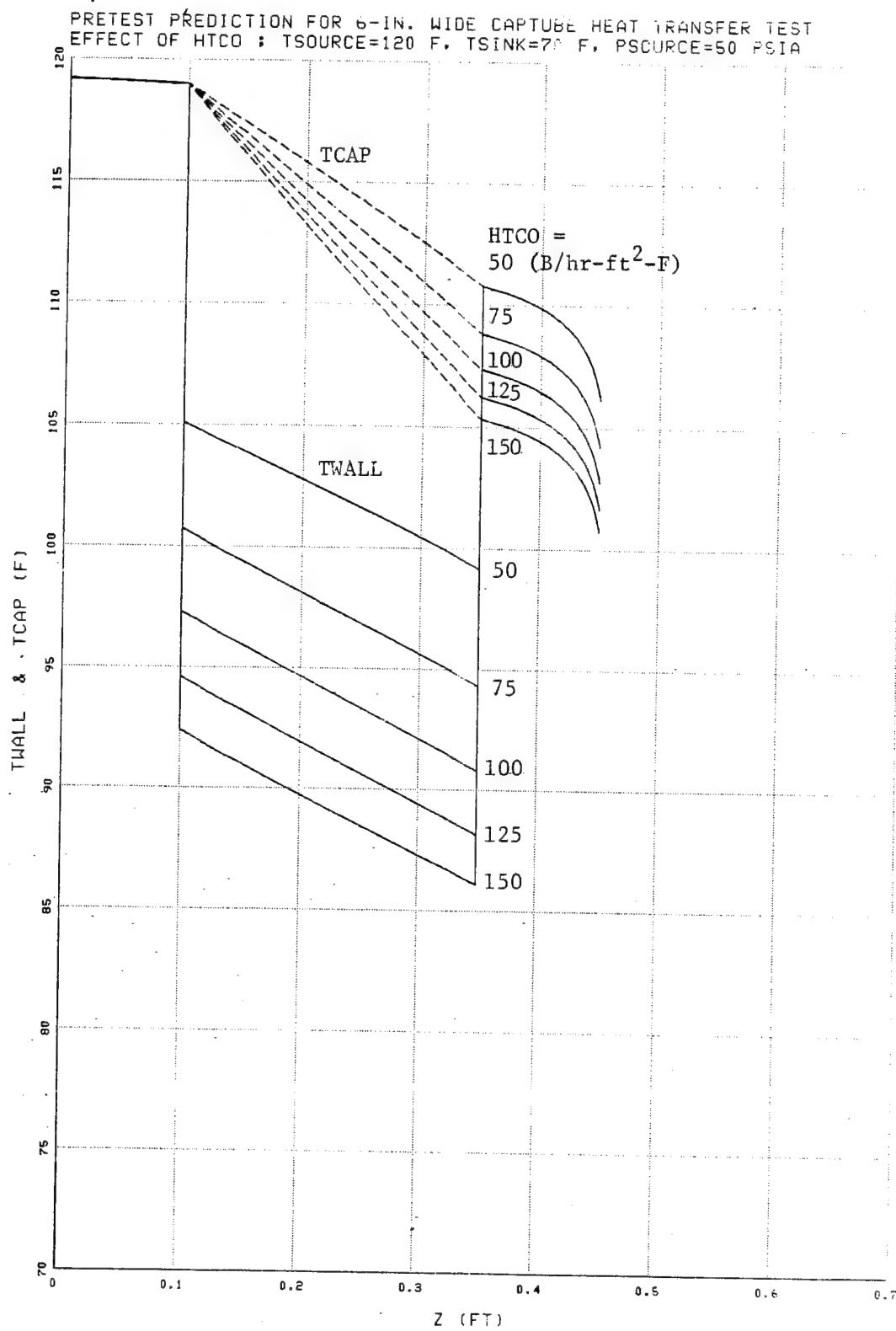


Figure 56

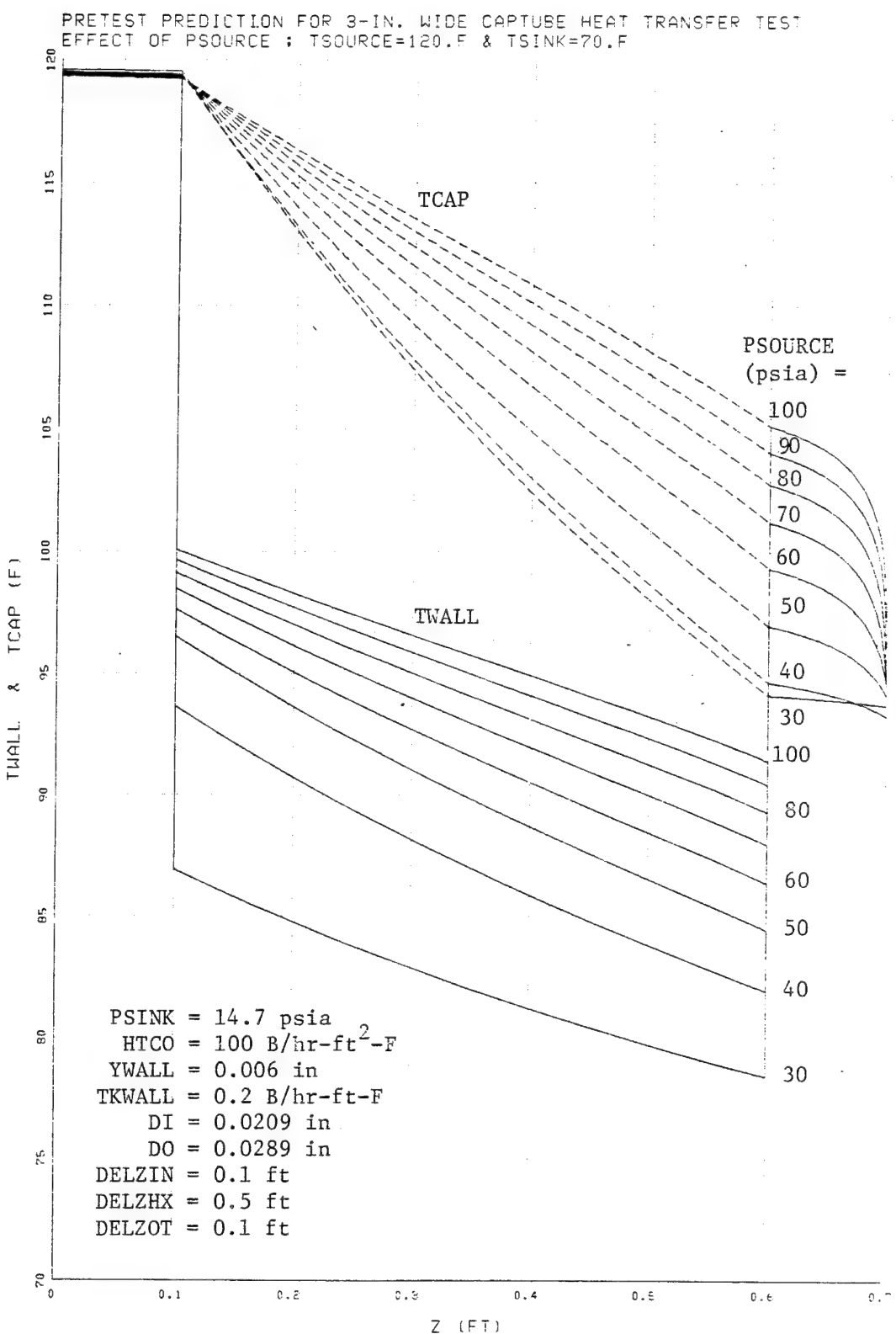


Figure 57

PRETEST PREDICTION FOR HEAT TRANSFER TESTS OF LARGER CAPTURE
TSOURCE=120.F & TSINK=70.F

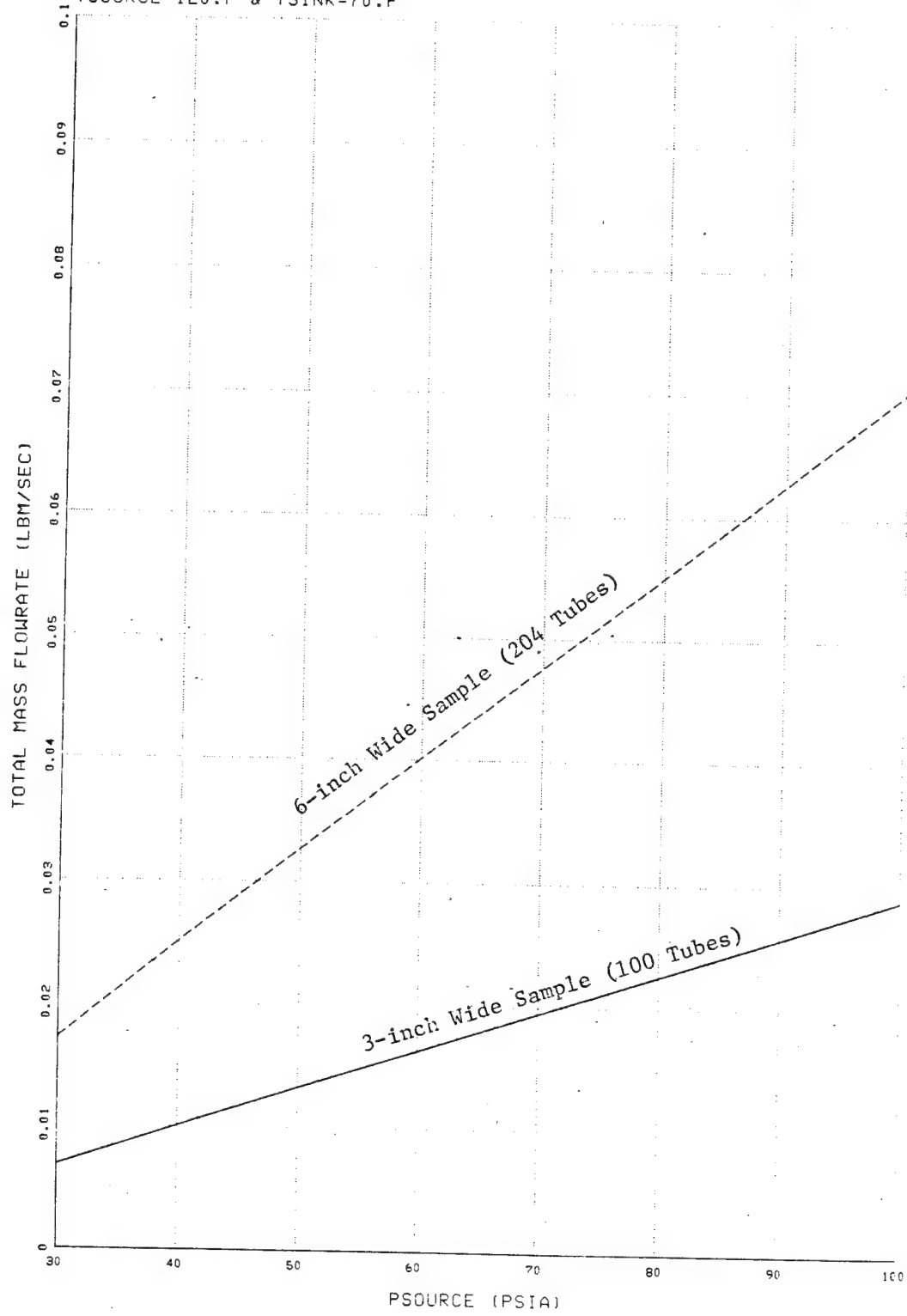


Figure 58

PRETEST PREDICTION FOR HEAT TRANSFER TESTS OF LARGER CAPTUBE
TSOURCE=120.F & TSINK=70.F

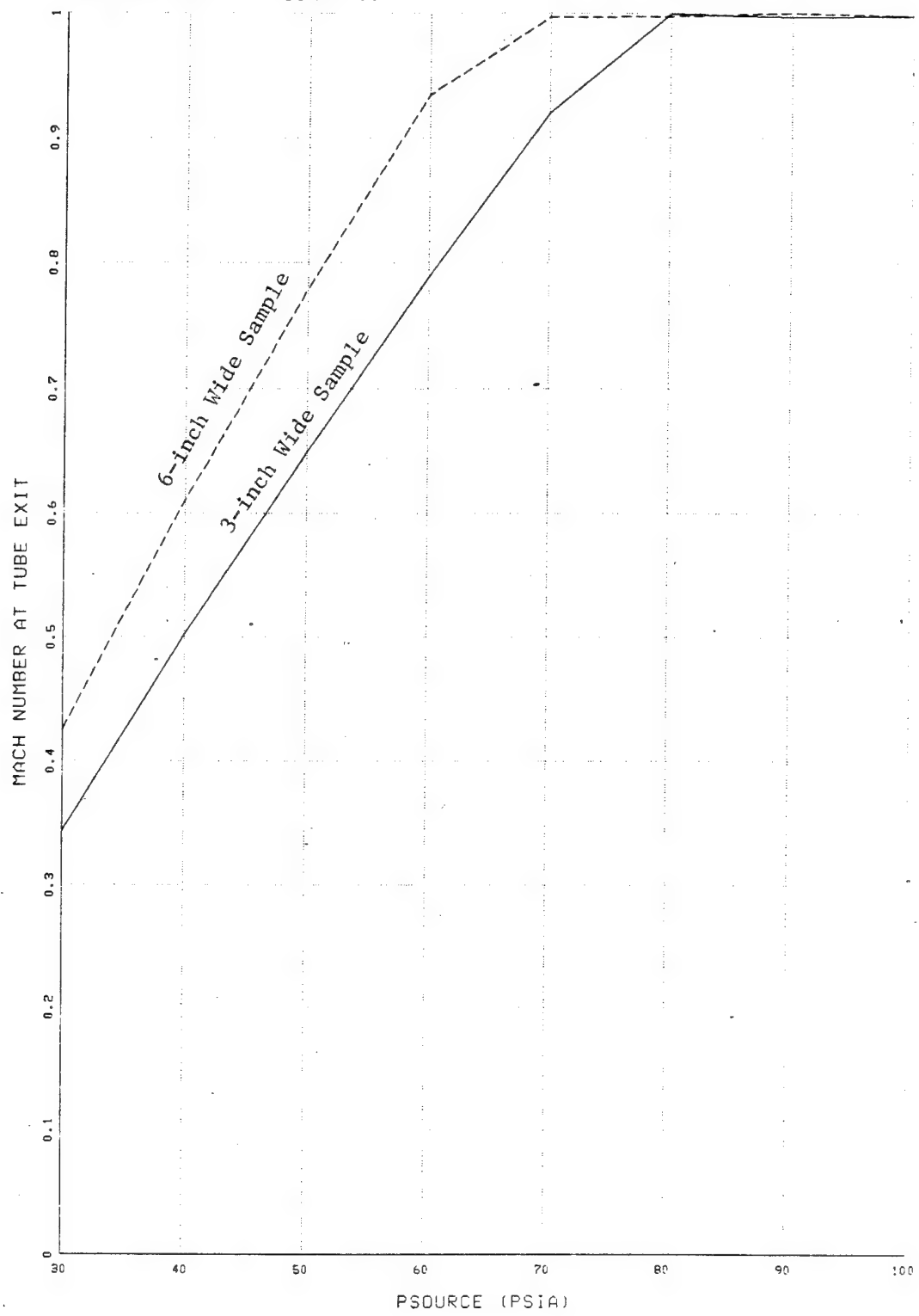


Figure 59

PRETEST PREDICTION FOR HEAT TRANSFER TESTS OF LARGER CAPTURE
TSOURCE=120.F & TSINK=70.F

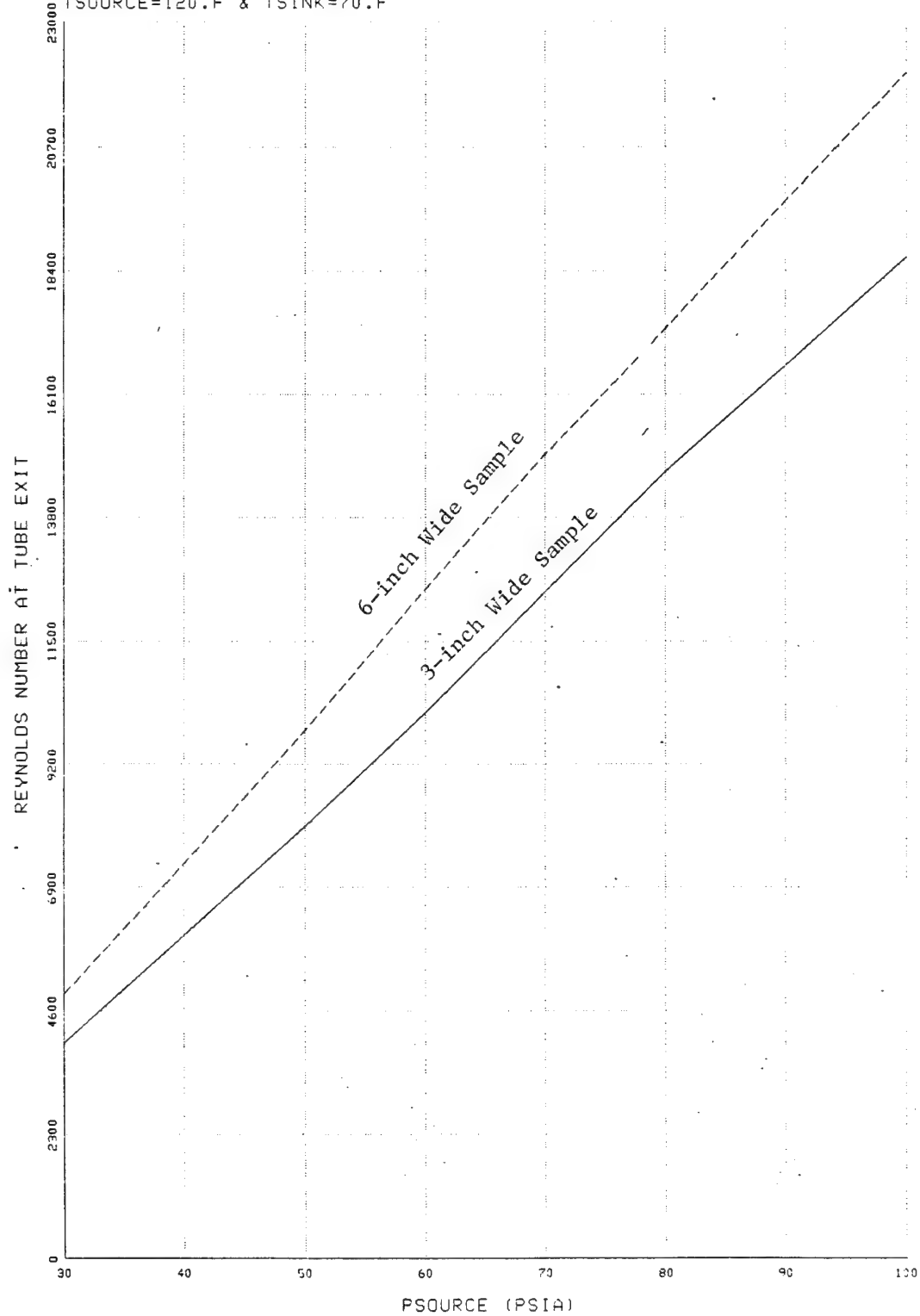


Figure 60

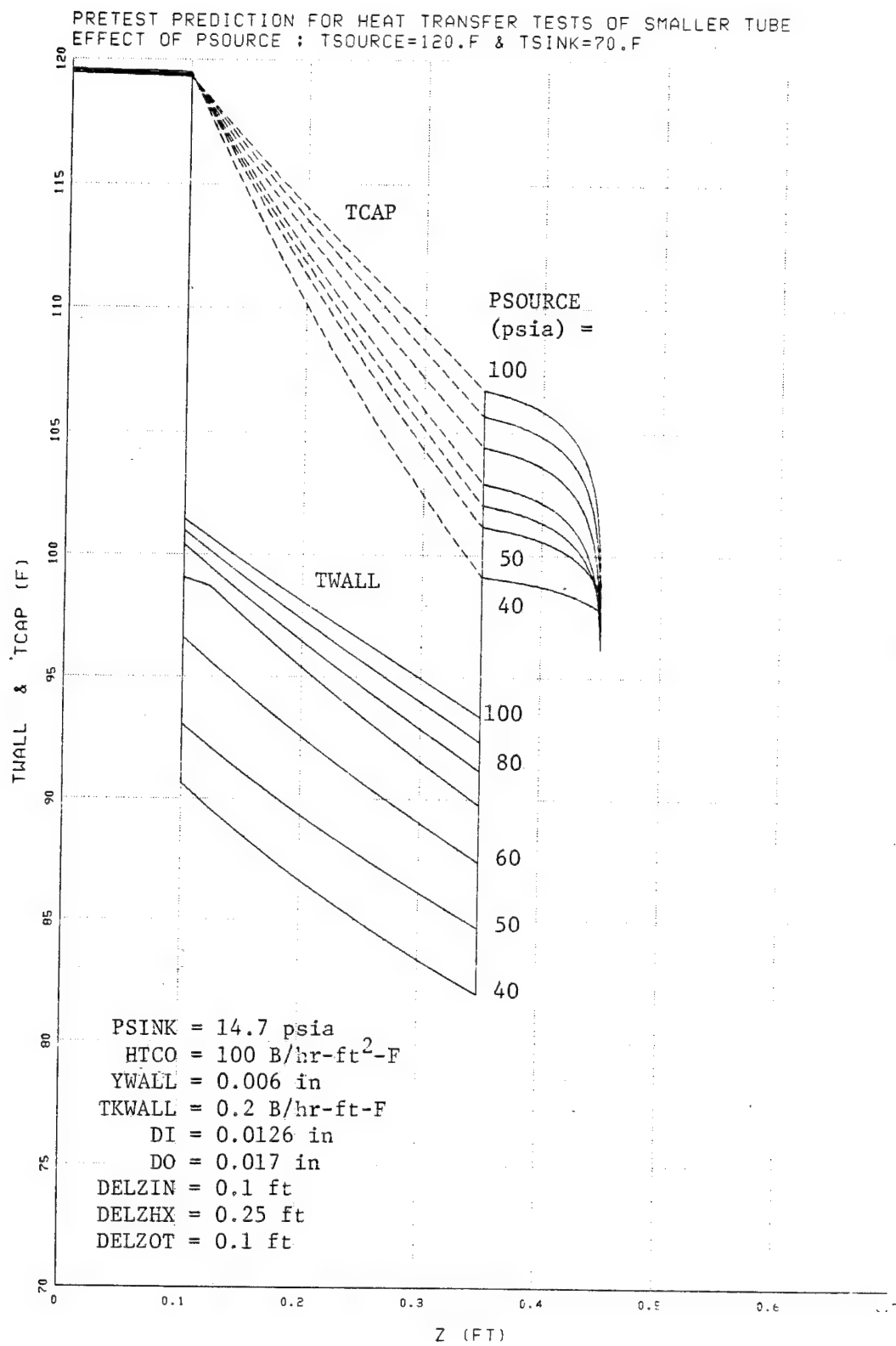


Figure 61

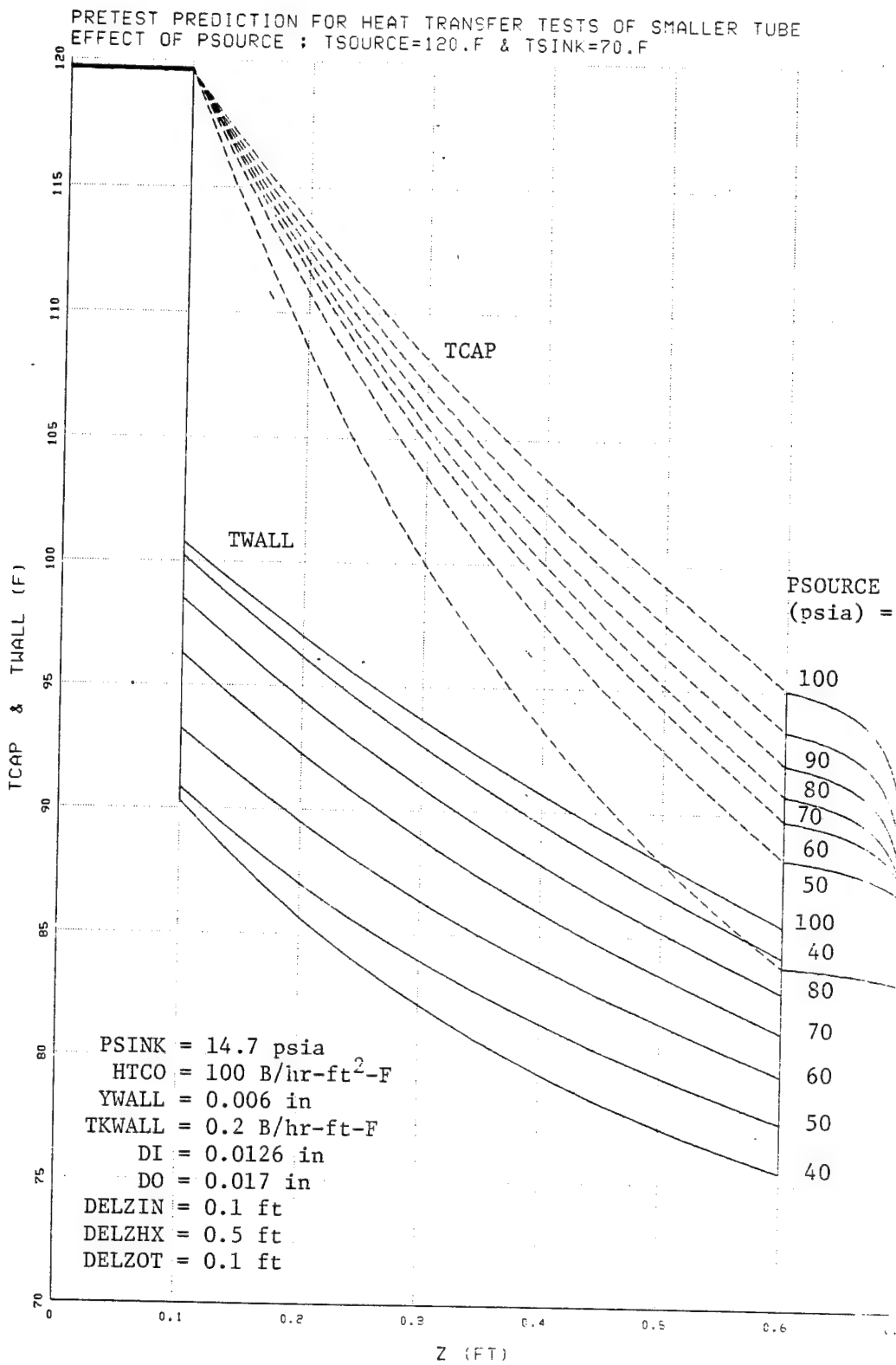


Figure 62

PRETEST PREDICTION FOR HEAT TRANSFER TESTS OF SMALLER TUBE
TSOURCE=120.F & TSINK=70.F

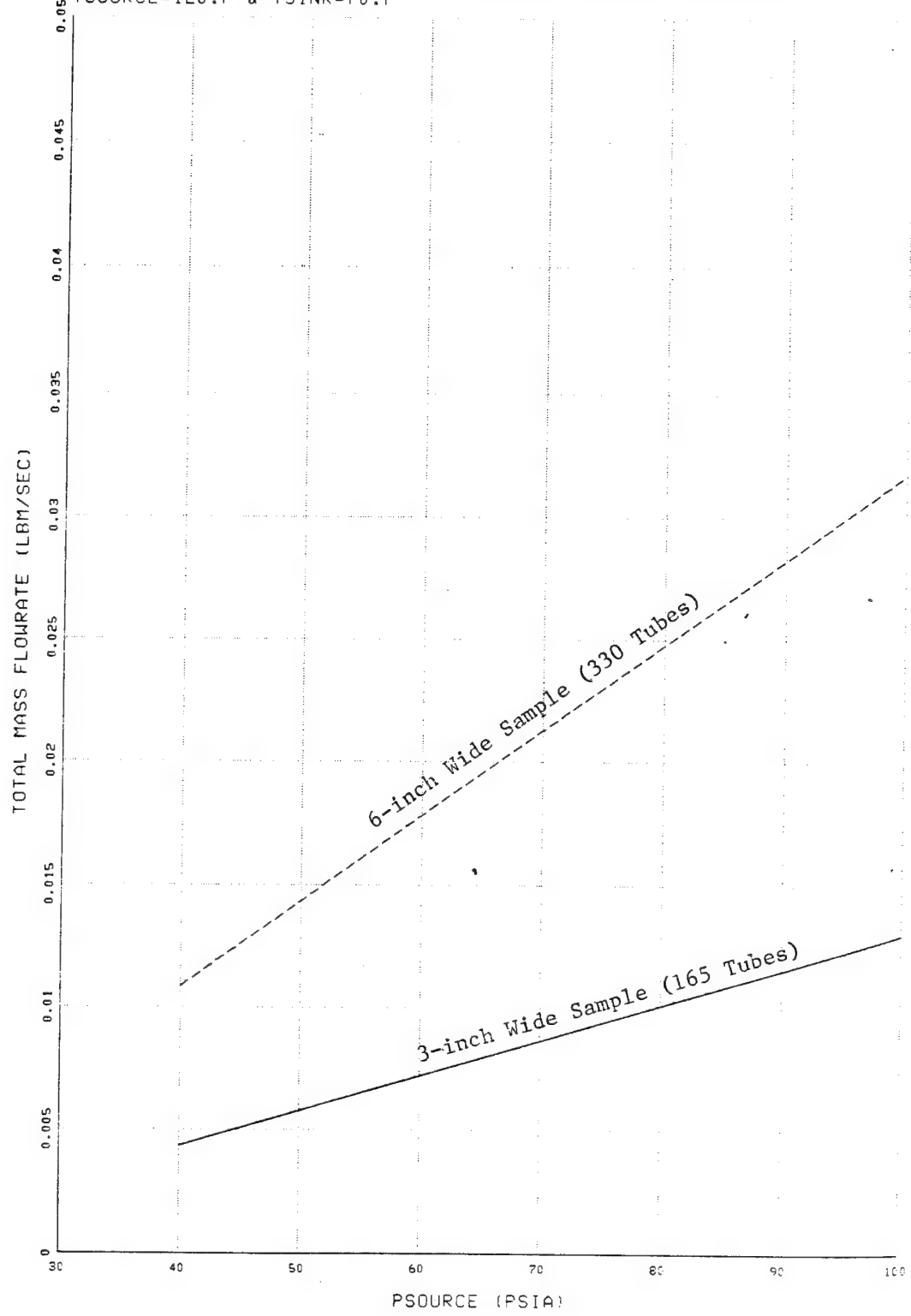


Figure 63

PRETEST PREDICTION FOR HEAT TRANSFER TESTS OF SMALLER TUBE
TSOURCE=120.F & TSINK=70.F

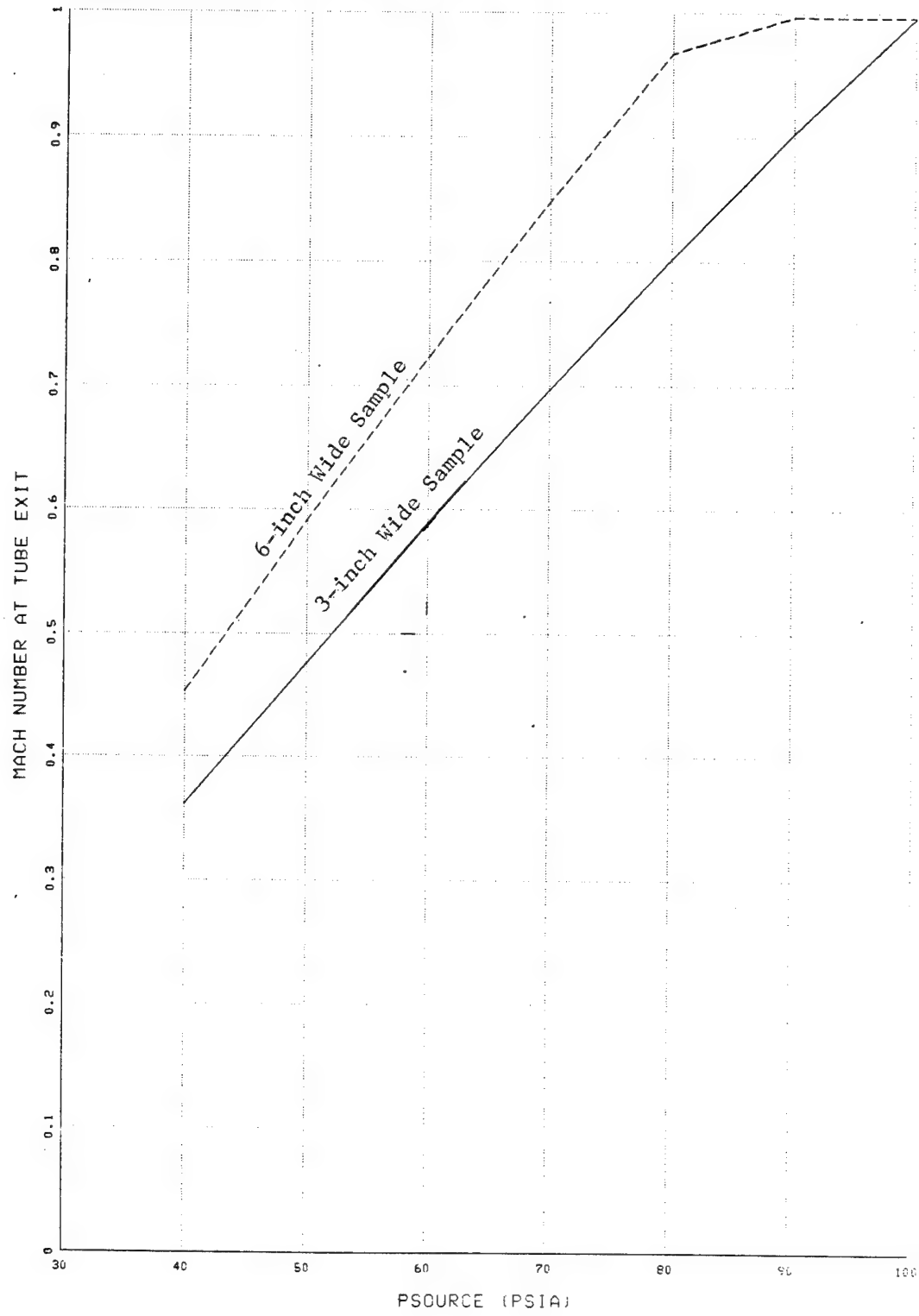


Figure 64

PRETEST PREDICTION FOR HEAT TRANSFER TESTS OF SMALLER TUBE
TSOURCE=120.F & TSINK=70.F

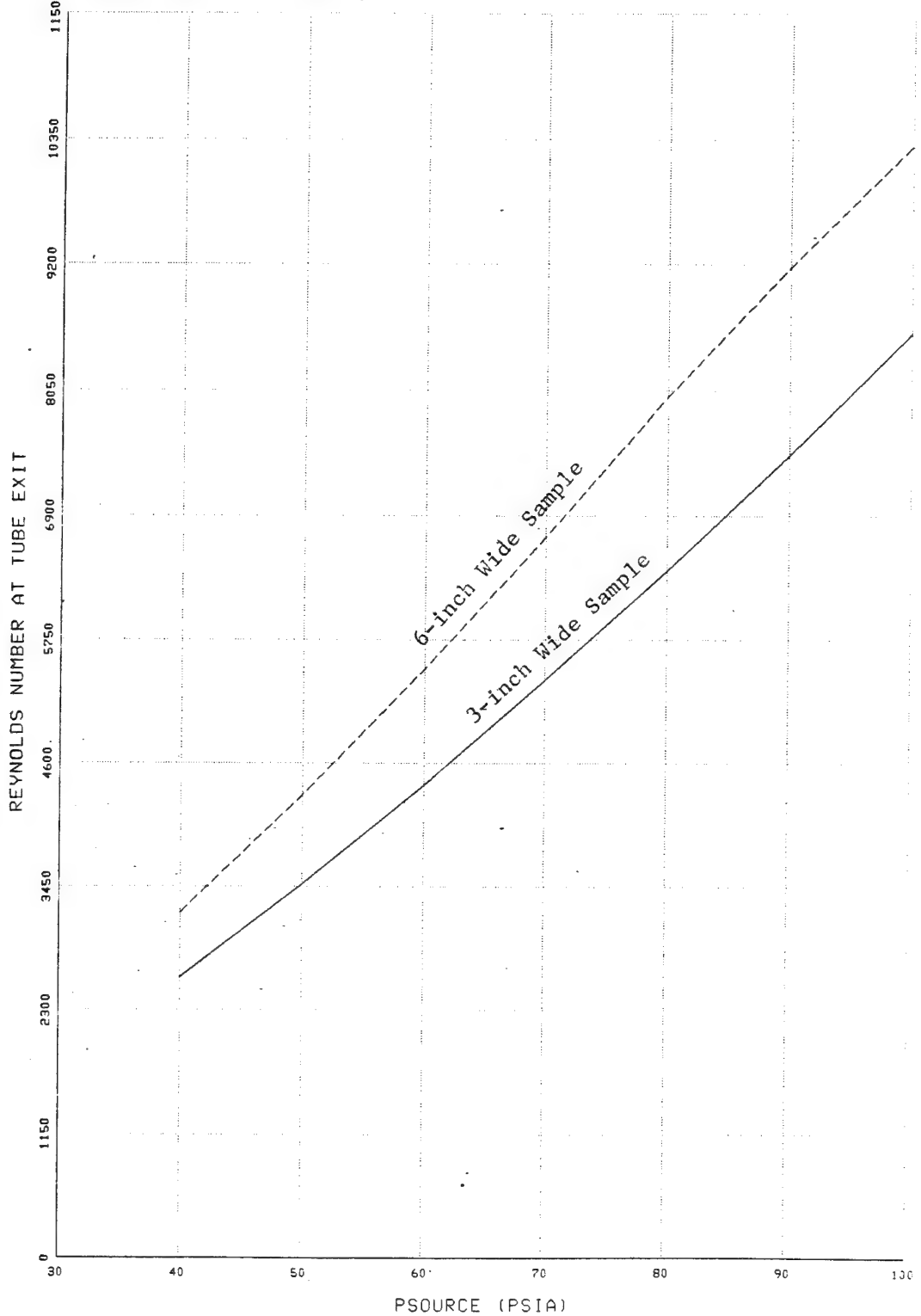


Figure 65

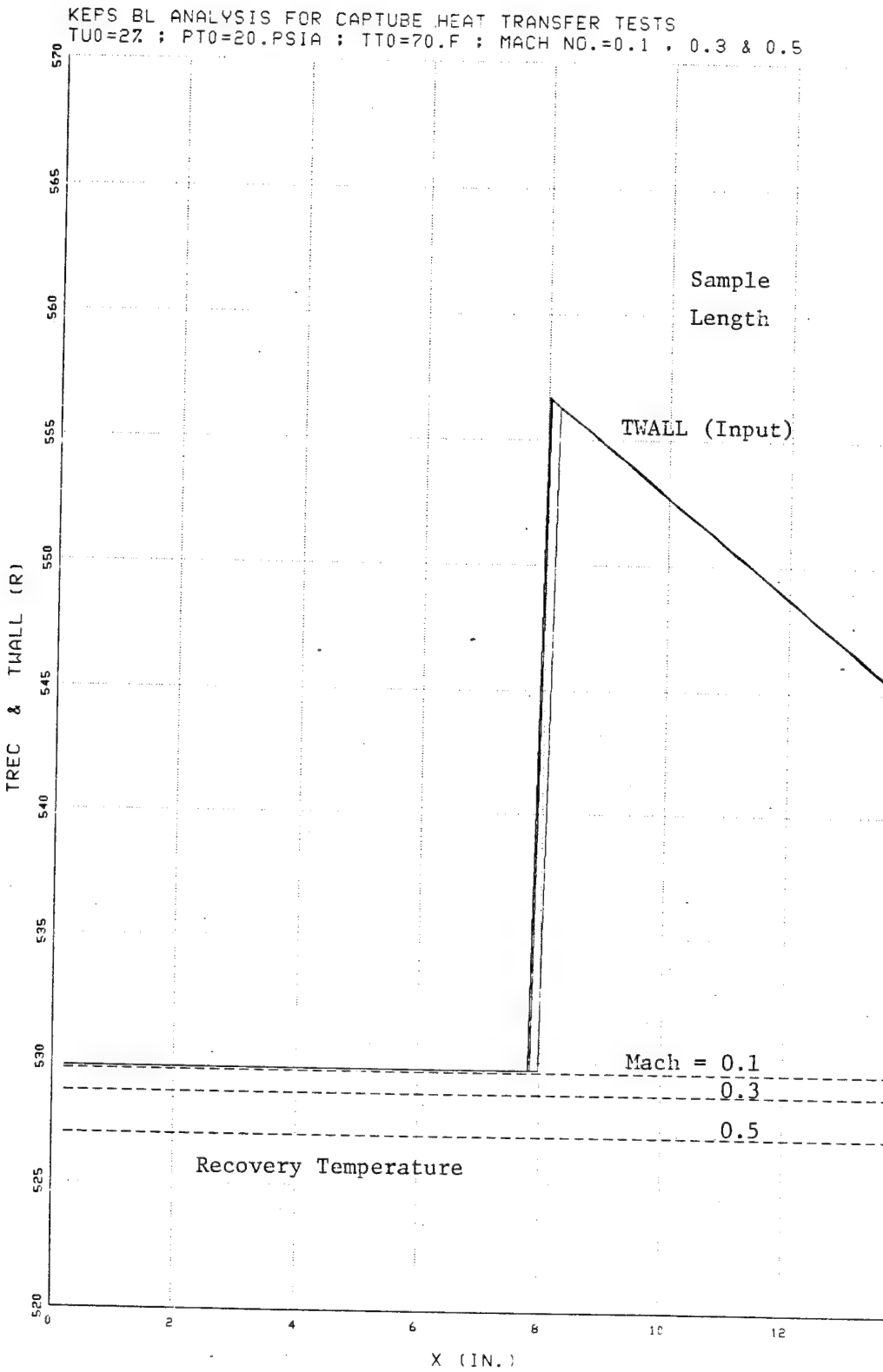


Figure 66

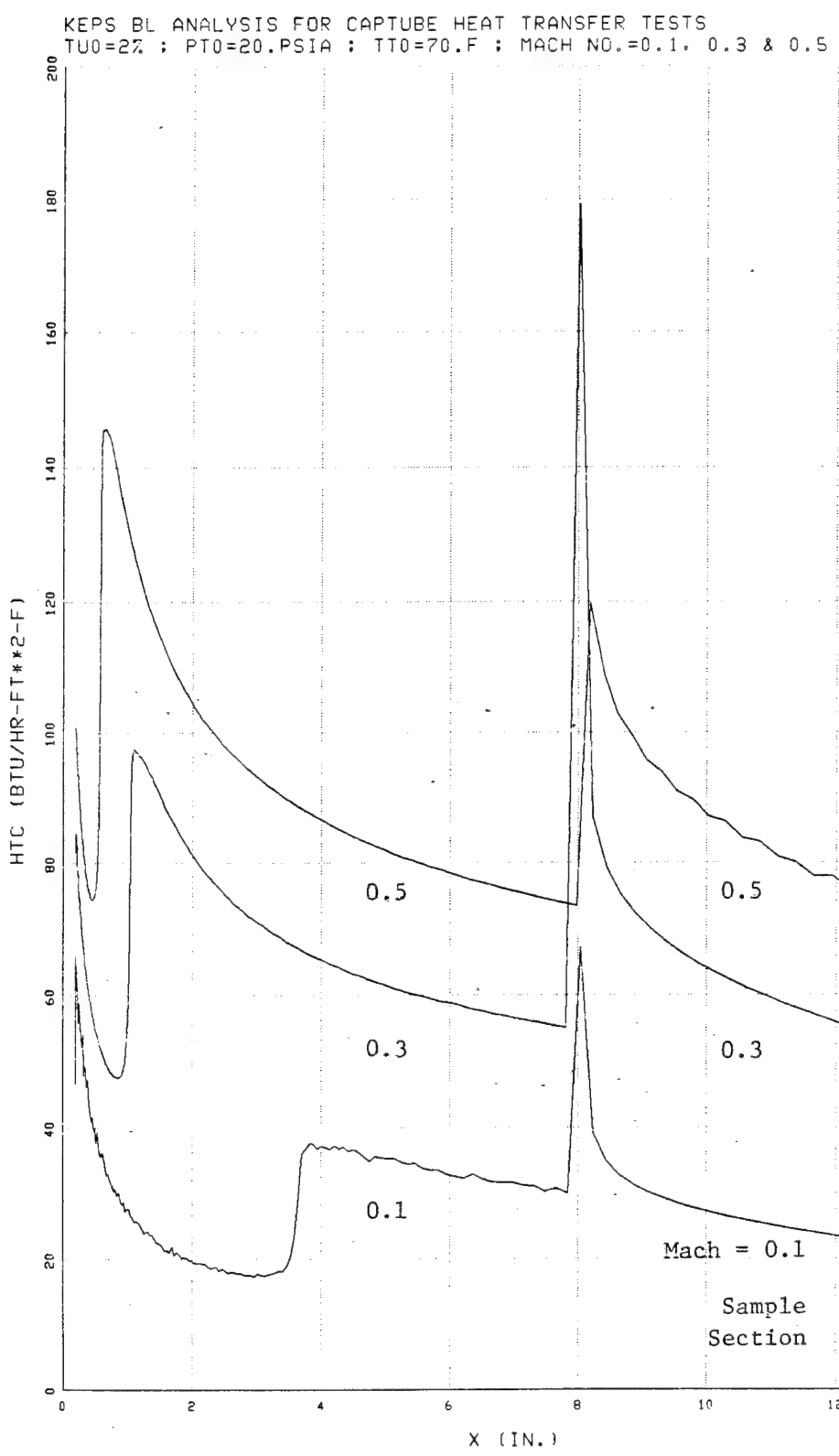


Figure 67

KEPS BL ANALYSIS FOR CAPTUBE HEAT TRANSFER TESTS
TU0=2% ; PT0=20. PSIA ; TT0=70.F ; MACH NO.=0.1 , 0.3 & 0.5

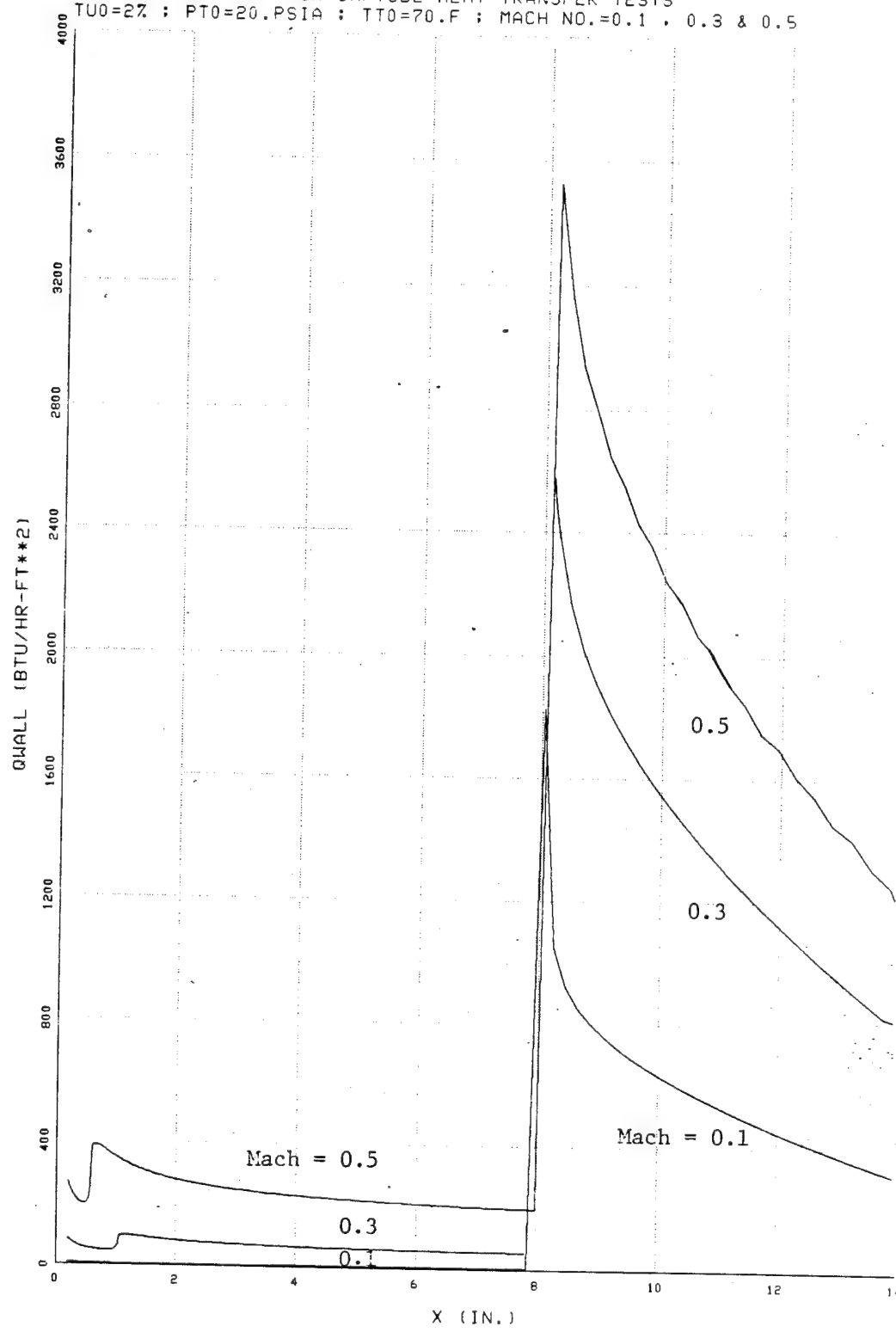


Figure 68

KEPS BL ANALYSIS FOR CAPTUBE HEAT TRANSFER TESTS
TU₀=2% ; PT₀=20.PSIA ; TT₀=70.F ; MACH NO.=0.1 , 0.3 & 0.5

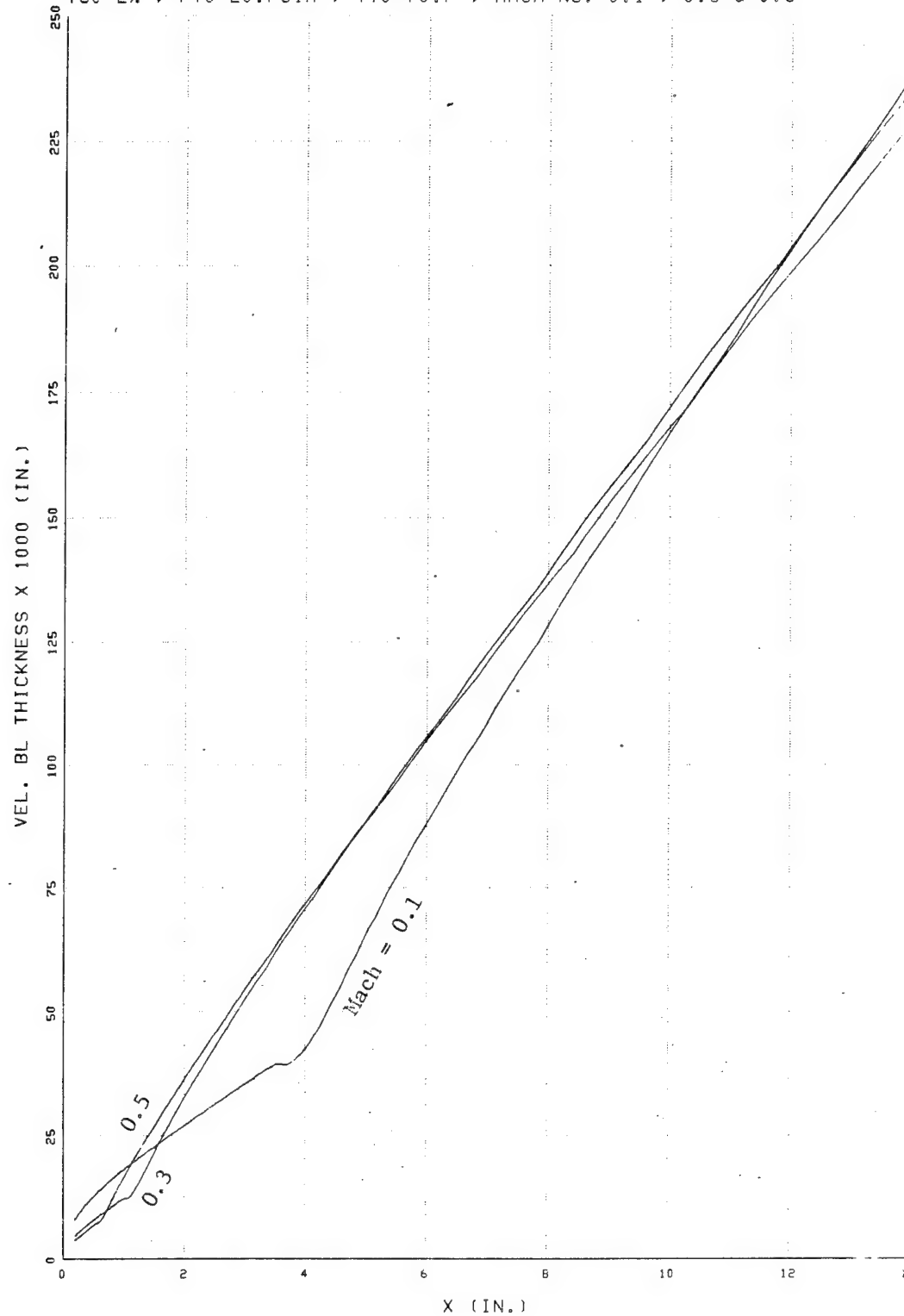


Figure 69

KEPS BL ANALYSIS FOR CAPTUBE HEAT TRANSFER TESTS
2-INCH PREHEAT SECTION : COUNTERFLOW AIR STREAMS

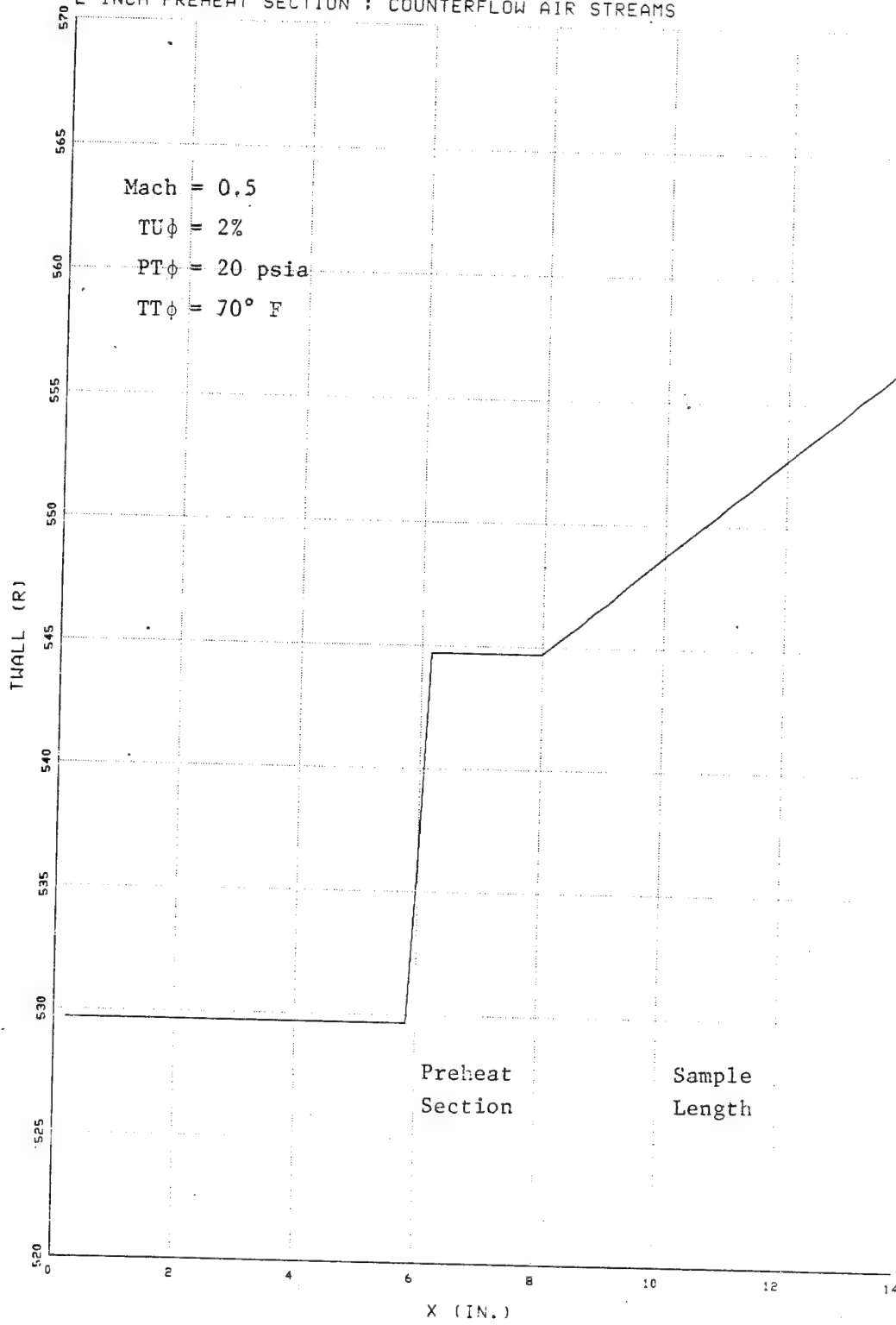


Figure 70

KEPS SL ANALYSIS FOR CAPTURE HEAT TRANSFER TESTS
2-INCH PREHEAT SECTION : COUNTERFLOW AIR STREAMS

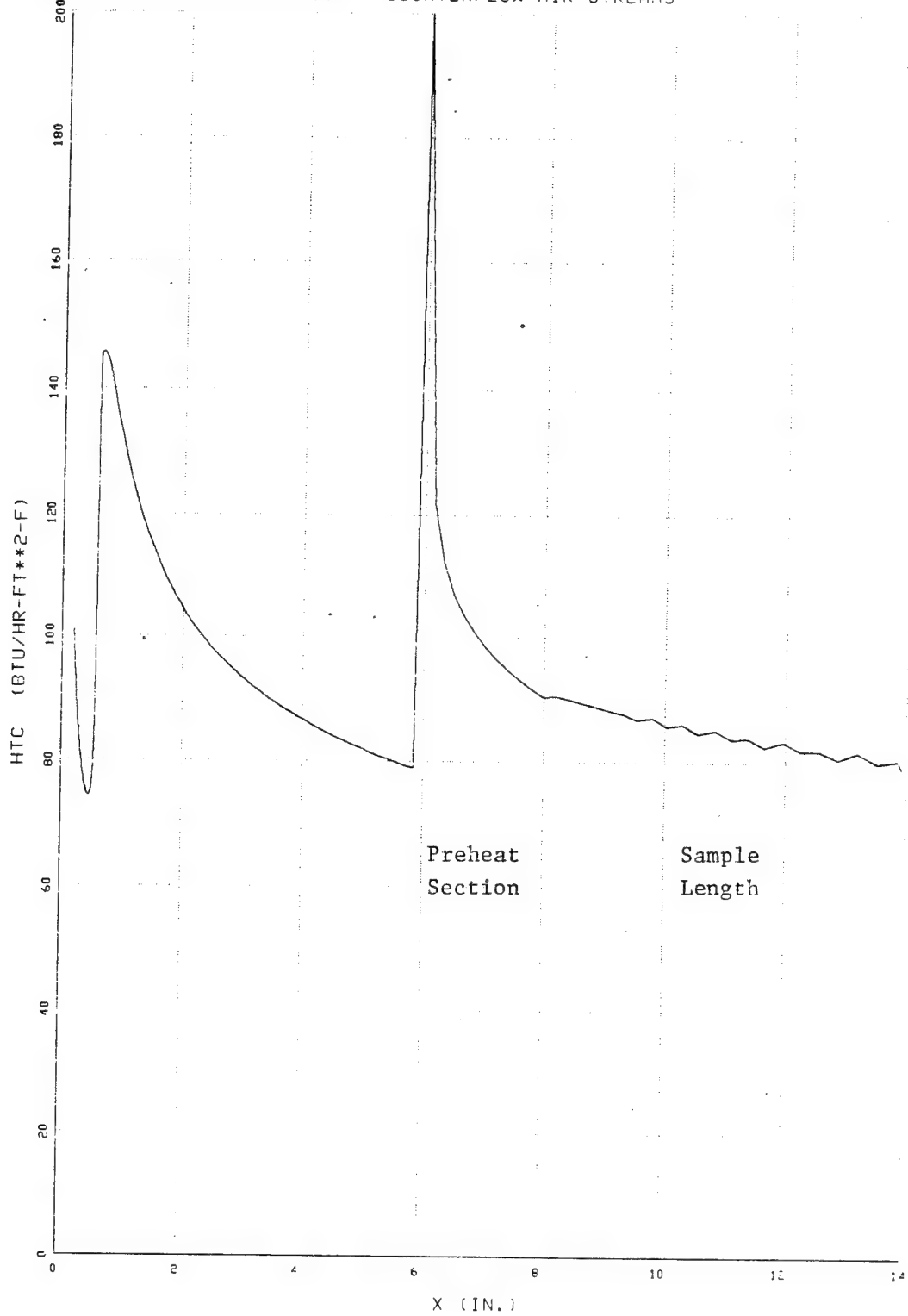


Figure 71

KEPS BL ANALYSIS FOR CAPTUBE HEAT TRANSFER TESTS
2-INCH PREHEAT SECTION : COUNTERFLOW AIR STREAMS

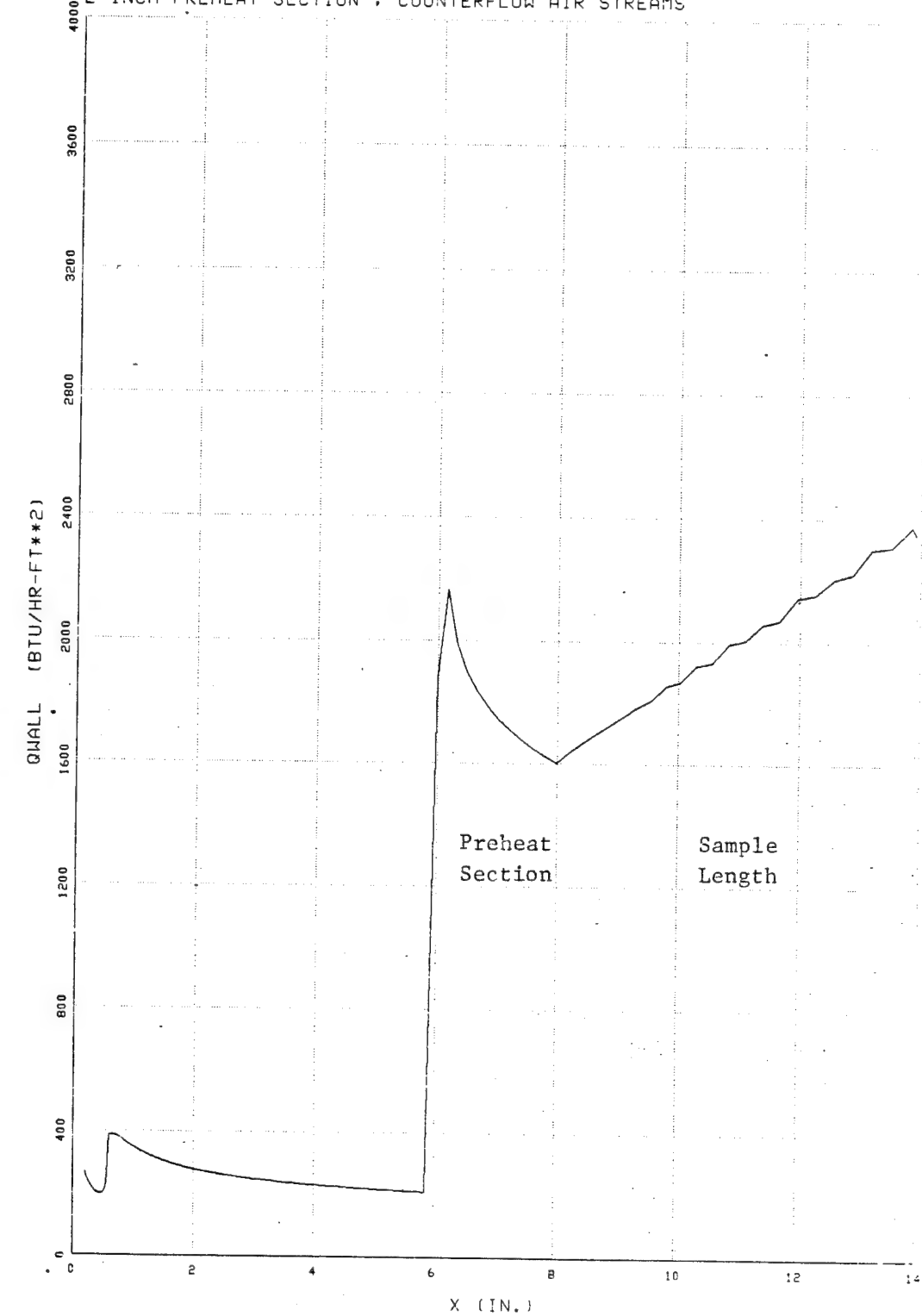


Figure 72.

SIMCAP Results

Results for the six inch wide by three inch long sample containing captubes with the larger diameter are plotted in Figures 49 through 65. The effect of hot-air source pressure and temperature on total mass flowrate of air through the 204 parallel captubes, and on Mach number and Reynolds number at the tube exit are shown in Figures 48 through 51. The effect of PSOURCE and TSOURCE on the air recovery temperature in the captubes (TCAP) and on the outside wall surface temperature along the sample (TWALL) are plotted in Figures 52 through 55. The effect of heat transfer coefficient at the outside surface of the sample (HTCO) on TCAP and TWALL are shown in Figure 56.

Similar results for the other three samples with a hot-air source temperature of 120°F are plotted in Figures 57 through 65.

5.4 Conclusions from the SIMCAP Analysis

- 1 It is not necessary to have extreme values of PSOURCE and TSOURCE in order to verify the capture simulation model. For example, a source pressure of 50 psia and a source temperature of 120°F give typical results.
- 2 There are very large step jumps in the sample surface temperature (TWALL) at the ends of the captubes where the sample is exposed to cold air at the sink temperature (TSINK). However, the temperature drop across the heat exchange length of the captubes is relatively small. (about 3.5°F in Figure 52, up to 24°F in Figure 55).
- 3 Figure 56 shows that a uniform heat transfer coefficient at the outside surface of the sample (HTCO) has a big influence on the mean temperature level of TWALL, but a negligible effect on the temperature drop along the heat exchange section of the surface.
- 4 The temperature distribution on the sample surface will be very sensitive to variations in the value of HTCO over the sample surface, and to end/edge effects. Such variations would make it difficult (if not impossible) to verify the capture thermal model, and variations in tube depth should therefore be reduced as much as possible.

5.5 Boundary Layer Results

The KEPS BL code was used to simulate the boundary layer on the duct wall preceding the sample surface, and on the sample surface. The length of the upstream duct wall was assumed to be eight inches followed by a sample length of six inches.

A thermal boundary condition input to the BL program is plotted in Figure 66. The duct wall temperature was specified as 70°F (529.7°R), and the sample temperature was assumed to decrease linearly from 97°F (556.7°R) at $x = 8$ inches to 85°F (544.7°R) at $x = 14$ inches. Note that a step jump in the wall temperature of 27 degrees is specified between the cold duct wall and the hot sample surface at $x = 8$ inches.

BL simulations were made for three different mainstream Mach number flows in the duct of 0.1, 0.3 and 0.5. The turbulent intensity in the duct mainstream was specified at 2%, with a total pressure of 20 psia and a total temperature of 70°F . The recovery temperature for the mainstream duct air at the three Mach number levels is also plotted in Figure 66.

The predicted variation of heat transfer coefficient along the duct and sample surface is plotted in Figure 67 for each Mach number about 0.5, 1.0 and 3.5 inches from the beginning of the duct wall for Mach number flows of 0.5, 0.3 and 0.1. Note also that a thermal spike occurs on the first inch of sample length following the step jump in wall temperature.

The predicted variations of heat flux and velocity BL thickness along the wall are plotted in Figure 68 and 69. A thermal spike again appears in the heat flux distribution at the beginning of the sample; however, the BL thickness is unaffected by the thermal BC, and it is not significantly affected by the mainstream Mach number. The velocity BL thickness is about 0.25 inches at the sample trailing edge, which is small compared to the duct gap of 2.5 inches.

The thermal spike at the leading edge of the sample followed by the large variation of HTC over the sample surface, as shown in Figure 67 is unacceptable. However, the situation can be improved by preheating the duct wall upstream of the sample to the same temperature as the sample leading edge, and by orienting the sample such that the duct air and the capture air streams are in counterflow. Thus, the thermal spike would occur upstream of the sample, and the rise of sample wall temperature in the direction of duct air flow would tend to diminish the variation of HTC on the sample surface.

To illustrate the effect of a preheat section followed by a linearly increasing sample wall temperature, the wall temperature distribution plotted in Figure 70 was input to the KEPS BL program. The mainstream Mach number was set at 0.5, and all other parameters were set at the same values used in the previous simulation.

The new results for HTC and wall heat flux are plotted in Figures 71 and 72. The thermal spike now occurs on the preheat section of the duct wall, and HTC varies from about 80 to 90 Btu/hr-sq. ft. -F on the sample wall. This variation of HTC on the sample could be reduced even more by providing an even longer preheat section; however, the average value of HTC on the sample surface would also decrease.

5.6 Conclusions from the Boundary Layer Analysis

1. An undesirable variation of Heat Transfer Coefficient (HTC) can develop on the outside surface of the test samples.
2. The variation of HTC on the sample surface can be reduced by heating the duct wall preceding the sample to the same temperature that occurs at the sample leading edge. Any step change of surface temperature will cause a thermal spike on the sample surface..
3. The variation of HTC can be further reduced by orienting the sample such that the duct air and the capture air streams are in counterflow.

6.0 Infrared Measurement of Surface Temperature

6.1 Infrared Temperature Measurement Sensor

Infrared measurement of composite material surface temperature was performed using a scanning radiometer with two spectral sensitivity bands of 3 to 5 microns and 8 to 12 microns. Measurements were taken using a radiometer setting which provided minimum temperature resolution of 1°F over a range of approximately 100°F. The spatial resolution of the thermal image was dependent on the surface area contained in the radiometer's field of view; each infrared image frame consists of 200 horizontal lines containing 250 resolvable elements per line. Data was available in standard television video format which was viewed in real time, and also stored on videotape for transfer to computer disk via a video image digitizer.

6.2 Measurement System Calibration

In order to accurately determine the composite material surface temperatures, the infrared temperature measurement system was calibrated based on the actual operating conditions and physical characteristics of the equipment utilized in the experimentation. Three primary items influence the accuracy of the infrared temperature measurement: (1) the radiometer measurement characteristics, (2) the transmission properties of the viewing optics, and (3) the emissivity of the thermal surfaces being observed. Experiments were conducted to determine the effect of these items on the wind tunnel measurements. In each case, the radiometer output test results were recorded on videotape for later processing by computer.

The calibration of the radiometer equipment requires a source of radiation with known intensities and spectral distribution. The "blackbody" source is ideal for this purpose because it provides radiation having well-known theoretical relationships between temperature and radiated energy. A reference source traceable to the National Bureau of Standards was used to generate radiometer image data over a temperature range which spans the composite surface experimental test temperature.

Sodium chloride (NaCl) was used as the optic material to provide both a visual and infrared viewing window for observing the composite surface under test. To determine the transmission properties of the NaCl, thermal radiation from a source of known emissivity was measured as viewed through the NaCl with the radiometer. During this testing, the NaCl material was heated to temperatures representative of actual test conditions. This information was used to compensate the infrared image data for changes in transmission due to temperature or local material variations in the NaCl.

Knowledge of the composite surface emissivity at the experimental test temperature is essential to accurate infrared temperature measurement. To determine surface emissivity, a sample of the composite material was heated, and radiometer images were recorded for a series of test temperatures spanning expected composite surface test conditions.

6.3 Preliminary Emissivity Test

The composite sample had a thin electric resistance heater mounted to the back surface, and a piece of insulating material next to the heater to minimize heat loss to the environment.

Three thermocouples were surface mounted, equidistant along the axial centerline, and four thermocouples were embedded near the sample edges. Temperature readings from these thermocouples were used as reference points to ensure stabilized and uniform heating during the test. Radiometer video images of the sample were recorded at 100, 125, 150, 175 and 200°F. The area surrounding the center surface thermocouple was selected as representative of the sample temperature.

Background data was obtained by maintaining all infrared camera settings constant and recording the video image of a front silvered mirror. A computer program was then used to adjust the digitized grey level data for the digitized background data and to reference the data with the known emittance from the blackbody. For each test temperature using this method, the emissivity was found to be constant over the temperature range within the accuracy of the experiment.

6.4 Data Acquisition

Steady-state temperature data were acquired using a combination of thermocouple sensors and the scanning radiometer. Figures 73 and 74 illustrate the infrared measurement test apparatus used to acquire composite surface thermal images of the test panel viewed in Figure 75. Thermocouples provided mainstream and capillary air temperatures. The video output of scanning radiometer was recorded on videotape to capture infrared image data of the composite surface thermal patterns at each experimental test point. All test data including calibration results were maintained in laboratory notebooks. Infrared image data was referenced to written data using laboratory notebook entries of tape count and electronically generated text headers which were inserted on the videotape immediately prior to recording the infrared image data. In addition to recording the infrared data on videotape for later analysis in the GE-AEBG Inspection Automation image processing laboratory, each test was observed in real time with a television display to provide monitoring of the thermal flow patterns during testing.

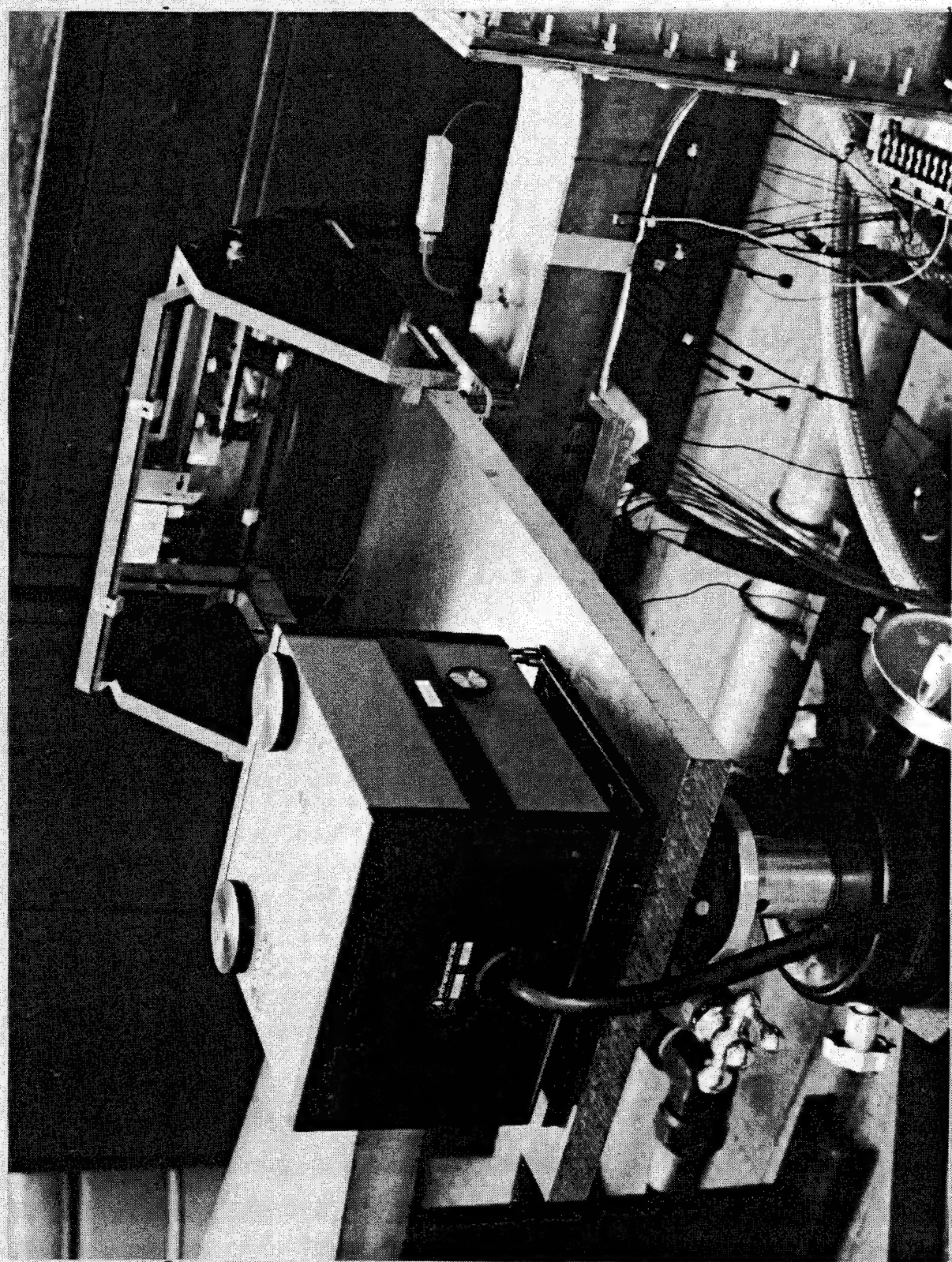


Figure 73 Infrared Measurement Test Apparatus

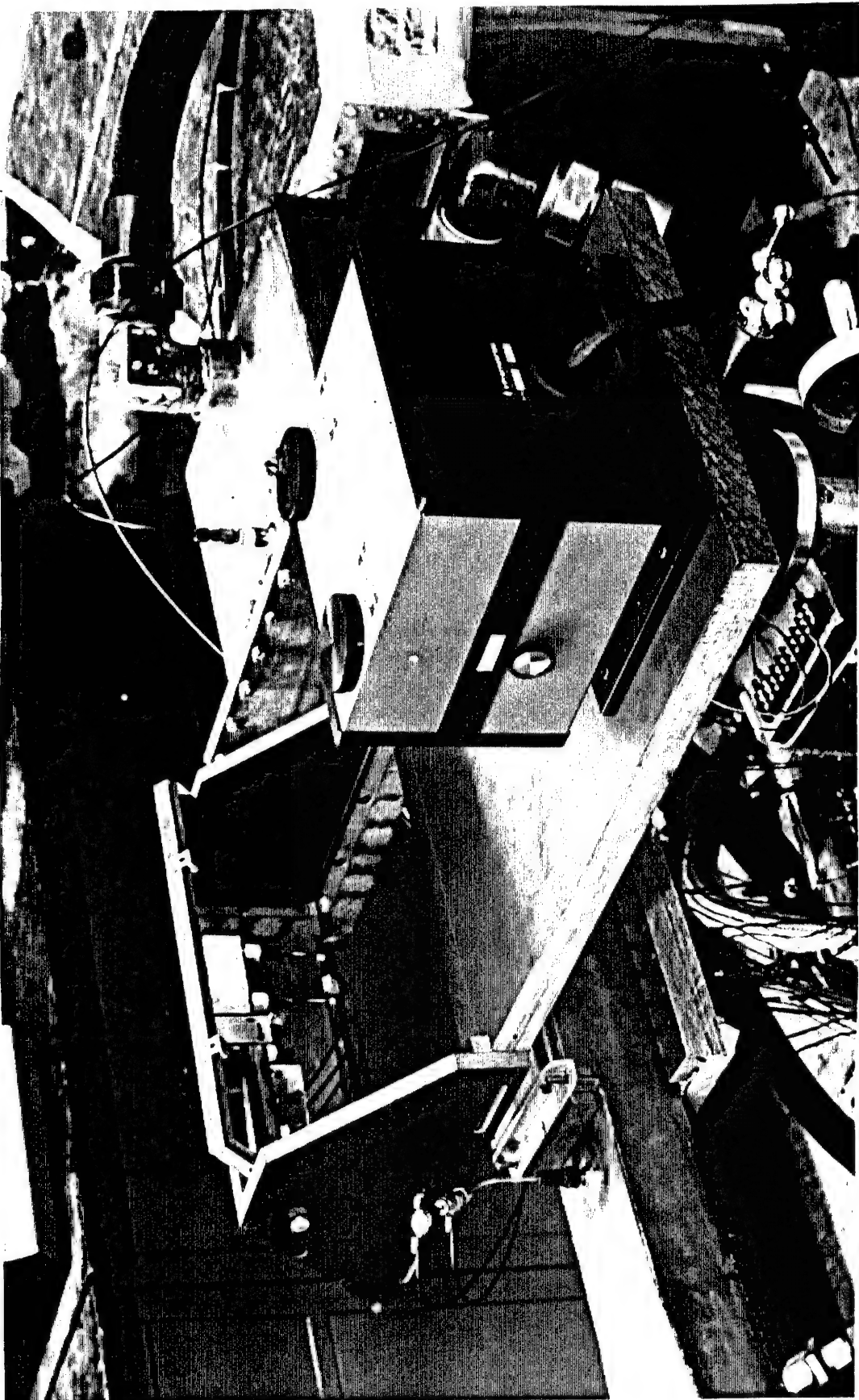
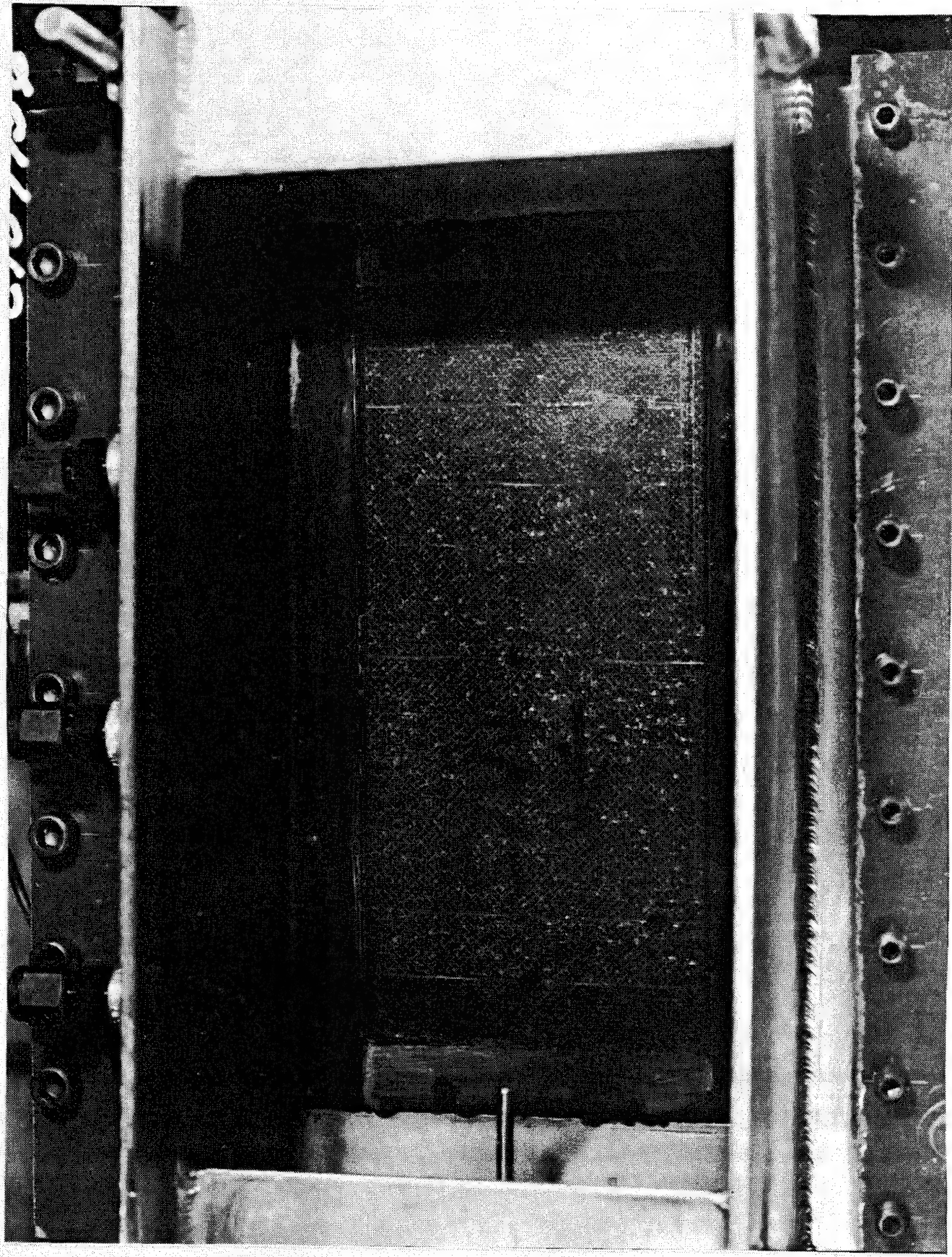


Figure 74 Infra-Red Camera Set-up to View Test Panel



6.5 Data Analysis

The recorded infrared images were digitized and transferred to computer disk for access by a variety of image processing and data analysis software routines. Digitized video image data were adjusted for intensity level using a known black and white reference generated electronically in the video image. Using image data files for NaCl transmission properties and composite surface emissivity in conjunction with calibration data for the radiometer obtained from blackbody measurements, the thermal image data was converted to temperature images. The resulting surface temperature computer files served as input to computer image display and analysis software.

Data analysis of the digitized images and the subsequent conversion from grey levels to temperature values was accomplished via several independent computer programs. In addition, a high resolution graphics terminal was utilized to generate statistical histograms displaying the composite material emissivity data and detailed temperature numerical printouts for each test point.

To assist in the visualization of the surface thermal pattern, the infrared temperature data were color enhanced for display on a high resolution video display unit. Plots of temperature variation were generated along lines or within regions as defined on the image of the composite surface using interactive graphics techniques.

6.6 Results

Color enhanced images for test point 120 are shown in Figure 76. The four images display the composite surface temperatures about a midpoint temperature of 151°F . In each image, the total range of displayed temperature data was divided into seven equal segments. These segments then were assigned a color which generated surface thermal patterns of equal temperature bandwidth. For example, Figure 76a illustrates color "isotherms" having a temperature bandwidth of 7°F . Likewise, Figures 76b, 76c, and 76d have 6°F , 5°F and 4°F per color band, respectively.. The heated capillary tube flow direction was left to right as shown in Figure 76. The resulting color patterns show a decrease in temperature across the composite surface from left to right resulting from the cooling effect of the mainstream flow.

Color enhanced images for test points 112 and 114 are shown in Figures 77a and 77b with their accompanying temperature printouts below each in Figure 77c and 77d. Both points were taken with primary flow at 2.02 pps, primary temperature at 60.5°F . Capillary pressure for point 112 was 10" Hg, and for point 114 was 30" Hg.

These examples of image and numerical data are representative of the large amount of both qualitative and quantitative information obtained from the infrared thermal image measurements. The visualization of the thermal surface patterns obtained in real-time during the experimentation and in computer enhanced digital images

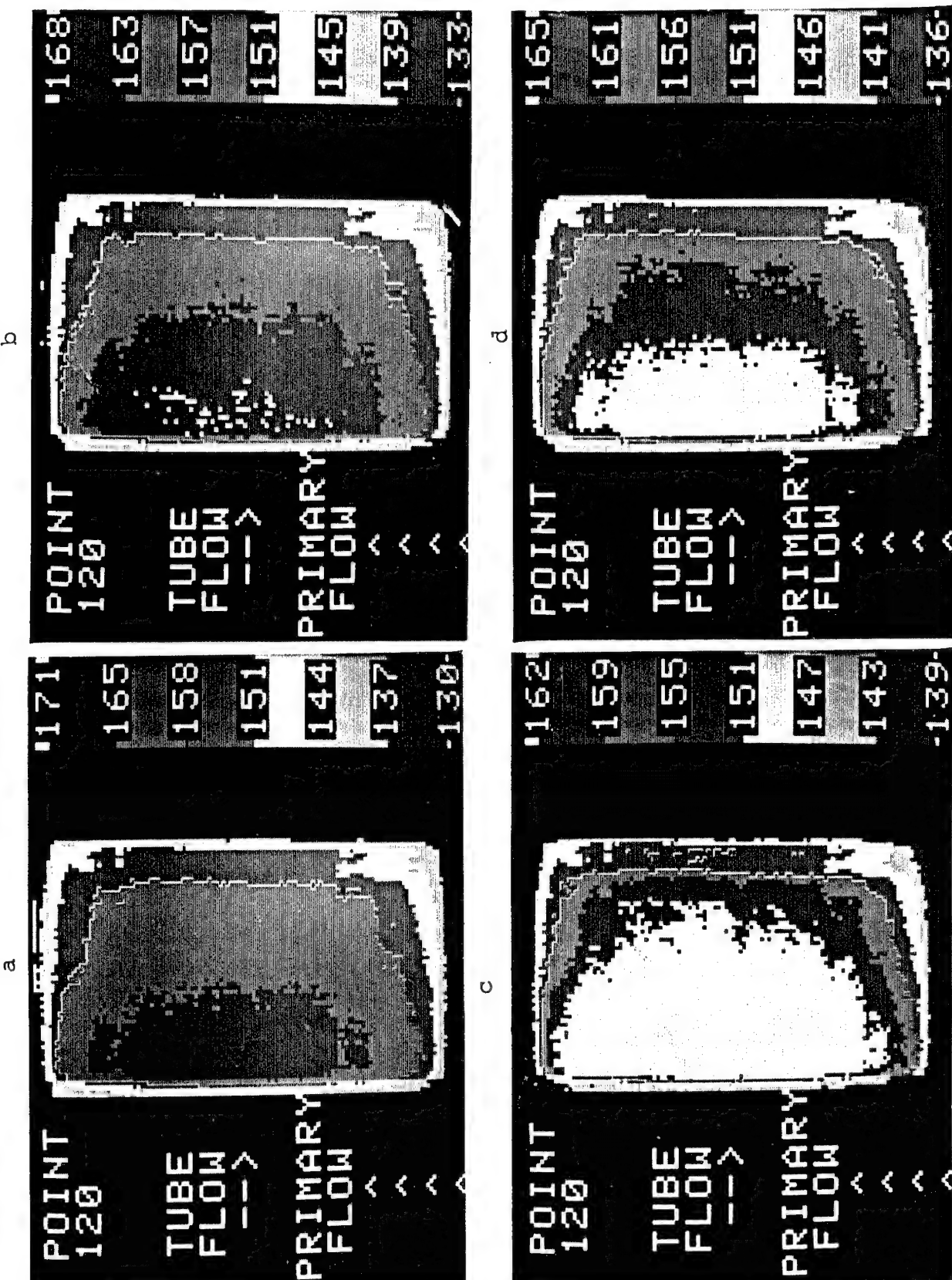


Figure 76 Computer Color Enhanced Images for Test
Point 120 - showing successively narrower temperature windows

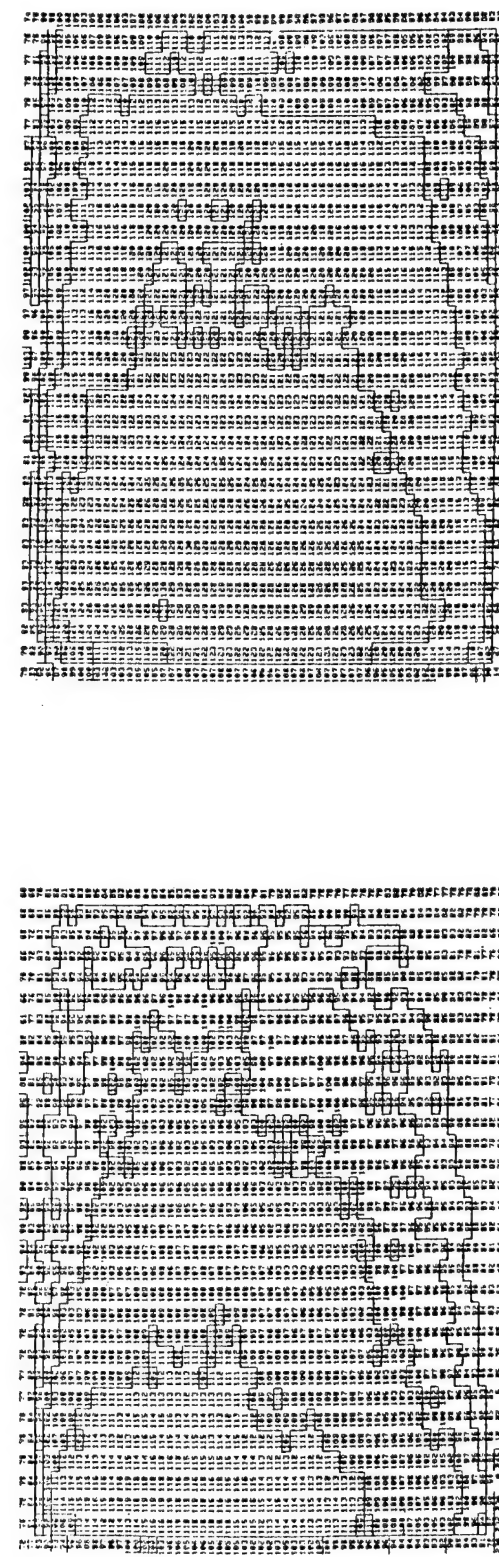
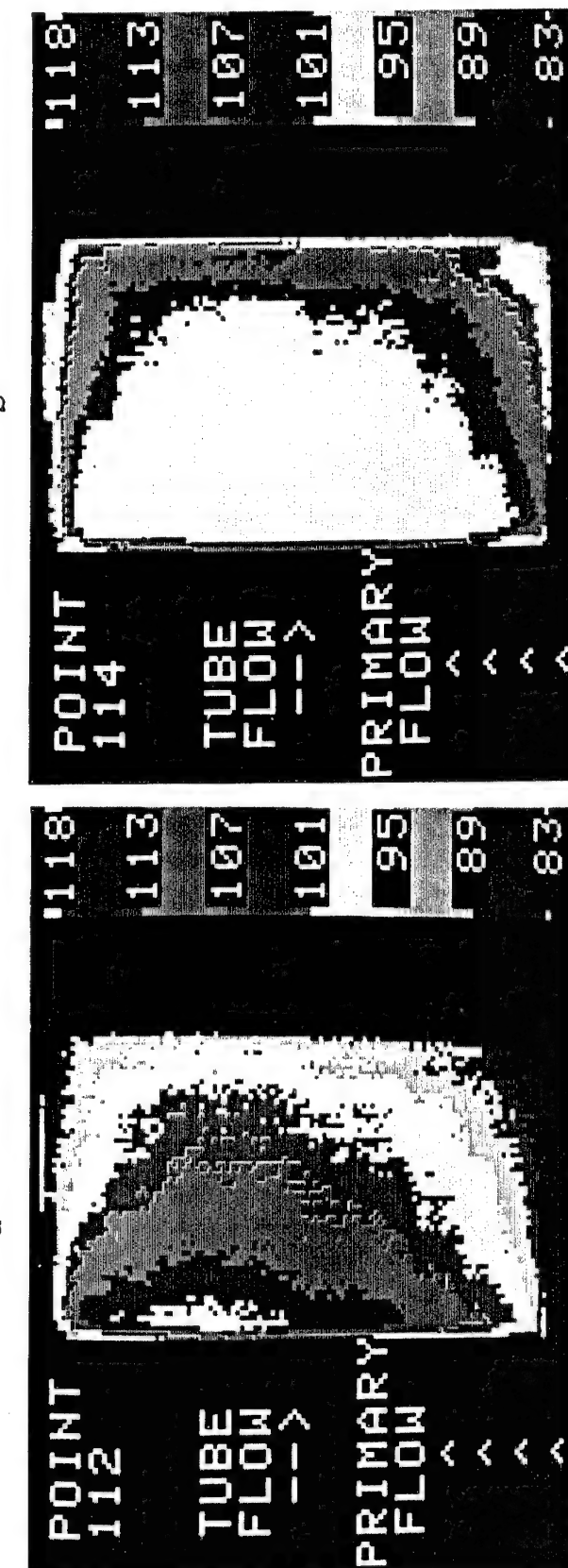


Figure 77 Colorized Images with Corresponding Temperature Maps, Describing Two Test Points

provided information useful for qualitatively evaluating the effect of different capillary tube and mainstream flows. Comparison of infrared-based and thermocouple data indicated that a good correlation could be obtained between the two measurement techniques. The infrared method, however, provided more detailed temperature maps of the composite material thermal behavior than was available from conventional techniques.

7.0 COMBINED 2D WALL HEAT CONDUCTION AND 1D COMPRESSIBLE TUBE AIR MATHEMATICAL MODEL

7.1 Thermal Analysis of Capillary Reinforced Composites

A computer program named SIMCAP was previously developed to simulate the steady-state thermal performance of capillary tube embedded within a composite wall. Negligible spacing between adjacent capillary tubes was assumed.

The SIMCAP code includes a one-dimensional heat conduction model at a typical cross section of a tube combined with a one-dimensional compressible flow model along the tube.

It is of interest to determine the effect of tube spacing upon thermal performance, and to determine if multiple layers of tubes can significantly influence the surface temperature of a composite wall. Therefore, a two-dimensional heat conduction analysis was made at a typical cross section of the wall, and results are described in this report.

A correlation for two-dimensional conduction shape factor for a single layer of spaced tubes was also derived and inserted into a modified version of SIMCAP. Computed results for composite wall surface temperature as a function of tube spacing are also presented.

7.2 Two-Dimensional Heat Conduction Analysis

Consider the cross section of a tube/wall assembly represented in Figure 78. One wall surface is exposed to hot air at temperature TSOURCE, and the other wall surface is exposed to cold air at temperature TSINK. Hot air at TSOURCE enters one end of the tubes and flows through the tube length.

A layer of tubes with outside diameter $D=2R$ and uniform spacing, SPACE, is located at depth YWALL from the cold wall surface. An optional second layer of tubes centered in the spaces between the upper layer of tubes, and at a greater distance from the cold wall surface, is also represented in Figure 78.

The conduction analysis will focus on a basic area bounded by lines of symmetry for a single tube. The width of such an area is designated in Figure 78 by "CONTROL WIDTH"; this width is equal to $(R+SPACE/2)$.

A computer program called BIE4 is available at General Electric* for analyzing two-dimensional heat conduction problems. It is particularly convenient and economical for analyzing the basic conduction problem represented in Figure 78 and will, therefore, be used in this analysis.

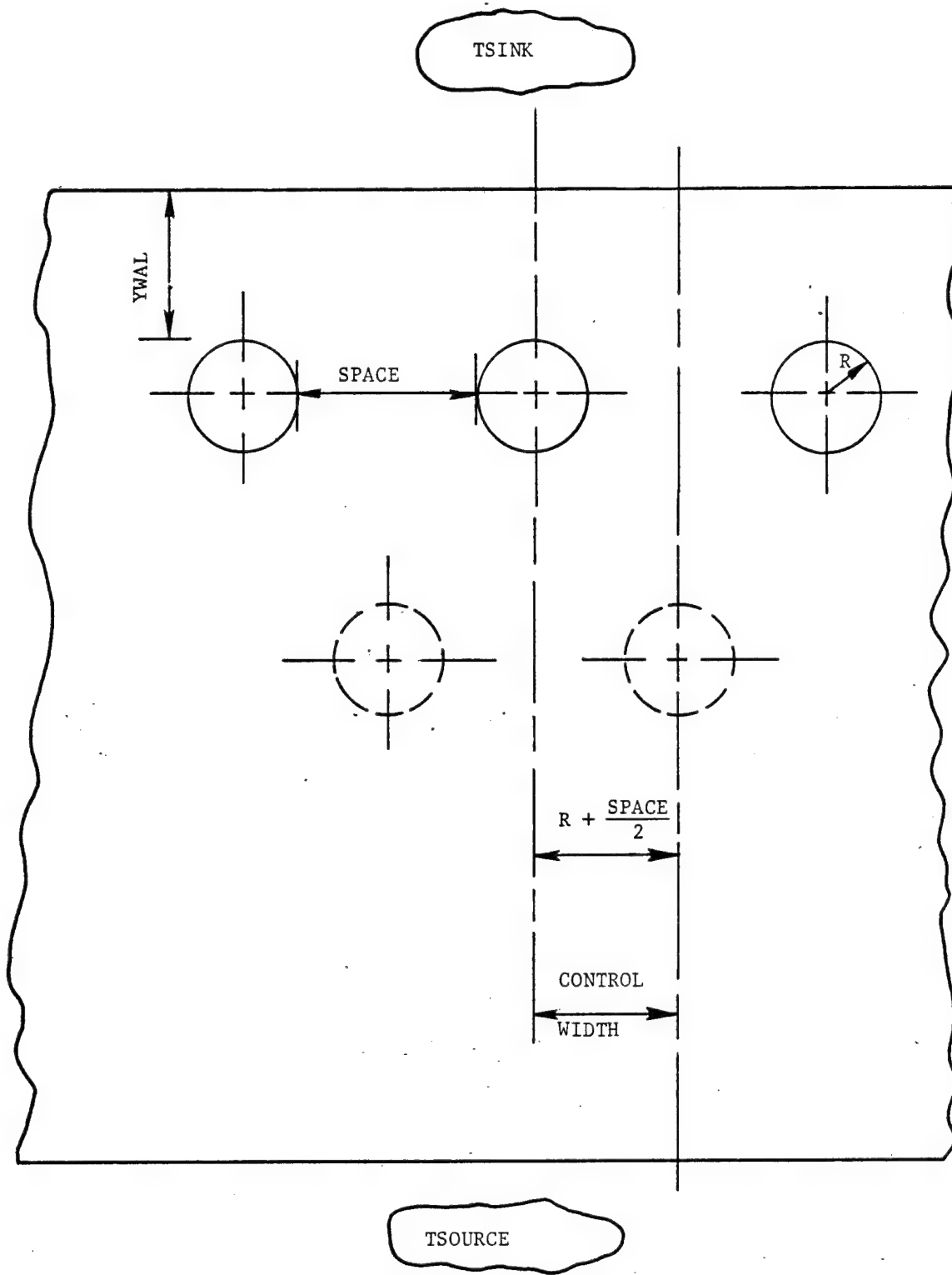


Figure 78 Basic Conduction Problem.

7.2.1 Analysis of a Simple Test Case: A Plane Wall

In order to test the BIE4 program, a simple plane wall was first considered so the BIE4 results could be compared to exact analytical results.

The control area for the plane wall test case is shown in Figure 79. The heat transfer coefficient is $HTCO$ at the cold wall surface, and $HTCL$ at the hot wall surface. The wall temperature is TWO at the cold surface, and TWL at the hot surface. The thermal conductivity of the wall material is k .

The width ($3R$) and thickness ($17R$) of the control area are representative of a composite wall. The vertical sides of the control area are specified as adiabatic.

An equation for the rate of heat transfer (per unit depth) from $TSOURCE$ to $TSINK$ through the wall is:

$$q' = \frac{[TSOURCE - TSINK]}{\frac{1}{3R(HTCO)} + \frac{17R}{3Rk} + \frac{1}{3R(HTCL)}} \quad (20)$$

Equation (20) can be rearranged to the following dimensionless form:

$$(q' / k \Delta T) = \frac{3}{[1/B0 + 17 + 1/BL]} \quad (21)$$

Where the following parameters are defined:

$$\Delta T = TSOURCE - TSINK \quad (22)$$

$$B0 = R(HTCO)/k \quad (23)$$

$$BL = R(HTCL)/K \quad (24)$$

The dimensionless temperature at the cold wall surface is given by the following equation:

$$TWO* = (q' / k \Delta T) (1/3B0) \quad (25)$$

Where $TWO*$ is defined as

$$TWO* = \frac{[TWO - TSINK]}{[TSOURCE - TSINK]} \quad (26)$$

* Gibbs, R.W. and Kilduff, K.A., "2-D Heat Transfer Computer Program Using the Boundary Integral Equation Method: BIE4", TIS Report 82-GTD-12, April 1981.

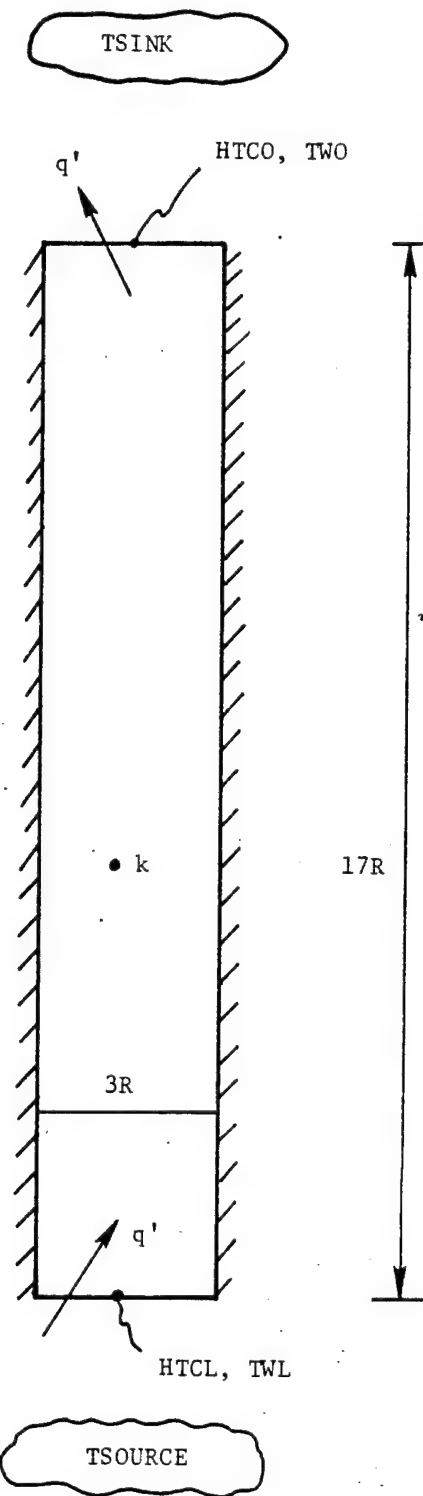


Figure 79 Simple Plane Wall Test Case.

If the following representative parametric values are specified,

$$HTCO = 100 \text{ (Btu/hr-ft}^{\frac{1}{2}}\text{)} \quad (27)$$

$$HTCO = 10 \text{ (Btu/hr-ft}^{\frac{1}{2}}\text{)} \quad (28)$$

$$k = 0.2 \text{ (Btu/hr-ft-}^{\circ}\text{F)} \quad (29)$$

$$R = 0.01445 \text{ inch} \quad (30)$$

then the dimensionless surface heat transfer coefficients become:

$$BO = 0.60208 \quad (31)$$

$$BL = 0.060208 \quad (32)$$

After these values are substituted into Equations (21) and (25), the following values of dimensionless heat transfer and cold wall surface temperature are obtained:

$$(q'/k\Delta T) = 0.08506 \quad (33)$$

$$TWO* = 0.04709 \quad (34)$$

Note that the cold wall surface temperature is only 4.709% of ΔT greater than $TSINK$. That is, if $TSINK=0^{\circ}\text{F}$ and $TSOURCE = 200^{\circ}\text{F}$, then $TWO = 9.418^{\circ}\text{F}$. Thus, the cold wall surface temperature would be colder than the freezing temperature of water, unless capillary tube heating is added to the wall.

The simple plane wall problem was input to the BIE4 program, and the computed values for dimensionless heat transfer and wall surface temperature agreed with the above values to within five decimal places.

7.2.2 Analysis of the Reference Case

The effect of adding a single layer of capillary tubes was considered next. The control area for the reference case is shown in Figure 80. The tubes were specified at a depth of $3R$, and the dimensionless heat transfer coefficient at the tube surface was specified as

$$Bl = 1.64206 \quad (35)$$

The reference problem was input to the BIE4 program, and the following values of dimensionless heat transfer at the cold wall, tube, and hot wall surfaces were computed:

$$(q'/k'T)_0 = 0.48938 \quad (36)$$

$$(q'/k'T)_1 = 0.47962 \quad (37)$$

$$(q'/k'T)_L = 0.00976 \quad (38)$$

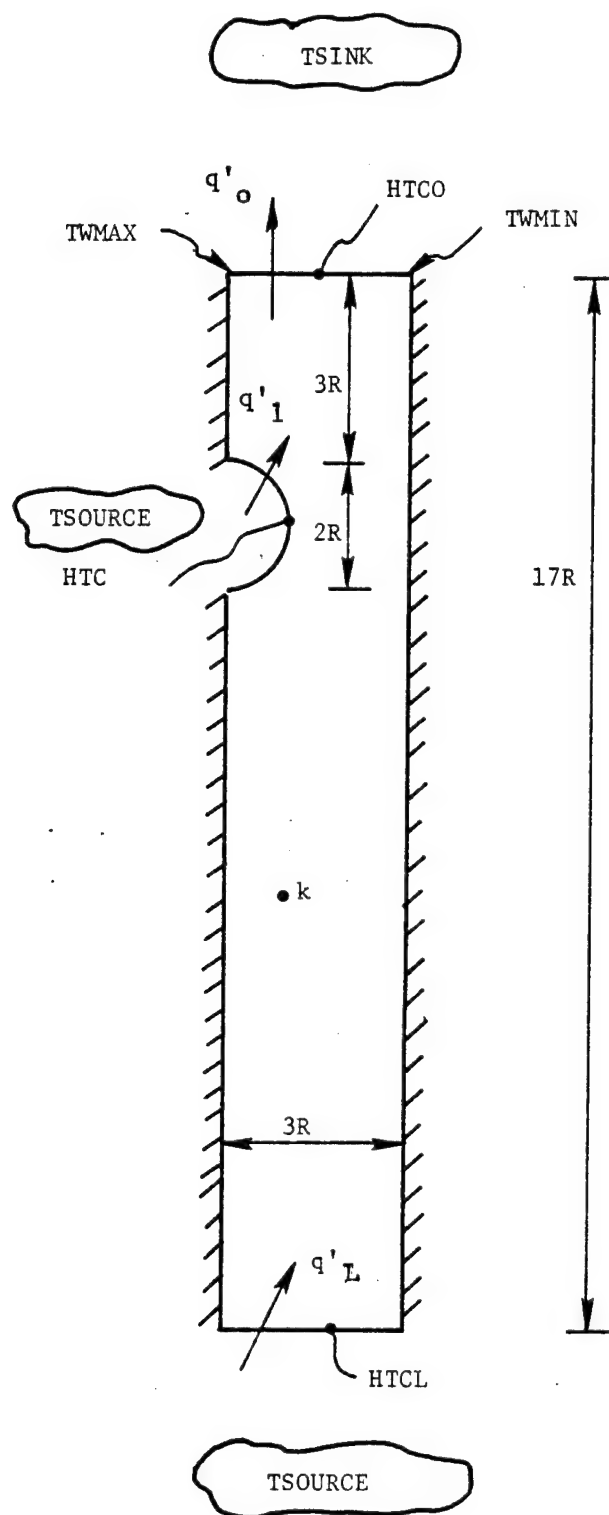


Figure 80 Reference Case: One Layer of Tubes.

The dimensionless cold wall surface temperatures closest to the tube (TWMAX) and farthest from the tube (TWMIN) were also computed as:

$$TWMAX^* = 0.27414 \quad (39)$$

$$TWMIN^* = 0.26795 \quad (40)$$

Note that when $TSINK = 0^{\circ}\text{F}$ and $TSOURCE = 200^{\circ}\text{F}$ then $TWMIN = 53.39^{\circ}\text{F}$, which is well above the freezing point of water. Also, the difference between TWMAX and TWMIN would be only 1.238°F .

7.2.3 Effect of Heat Transfer at the Hot Wall Surface

Equations (36-38) show that 98% of the heat flow through the top surface comes from the tube, and only 2% comes from the bottom surface. A simple but more conservative approach would be to neglect the heat contribution from the bottom surface. Therefore, the reference case was repeated with an adiabatic bottom surface: that is, set $HTCL = BL = 0$.

The BIE4 program computed the following values for dimensionless heat transfer and cold wall surface temperature:

$$(q'/k/T)_0 = 0.48845 \quad (41)$$

$$(q'/k/T)_1 = 0.48845 \quad (42)$$

$$TWMAX^* = 0.27365 \quad (43)$$

$$TWMIN^* = 0.26738 \quad (44)$$

Comparing these results with Equations (36-40) for the reference case, it can be seen that the bottom surface has negligible influence upon the top surface. Therefore, the bottom surface was assumed to be adiabatic in all later calculations.

7.2.4 Effect of a Second Layer of Tubes

The effect of adding a second layer of tubes was considered next. The control area for this case is shown in Figure 81. The second layer of tubes was assumed to be located at a depth $3R$ below the first layer of tubes, and the dimensionless surface heat transfer coefficient for both tubes were the same as the reference case; that is,

$$B2 = B1 = 1.64206 \quad (45)$$

The BIE4 program computed the following values for dimensionless heat transfer and wall surface temperature:

$$(q'/k\Delta T)_0 = 0.49338 \quad (46)$$

$$(q'/k\Delta T)_1 = 0.44331 \quad (47)$$

$$(q'/k\Delta T)_2 = 0.05007 \quad (48)$$

$$TWMAX^* = 0.27620 \quad (49)$$

$$TWMIN^* = 0.27029 \quad (50)$$

Equations (46-50) show that 90% of the heat flow through the top surface comes from the upper tube, and only 10% comes from the lower tube. Also, comparing these results to Equations (41 - 44) for a single layer of tubes shows that adding the second layer of tubes increases the heat transfer and wall surface temperature at the top surface less than 1%. That is, if $TSINK = 0^{\circ}\text{F}$ and $TSOURCE = 200^{\circ}\text{F}$, then adding the second layer of tubes would increase $TWMAX$ by only 0.5°F .

Therefore, adding the second layer of tubes has a negligible effect on the cold wall surface temperature for the specified geometry. This is because the upper layer of tubes "masks the view" of the lower layer of tubes to the top wall surface; that is, the upper tube causes a temperature in the region between the upper and lower tubes that is very nearly equal to the temperature of the lower tube. Thus the lower tube has only a small temperature gradient to cause heat conduction from its surface.

There are, of course, cases where the second layer of tubes would have a more significant influence on the cold wall surface. For example, if the air temperature in first layer of tubes falls well below $TSOURCE$, or if the spacing between the upper tubes is very large, then the second layer of tubes would have a greater influence.

7.2.5 Effect of Tube Spacing on Heat Conduction

Calculations were carried out for the reference case illustrated in Figure 80 with a single layer of tubes and an adiabatic bottom surface. The width of the control area was varied from R to $6R$; that is, the spacing between adjacent tubes was varied from zero to $10R$ (five tube diameters).

The results computed by the BIE4 program are plotted in Figures 82 and 83. Results for dimensionless wall surface temperature are plotted in Figure 82. Note that $TWMAX$ decreases more than $TWMIN$ as SPACE increases; that is, the wall surface temperature not only decreases with spacing, but it also becomes nonuniform.

Results for dimensionless heat transfer from a tube to the upper wall surface are plotted versus tube spacing in Figure 83. Note that heat transfer from a tube increases as spacing increases (tubes are eliminated); however, the heat transfer increase does not compensate for the loss of tubes.

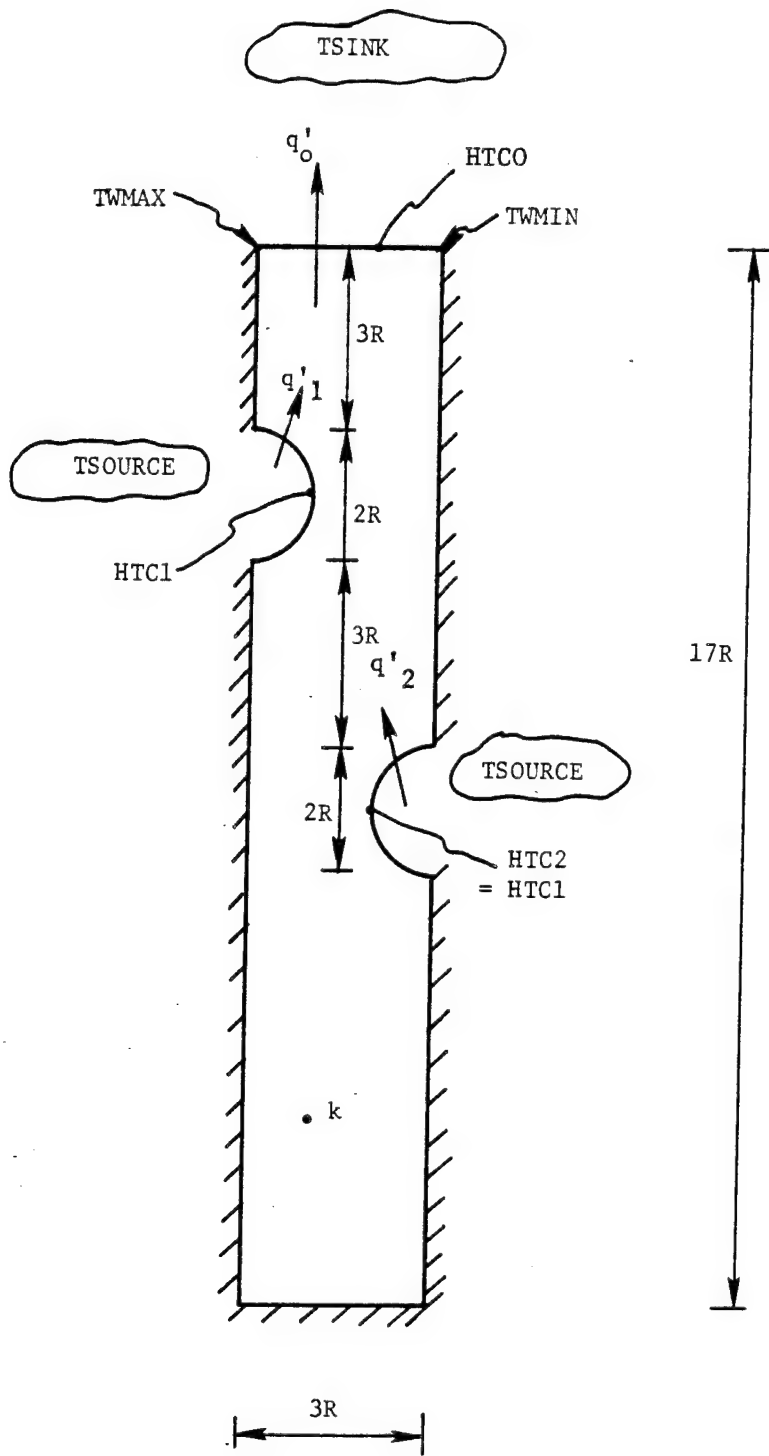


Figure 81 Control Area with Two Layers of Tubes.

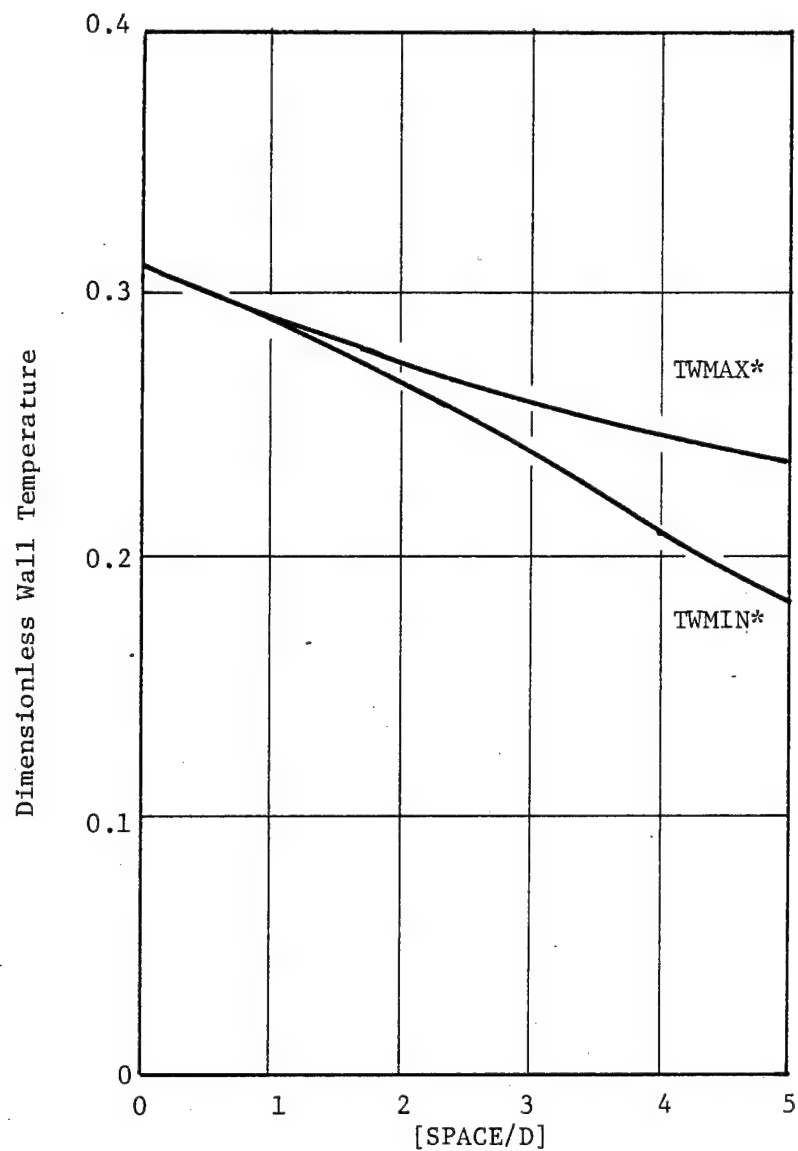


Figure 82 Effect of Tube Spacing on Dimensionless Wall Surface Temperature.

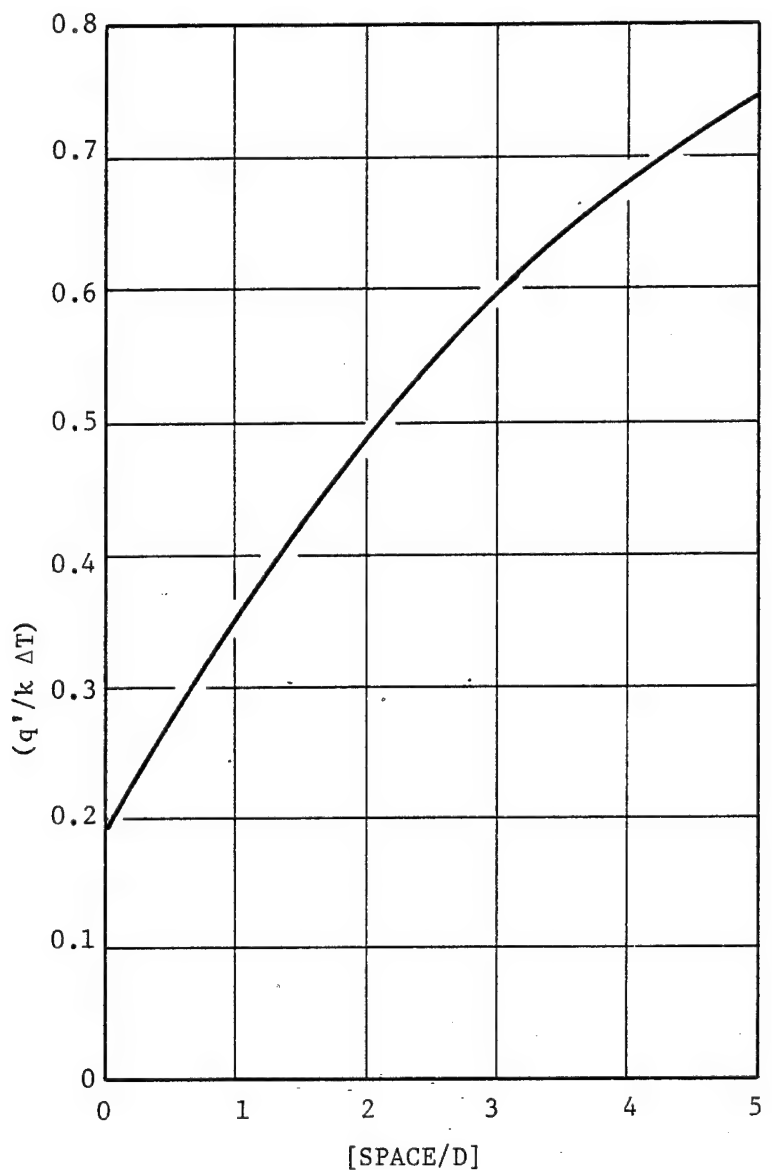


Figure 83 Effect of Tube Spacing on Dimensionless Wall Surface Heat Transfer.

It is of interest to determine a heat conduction shape factor for the control area. An equation for the rate of heat transfer (per unit depth) from a capture to the top wall surface is:

$$q' = \frac{[TSOURCE - TSINK]}{\left[\frac{1}{R(HTC1)} + \frac{1}{Sk} + \frac{1}{(R+SPACE/2)HTCO} \right]} \quad (51)$$

Where the rate of heat conduction is proportional to the shape factor, S. Equation (51) can be rearranged to give the following dimensionless form:

$$(q'/k^T) = \frac{1}{\left[\frac{1}{B1} + \frac{1}{S} + \frac{1}{(1+SPACE/D)BO} \right]} \quad (52)$$

Equation (52) can be solved for conduction shape factor to give:

$$S = \left[\frac{1}{(q'/k^T)} - \frac{1}{B1} - \frac{1}{(1+SPACE/D)BO} \right]^{-1} \quad (53)$$

Shape factor can be determined by substituting values of BO and B1 into Equation (53) along with computed values of (q'/k^T) plotted in Figure 83. The resulting shape factor values are plotted in Figure 84 versus tube spacing.

A least-squares regression fit was made to the curve in Figure 84 to give the following equation for conduction shape factor:

$$S = 0.28985 + 0.28278 * (SPACE/D) - 0.022247 * (SPACE/D)^2 \quad (54)$$

Note that Equation (54) is valid only for a single layer of tubes at a depth of 1.5D from the cold outer wall surface. The rate of heat transfer can then be determined from Equations (52) and (54), and the average wall surface temperature at an axial cross section can be determined from:

$$TWALL* = (q'/k^T) \left[\frac{1}{(1+SPACE/D)BO} \right] \quad (55)$$

7.3 Axial Variation of TWALL

The effect of tube spacing on the surface temperature of a composite wall of arbitrary length can be determined by inserting Equations (52), (54), and (55) into the SIMCAP computer program. This was done and the modified code was named SIMCAP2.

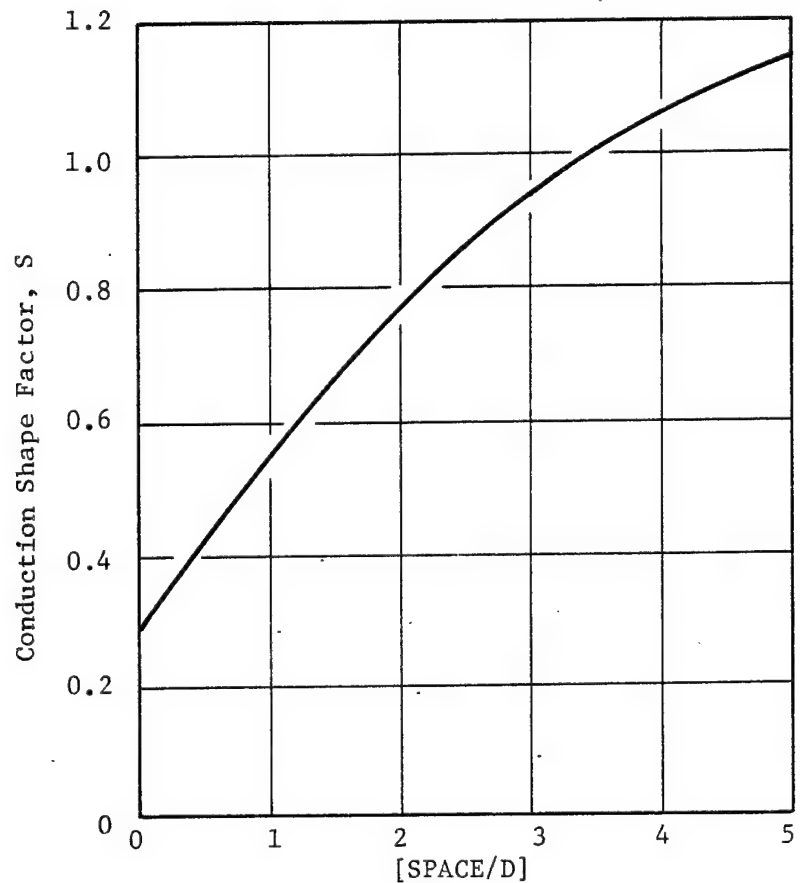


Figure 84 Effect of Tube Spacing on Heat Conduction Shape Factor.

SIMCAP2 predictions showing the effect of tube spacing on a captube having a length of one foot are shown in Figure 85. The axial variations of air temperature in the captube(TCAP) and average cross-sectional wall surface temperature (TWALL) are plotted versus distance from the tube inlet for tube spacing from zero to five tube diameters. Note that a tube spacing of only one diameter will significantly reduce TWALL.

7.4 Comparison of Test Results with Computer Code

Analysis of test data was conducted with emphasis on the sensitivity of difference between predicted assumptions and actual test hardware with related test results. For example, a difference of only a few thousandths of an inch between the assumed depth of a capillary tube below the air flow surface versus its actual measured depth could display a significant difference between predicted and measured test results. Test data was carefully reviewed with this sensitivity in mind.

The following Figures 86 thru 92 illustrate how closely actual test results compare with the computer SIMCAP predictions.

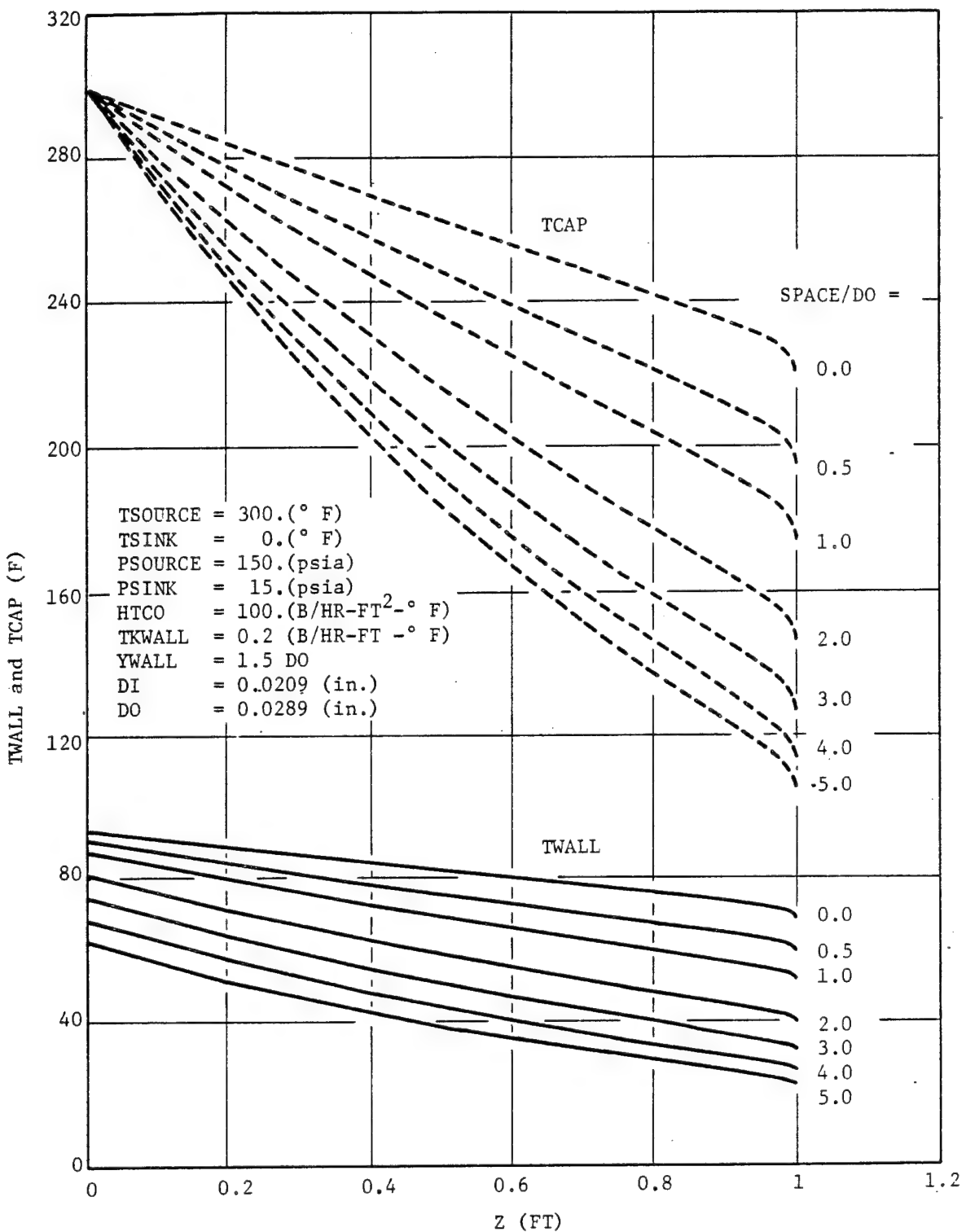
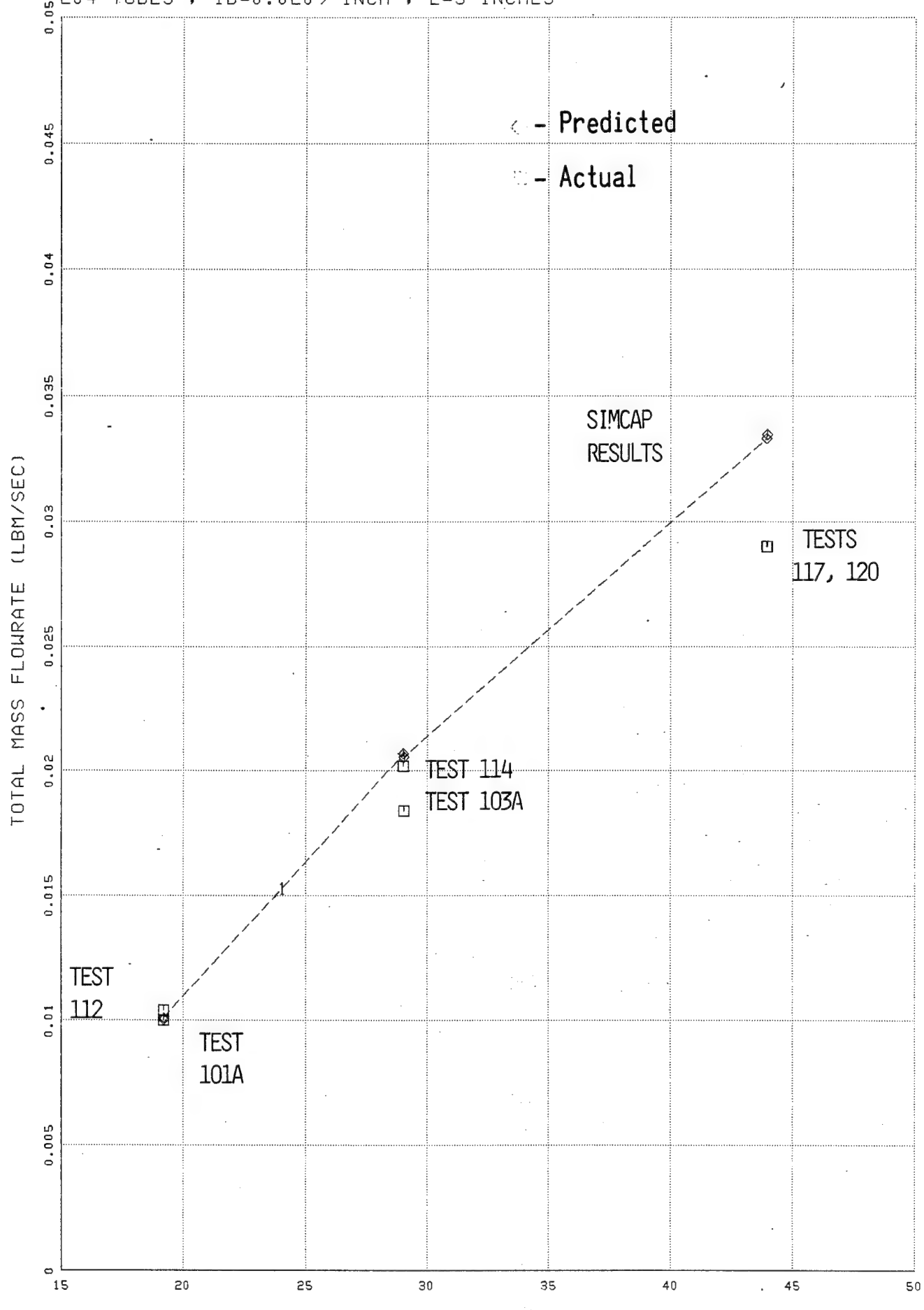


Figure 85 SS2D Captube Heat Transfer Model Effect of Captube Spacing on T_{WALL} and T_{CAP} Distributions.

HEAT TRANSFER TESTS 101A, 103A, 112, 114, 117, 120
204 TUBES ; ID=0.0209 INCH ; L=3 INCHES



SOURCE PRESSURE (PSIA)

Figure 86

SIMCAP RESULTS FOR 6-IN. WIDE CAPTUBE HEAT TRANSFER TESTS
TEST 101A : EFFECT OF YWALL

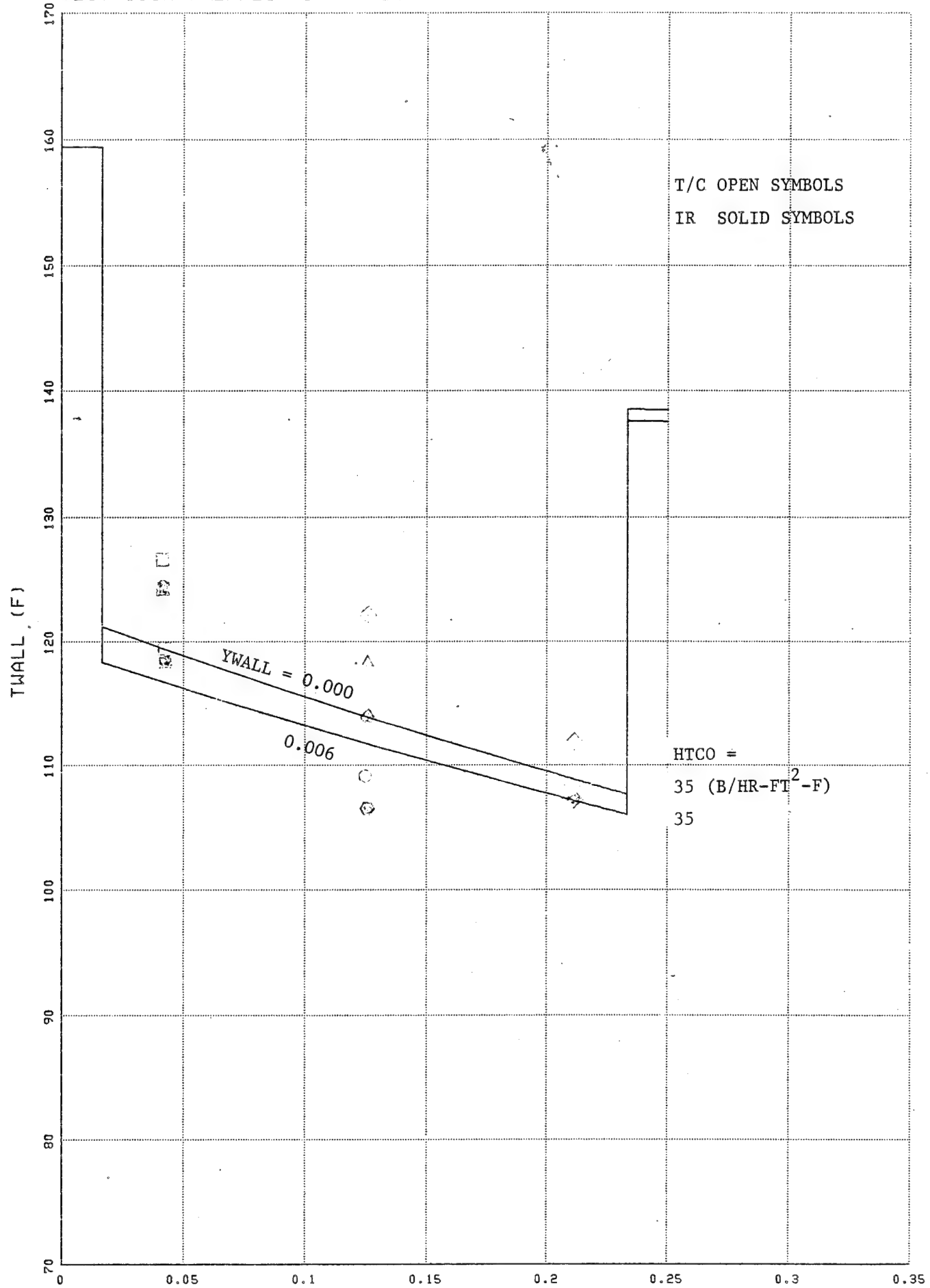


Figure 87

Z (FT)

120

SIMCAP RESULTS FOR 6-IN. WIDE CAPTUBE HEAT TRANSFER TESTS
TEST 103A ; EFFECT OF YWALL

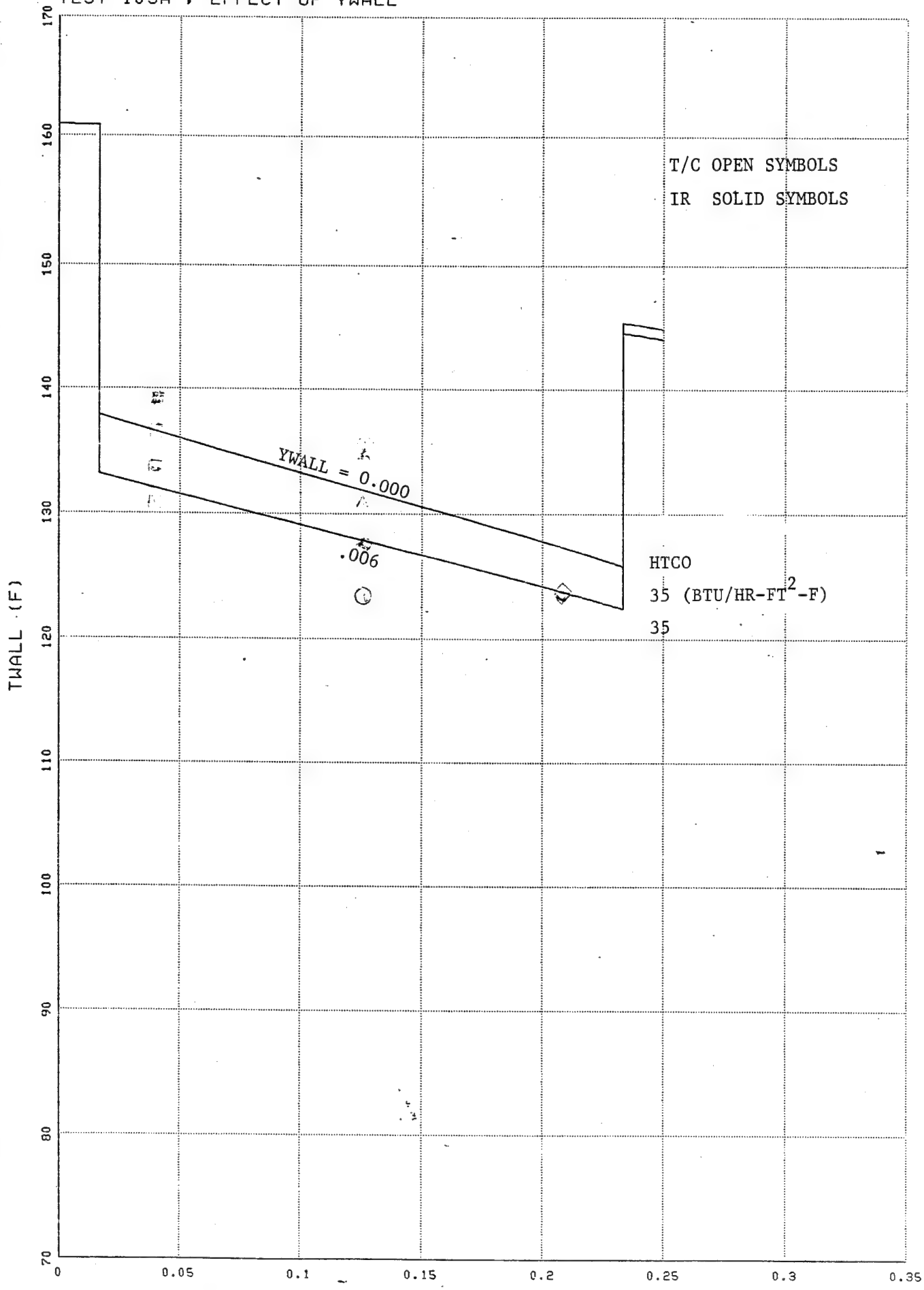


Figure 88

C 5 6

SIMCAP RESULTS FOR 6-IN. WIDE CAPTUBE HEAT TRANSFER TESTS
TEST 112 : EFFECT OF YWALL

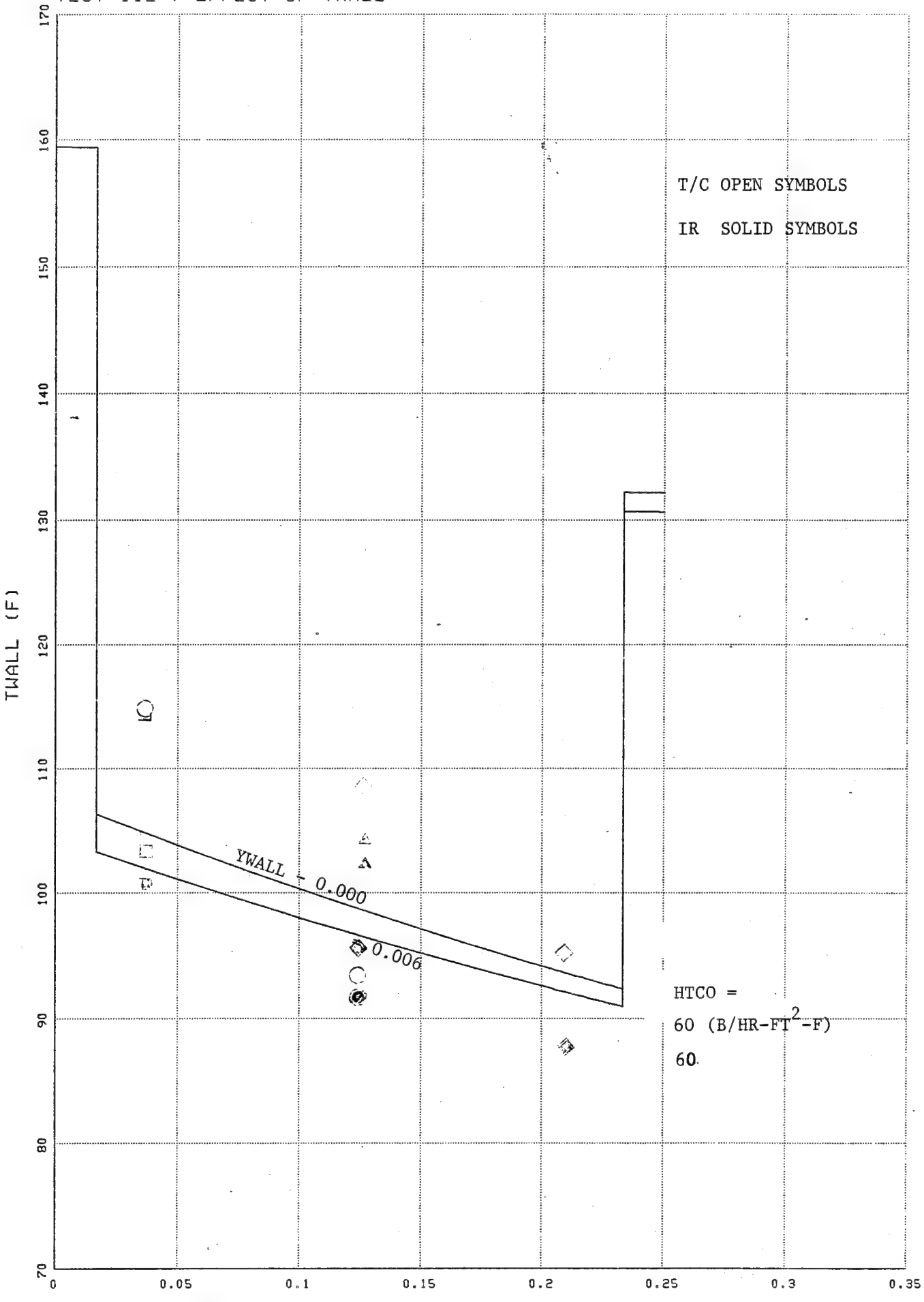


Figure 89

Z (FT)

122

SIMCAP RESULTS FOR 6-IN. WIDE CAPTUBE HEAT TRANSFER TESTS
TEST 114 ; EFFECT OF YWALL

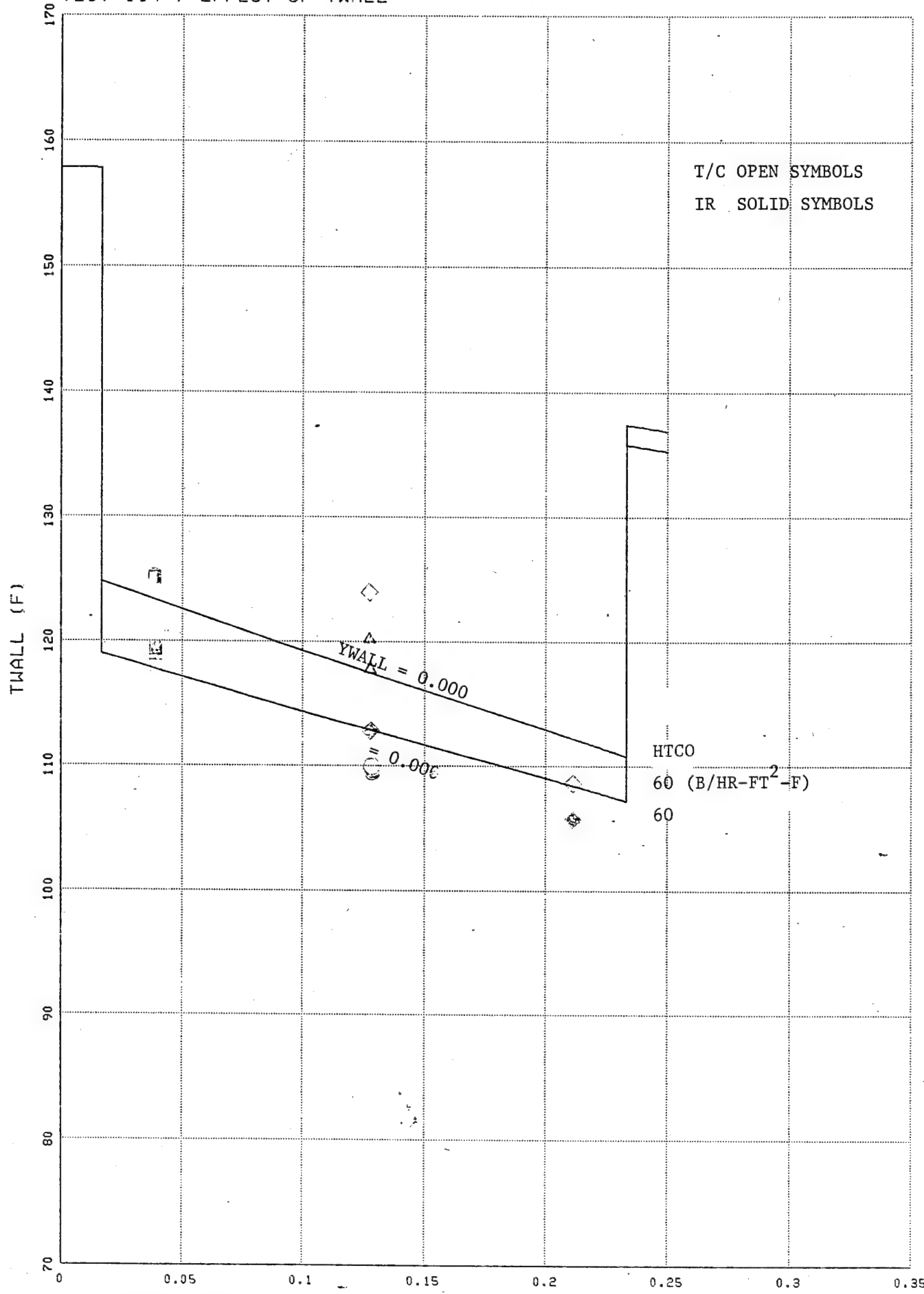


Figure 90

SIMCAP RESULTS FOR 6-IN. WIDE CAPTUBE HEAT TRANSFER TESTS
TEST 117 ; EFFECT OF YWALL

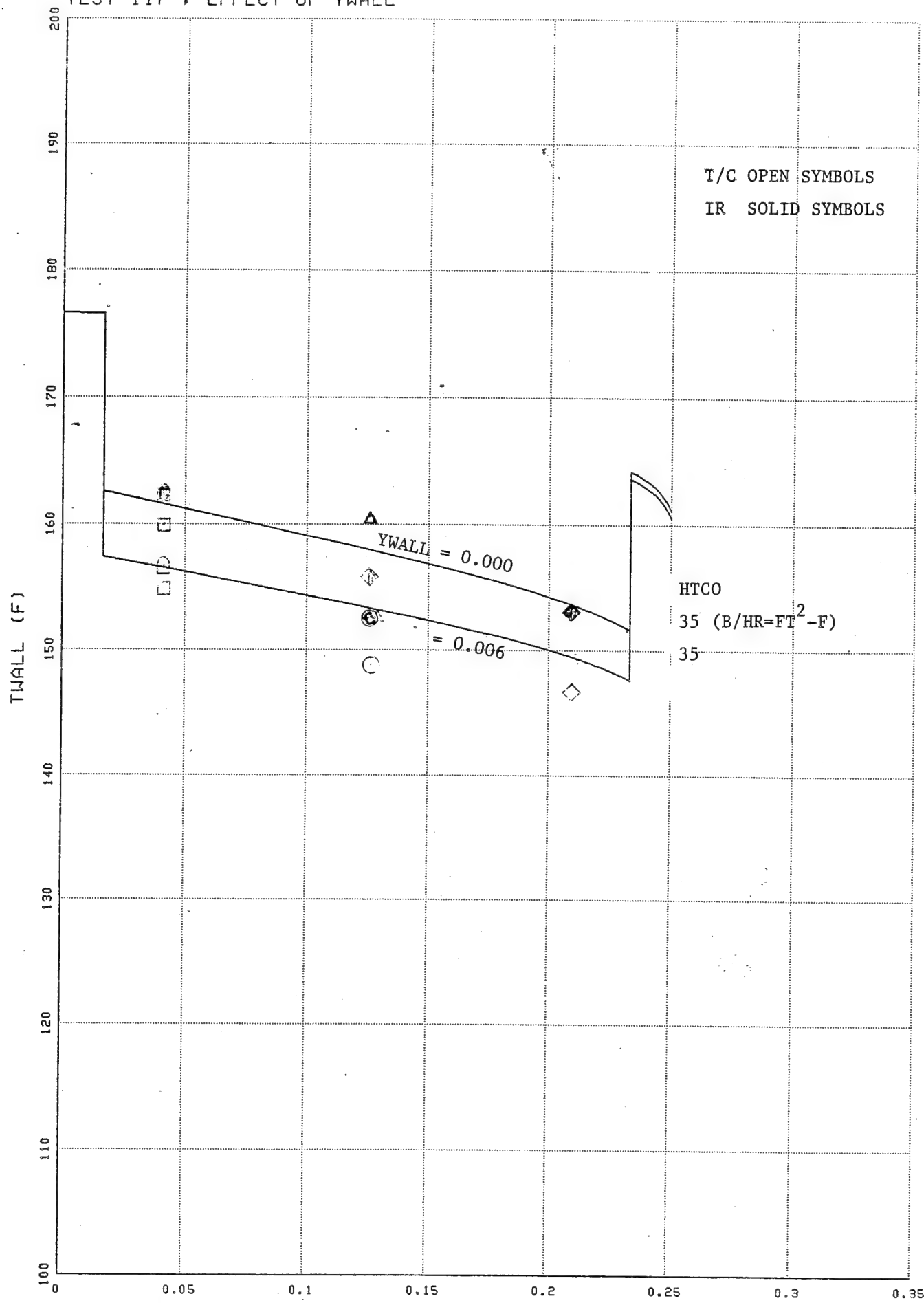


Figure 91

SIMCAP RESULTS FOR 6-IN. WIDE CAPTUBE HEAT TRANSFER TESTS
TEST 120 : EFFECT OF YWALL

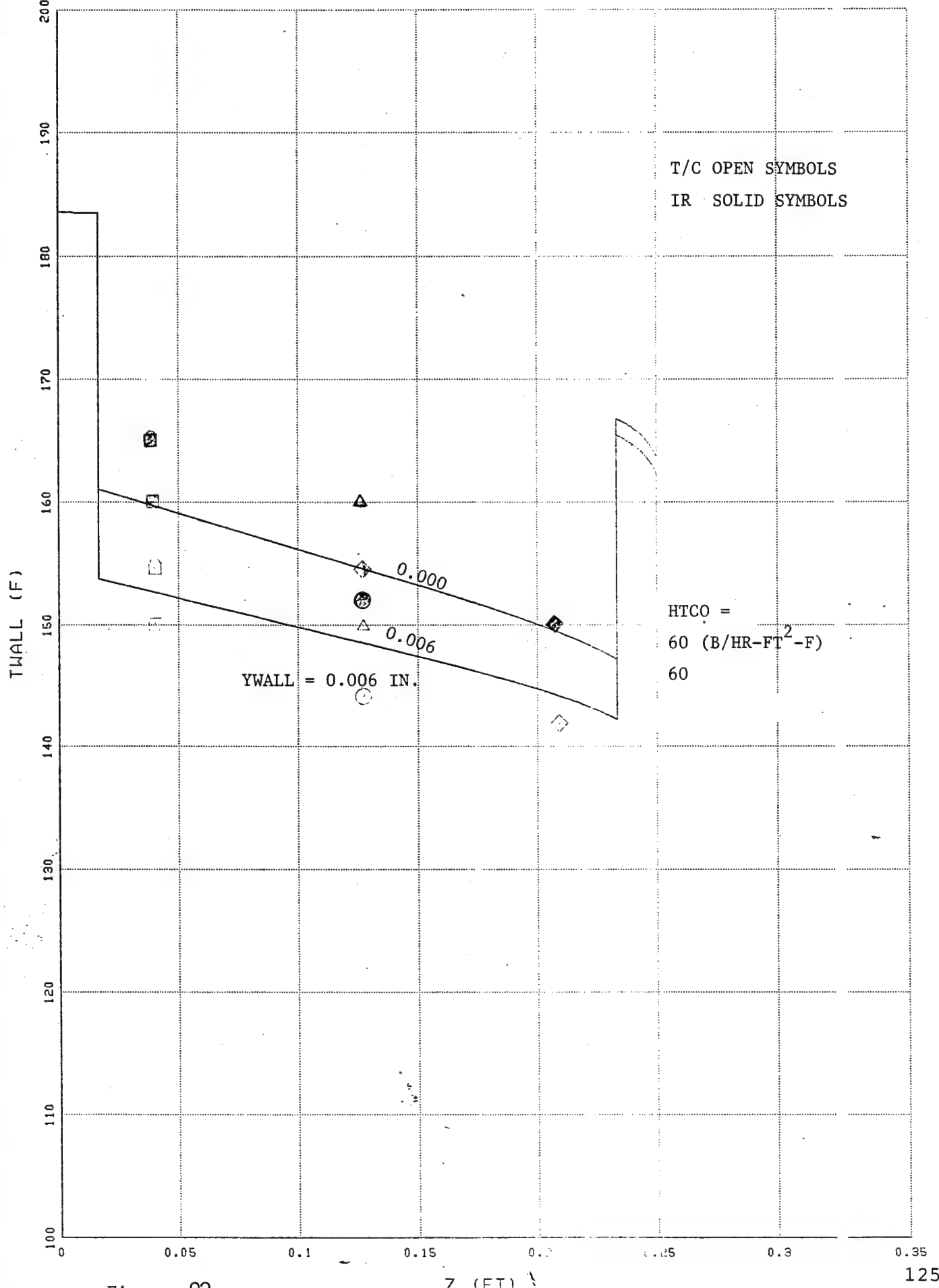


Figure 92

8.0 SUMMARY AND CONCLUSIONS

A heat transfer analysis was made to determine the thermal performance of capillary tubes embedded within a composite wall. The primary objectives were to determine the effects of spacing between adjacent tubes, and of multiple layers of tubes within the wall.

A two-dimensional heat conduction analysis using the BIE4 computer program was made at a typical axial cross section of the wall. Results show that a second layer of tubes had a small effect on heat transfer and temperature at the cold outer surface of the composite wall for the assumed geometry. Also, the cold wall temperature decreased significantly as spacing increased between adjacent tubes.

A correlation for two-dimensional heat conduction shape factor for a single layer of tubes was also derived, and inserted into a modified version of the SIMCAP capture simulation code. Computed results show that a tube spacing of only one diameter can significantly reduce wall surface temperature.

The BIE4 2D heat conduction program could be combined or coupled with the SIMCAP simulation code to obtain a versatile tool for analyzing complete tube/wall assemblies. However, such an effort is beyond the work scope of this investigation.

The correlation between infra-red monitoring, thermocouple recording and calculated analysis was exceptionally close for the entire scope of this program.

9.0 PROJECTIONS FOR FUTURE CAPTUBE EFFORT

The prospective need for larger diameter capillary tubes for anti-icing during lower engine performance conditions such as at loiter, descent or taxiing when compressor bleed air-pressure and temperature is relatively low, is being reviewed. No fixed assessment has yet been made, however, as all engines are different in this regard. Several tube vendors have been approached with request for tube availability up to .050" I.D./.070" O.D. During the course of discussing tube features with several vendors, it became apparent that tube stress corrosion and contamination corrosion are factors that must be addressed. Several glass tube suppliers cautioned that structural stress could induce stress corrosion cracks in their capillary tubes in a relatively short time. The suppliers advised that their tubes should be composited as straight and unstressed as possible. They also advised that contamination such as acid rain would accelerate failure of a stressed tube. However, even if tubes should crack, if they are composited sufficiently deep enough into the surface, they could still function as an anti-icing duct of hot air without catastrophic failure. Perhaps such tubes can be coated internally with a barrier coating sufficient to inhibit corrosive attack. The Hewlett-Packard Company that supplied the tubes used in this contract had the tubes jacketed externally with a very thin coat of polyimide as a means of inhibiting external scratching and corrosive attack. It is obvious that larger diameter tubing should be easier to coat internally, but evaluation of this prospective solution was beyond the scope of this contract.

Several conceptual studies were made to project future utilization of capillary tubes in anti-icing structures. Figures 93 and 94 show two versions of front frames for jet engines where hot air can be ducted through surface capillary tubes clustered in tangent assembly around radial struts. Figure 95 shows how one vulnerable area on a metal or composite inlet flap might be anti-iced with capillary tubes bonded in one particular area.

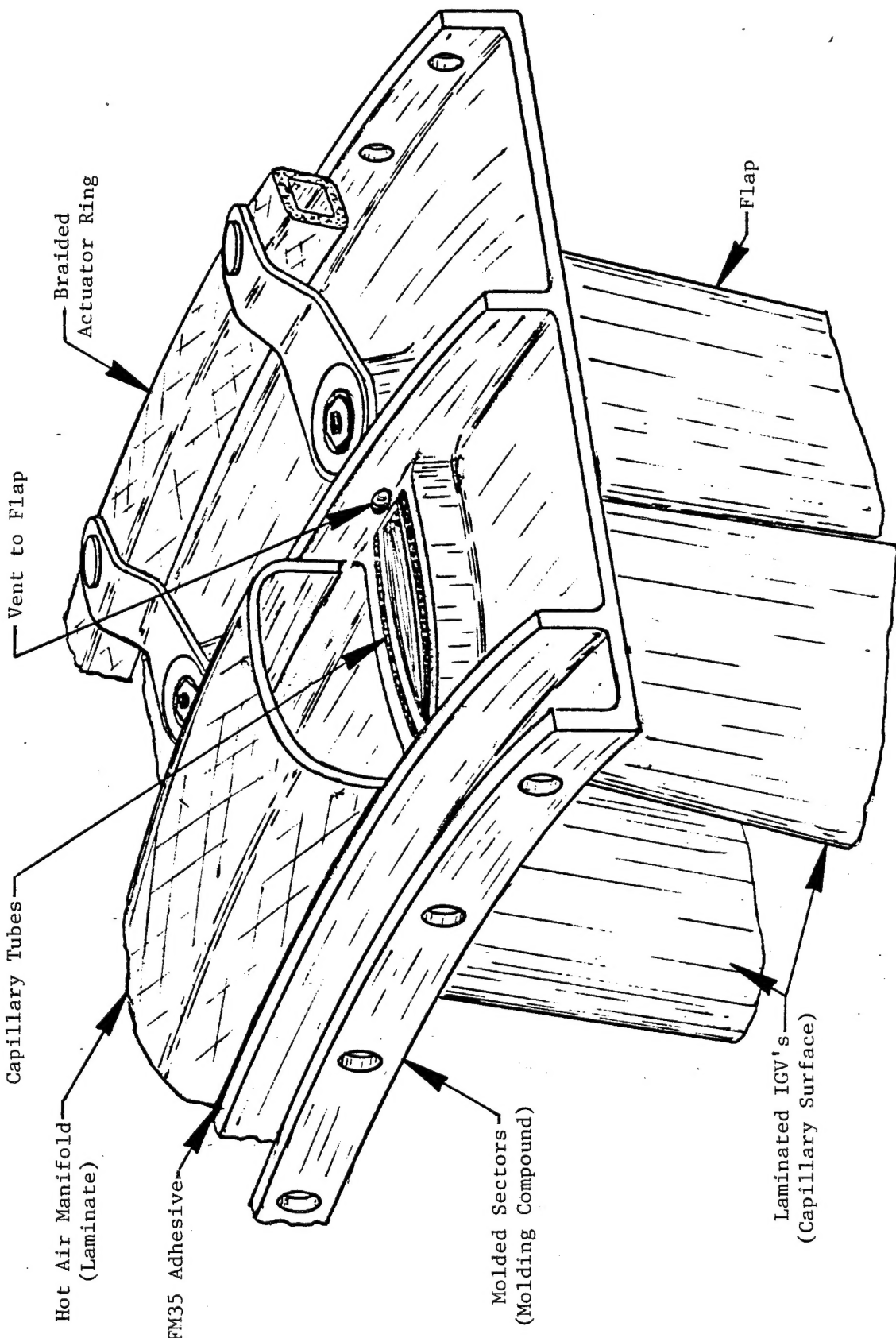


Figure 93 Graphite/PMR15 Composite Anti-Iced IGV Assembly.

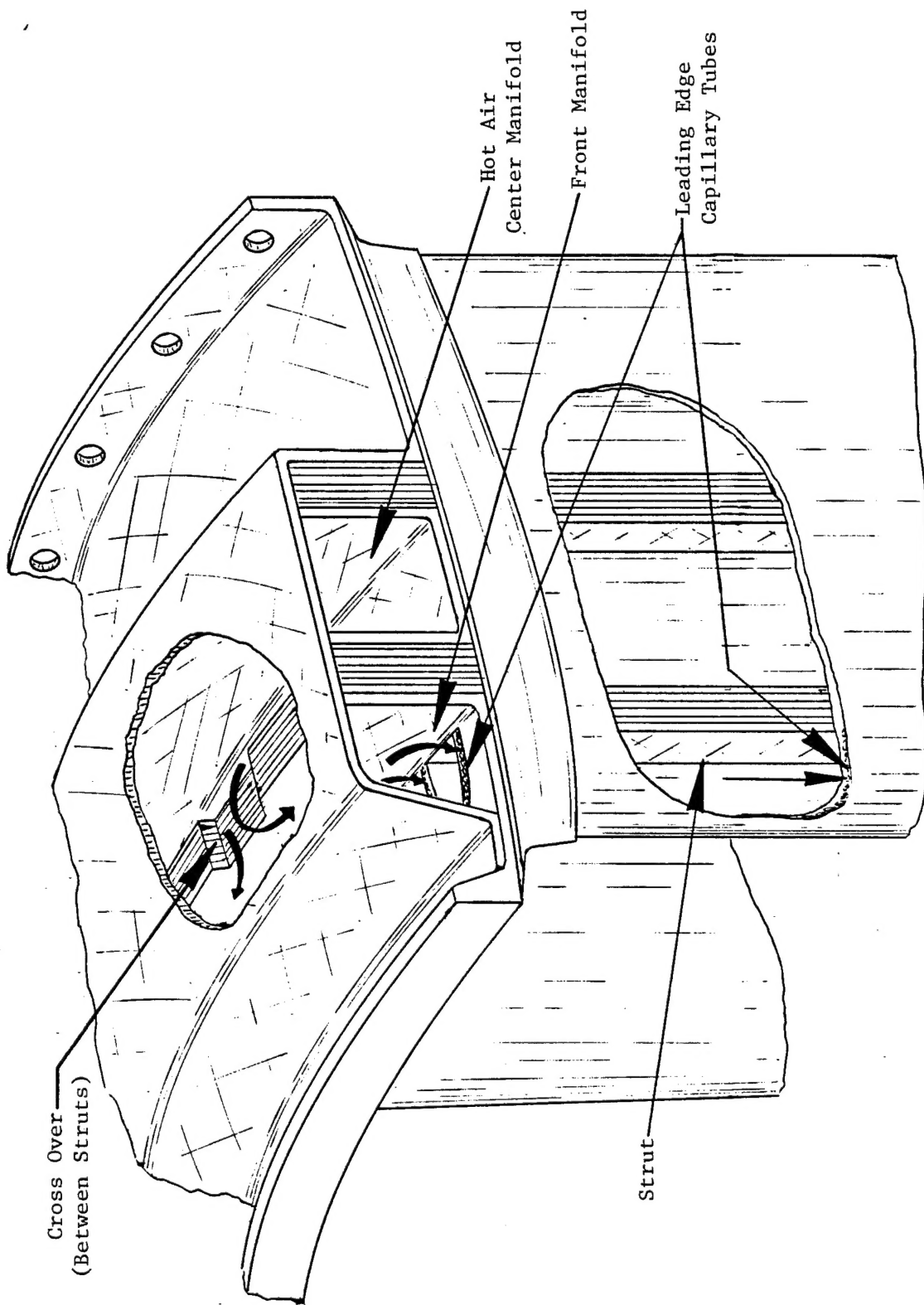


Figure 94 Graphite/PMR15 Composite, Anti-Iced Front Frame Assembly.

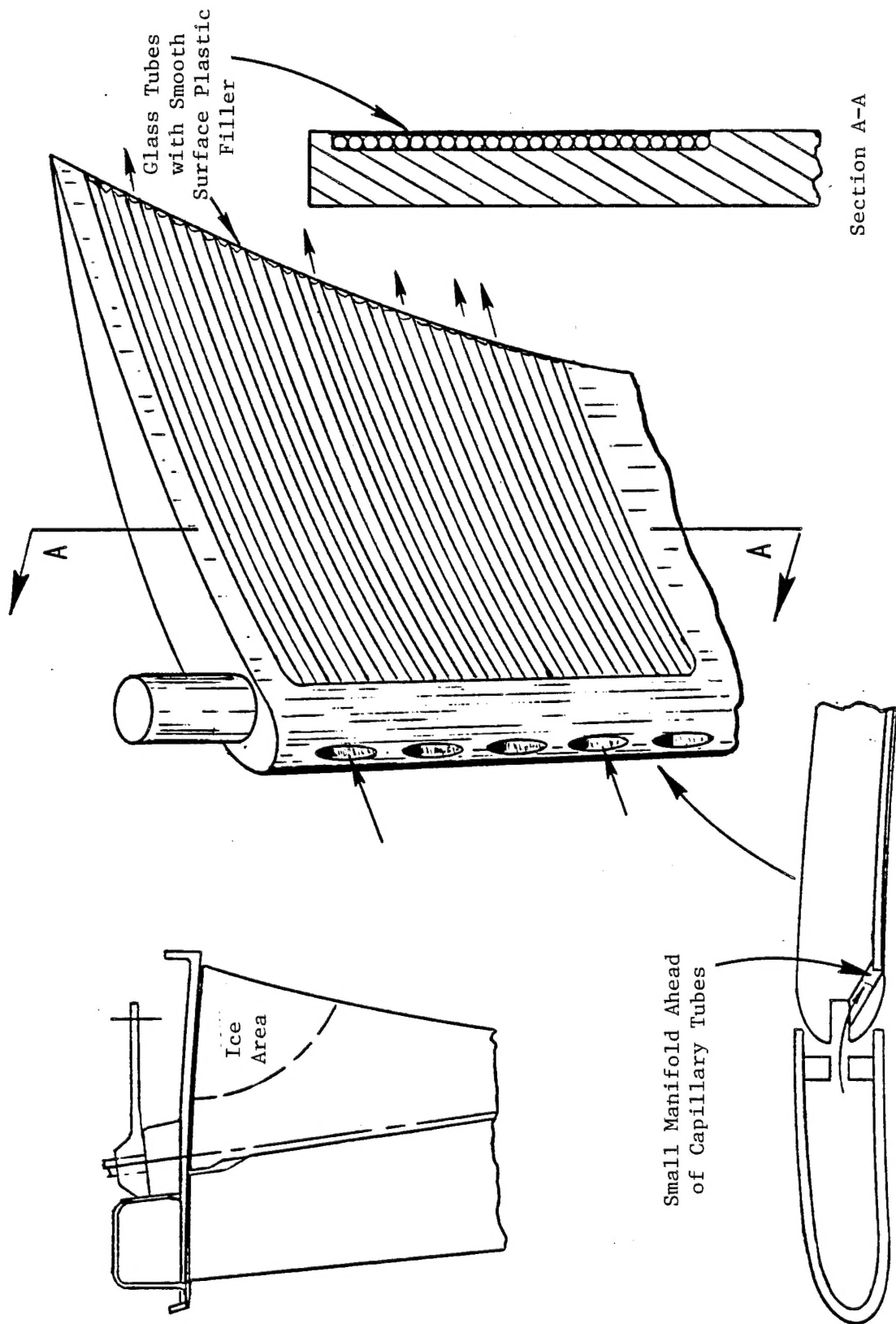


Figure 95 Concept for Anti-Icing IGV Flap.

10.0 PROPOSED FOLLOW-ON EFFORT

1. A detailed design of a captube anti-iced jet engine front frame should be made. Detailed design will require input from performance, systems, heat transfer and mechanical design engineers.
2. An evaluation should be made on impact damage of captube structures and possible methods of repair.
3. A proof-of-concept test of an anti-iced captube frame should be a culminating effort for a future program.